

## **Table of Contents**

1. **Introduction to Synthetic Analog Computation in Living Cells**
2. **Detailed Biochemical Models for Synthetic Analog Genetic Circuits**
  - 2.1. Overview
  - 2.2. Modeling the Binding of Inducers to Transcription Factors
  - 2.3. Modeling  $P_{lux}$  and  $P_{BAD}$  Promoter Activity
  - 2.4. Modeling of Degradation Rates in the Presence of Binding Sites
  - 2.5. Modeling Transcription Factor Expression in the Presence of Binding Sites
  - 2.6. Positive Feedback Model
  - 2.7. Positive Feedback and Shunt Model (PF-Shunt)
  - 2.8. Modeling the  $P_{lacO}$  Promoter
  - 2.9. Modeling the Wide-Dynamic-Range (WDR) Negative-Logarithm Circuit
  - 2.10. Modeling the Power Law Circuit
3. **Supplementary Experiments**
  - 3.1. LuxR-Based Open Loop Circuits
  - 3.2. AraC-Based Open Loop Circuits
  - 3.3. Dummy Shunt Circuit

Supplementary Table 1. List of abbreviations used in this study  
 Supplementary Table 2. Parameter values for biochemical circuit models
4. **Simple Mathematical Models Models for Synthetic Analog Genetic Circuits**
  - 4.1. Simple Mathematical Model for the WDR Positive-Logarithm Circuit
  - 4.2. Simple Mathematical Model for the WDR Negative-Logarithm Circuit
  - 4.3. Simple Mathematical Model for the Adder Circuit
  - 4.4. Simple Mathematical Model for the Ratiometer Circuit
  - 4.5. Simple Mathematical Model for the Power Law Circuit
5. **Mixed Analog-Digital Circuits**
6. **A Double-Promoter PF-Shunt Circuit**
7. **Dynamic Measurements Of Analog Genetic Circuits**
8. **Sensitivity Analysis**
9. **Minimal Model**
10. **Composition of Analog Functions**
11. **Potential Applications of Synthetic Analog Circuits**
12. **FACS Data**
13. **Plasmid Construction**

Supplementary Table 3. List of strains used in this study  
 Supplementary Table 4. List of biological parts used in this study

## 14. Plasmid Maps

## 15. Supplementary References

# 1 Introduction to Synthetic Analog Computation in Living Cells

We present two strategies for designing synthetic gene circuits which implement analog computation in living cells. The first approach involves detailed biochemical models which capture the effects of positive feedback, shunt plasmids, protein degradation, and transcription-factor diffusion. These detailed biochemical models enable us to accurately capture the behavior of the various analog circuit topologies by solely changing the parameters that are expected to vary between experiments (e.g., plasmid copy number). The derivation of the biochemical models used in this paper is described in Supplementary Section 2.

The second approach uses simple mathematical functions, such as logarithms, to capture the behavior of our analog circuit motifs with a handful of parameters. These empirical mathematical functions enable the composition of analog circuit modules together with predictable behavior. Thus, they are useful in the synthetic circuit design process because they are easily interpretable by human designers and remain accurate in circuits of higher complexity. The derivation of these simple mathematical representations of synthetic analog circuits is described in Supplementary Section 4.

## 2 Detailed Biochemical Models for Synthetic Analog Genetic Circuits

### 2.1 Overview

Here, we present our detailed biochemical models for synthetic analog genetic circuits. Our models incorporate the effects of biochemical interactions such as the binding of inducers to transcription factors, the binding of transcription factors to promoters, the degradation of free and bound transcription factors to DNA, the effective variation of transcription-factor diffusion-limited binding rates inside the cell with variation in plasmid copy number, and the integration of all these effects in our frequently used positive-feedback-and-shunt (PF-shunt) topology. To clarify the various interactions within our biochemical reaction models, we also show analog circuit schematics<sup>1</sup> that represent steady-state mass-action kinetics.

Our models yield insight into and predict network behavior. Our models assume that the concentration of chemical species is uniformly distributed and the behavior of our genetic circuits can be analyzed in the steady state. For each experiment, we only adjusted model parameter values that varied in that experiment (e.g., the copy number of plasmids used). All other parameter values were used consistently throughout all of our models.

Here, we use the following terminology to describe interactions between inducers, transcription factors, and DNA. Transcription factors are called “free” if they are not interacting with inducers or DNA. When inducers complex with transcription factors, we call the resulting product the inducer-transcription-factor “complex”. When free transcription factors bind to DNA, we call them “bound” transcription factors. When inducer-transcription factor complexes bind to DNA, we call them “bound complex transcription factors”. (For all the abbreviations, refer to Supplementary Table 1). Model files can be found at

<http://www.rle.mit.edu/acbs/research/supplementary>

and also at

<http://www.rle.mit.edu/sbg/supp.shtml>

## 2.2 Modeling the Binding of Inducers to Transcription Factors

The set of ordinary differential equations which model the process of free inducer ( $I_n$ ) binding to free transcription factor ( $T$ ) ( $I_n + T \leftrightarrow T_C$ ) can be described by:

$$\begin{aligned} \frac{dT_C}{dt} &= k_1 \cdot I_n \cdot T - k_{-1} \cdot T_C \\ \frac{dT}{dt} &= -\frac{dT_C}{dt} \\ \frac{dI_n}{dt} &= -\frac{dT_C}{dt} \end{aligned} \quad (1)$$

Where  $T_C$  is the concentration of transcription factor bound to the inducer,  $k_1$  is the rate of the forward reaction and  $k_{-1}$  is the rate of the reverse reaction. At equilibrium, the bound transcription factor is equal to:

$$T_C = \frac{I_n \cdot T}{K_m} \quad (2.1)$$

$$T_C + I_n = I_{nT} \quad (2.2)$$

$$T_C + T = T_T \quad (2.3)$$

$$\Rightarrow T_C = \frac{(I_{nT} + T_T + K_m) - \sqrt{(I_{nT} + T_T + K_m)^2 - 4T_T \cdot I_{nT}}}{2} \quad (2.4)$$

Where  $I_{nT}$  is the concentration of total inducer,  $T_T$  is the concentration of total transcription factor and  $K_m = k_{-1}/k_1$  is the dissociation constant. In the case that  $\frac{T_T}{K_m} < 1 + \frac{I_{nT}}{K_m}$ , we can approximate Eq. 2.4 as:

$$T_C = T_T \cdot \frac{\frac{I_n T}{K_m}}{1 + \frac{I_n T}{K_m} + \frac{T_T}{K_m}} \quad (3)$$

Note that the Michaelis-Menten approximation is a special case of Eq. 3 (where  $T_T \ll I_n T$ ). Eq. 3 shows that the amount of bound transcription factor ( $T_C$ ) will saturate at high values of total transcription factor ( $T_T$ ) because it is limited by the inducer concentration ( $I_n T$ ); in contrast, in the Michaelis-Menten model, bound transcription factor increases linearly with increasing total transcription factor, without being limited by inducer saturation.

Many binding reactions include cooperativity between inducers and transcription factors. We will study two specific cases of cooperativity ( $h = 2$  and  $3$ , where  $h$  is the Hill Coefficient):

i. In the case of  $h = 2$  (Hill Coefficient = 2):



The set of the ordinary differential equations which describes the set of biochemical reactions in Eq. 4 includes:

$$\frac{dT_{C1}}{dt} = k_1 \cdot I_n \cdot T - k_{-1} \cdot T_{C1} - k_2 \cdot I_n \cdot T_{C1} + k_{-2} \cdot T_C$$

$$\frac{dT_C}{dt} = k_2 \cdot I_n \cdot T_{C1} - k_{-2} \cdot T_C$$

$$\frac{dT}{dt} = -\frac{dT_{C1}}{dt} - \frac{dT_C}{dt} \quad (5)$$

$$\frac{dI_n}{dt} = -\frac{dT_{C1}}{dt} - \frac{dT_C}{dt}$$

At equilibrium:

$$T_{C1} = \frac{I_n \cdot T}{K_{m1}} \quad (6.1)$$

$$T_C = \frac{I_n \cdot T_{C1}}{K_{m2}} \quad (6.2)$$

$$T + T_{C1} + T_C = T_T \quad (6.3)$$

$$I_n + T_{C1} + T_C = I_n T \quad (6.4)$$

Where  $K_{m1} = k_{-1}/k_1$ , and  $K_{m2} = k_{-2}/k_2$ . Substituting Eq. 6.1, 6.3 and 6.4 into Eq. 6.2, we get:

$$T_C = \frac{(I_n T - T_{C1} - T_C)^2 \cdot (T_T - T_{C1} - T_C)}{K_{m1} \cdot K_{m2}} \quad (7)$$

We will assume that the concentration of the product of the final reaction is larger than the concentration of the product of the intermediate reactions ( $K_{m2} \ll K_{m1}$ ); in this case, Eq. 7 can be approximated by:

$$T_C = \frac{(I_{nT} - T_C)^2 \cdot (T_T - T_C)}{K_{m1} \cdot K_{m2}}$$

$$T_C^3 - T_C^2 \cdot (2I_{nT} + T_T) + T_C \cdot (2I_{nT} \cdot T_T + I_{nT}^2 + K_m^2) = T_T \cdot I_{nT}^2 \quad (8)$$

Where  $K_m^2 = K_{m1} \cdot K_{m2}$ . In the case that  $\frac{T_T}{K_m} < 1 + \frac{I_{nT}}{K_m}$ , we can approximate Eq. 8 as

$$T_C = T_T \cdot \frac{\left(\frac{I_{nT}}{K_m}\right)^2}{1 + \left(\frac{I_{nT}}{K_m}\right)^2 + \left(\frac{I_{nT}}{K_m}\right) \cdot \frac{T_T}{0.5K_m}} \quad (9)$$

ii. In the case of  $h = 3$  (Hill Coefficient = 3):



The set of the ordinary differential equations which describes the set of biochemical reactions in Eq. 10 includes:

$$\frac{dT_{c1}}{dt} = k_1 I_n \cdot T - k_{-1} \cdot T_{c1} - k_2 I_n \cdot T_{c1} + k_{-2} \cdot T_{c2}$$

$$\frac{dT_{c2}}{dt} = k_2 \cdot I_n \cdot T_{c1} - k_{-2} \cdot T_{c2} - k_3 \cdot I_n \cdot T_{c2} + k_{-3} \cdot T_C$$

$$\frac{dT_C}{dt} = k_3 \cdot I_n \cdot T_{c2} - k_{-3} \cdot T_C \quad (11)$$

$$\frac{dT}{dt} = -\frac{dT_{c2}}{dt} - \frac{dT_{c1}}{dt} - \frac{dT_C}{dt}$$

$$\frac{dI_n}{dt} = -\frac{dT_{c2}}{dt} - \frac{dT_{c1}}{dt} - \frac{dT_C}{dt}$$

At equilibrium:

$$T_{c1} = \frac{I_n \cdot T}{K_{m1}} \quad (12.1)$$

$$T_{c2} = \frac{I_n \cdot T_{c1}}{K_{m2}} \quad (12.2)$$

$$T_C = \frac{I_n \cdot T_{c2}}{K_{m3}} \quad (12.3)$$

$$T + T_{C2} + T_{C1} + T_C = T_T \quad (12.4)$$

$$I_n + T_{C2} + T_{C1} + T_C = I_{nT} \quad (12.5)$$

Where  $K_{m1} = k_{-1}/k_1$ ,  $K_{m2} = k_{-2}/k_2$  and  $K_{m3} = k_{-3}/k_3$ . Substituting Eq. 12.1, 12.2, 12.4 and 12.5 into Eq. 12.3 we get:

$$T_C = \frac{(I_{nT} - T_{C2} - T_{C1} - T_C)^3 \cdot (T_T - T_{C2} - T_{C1} - T_C)}{K_{m1} \cdot K_{m2} \cdot K_{m3}} \quad (13)$$

We will assume that the concentration of the product of the final reaction is larger than the concentration of the products of the intermediate reactions ( $K_{m3} \ll K_{m2}, K_{m1}$ ); in this case Eq. 13 can be approximated by:

$$T_C = \frac{(I_{nT} - T_C)^3 \cdot (T_T - T_C)}{K_{m1} \cdot K_{m2} \cdot K_{m3}} \quad (14)$$

Where  $K_m^3 = K_{m1} \cdot K_{m2} \cdot K_{m3}$ . In the case that  $\frac{T_T}{K_m} < 1 + \frac{I_{nT}}{K_m}$ , we can approximate Eq. 14 as

$$T_C = T_T \cdot \frac{\left(\frac{I_{nT}}{K_m}\right)^3}{1 + \left(\frac{I_{nT}}{K_m}\right)^3 + \left(\frac{I_{nT}}{K_m}\right)^2 \cdot \frac{T_T}{0.3K_m}} \quad (15)$$

Based on these specific cases, we can generalize Eq. 3, 9 and 15 by using the Hill function<sup>2</sup>:

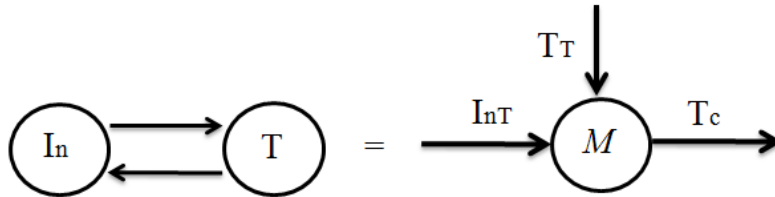
$$T_C = T_T \cdot \frac{\left(\frac{I_{nT}}{K_m}\right)^{h_1}}{1 + \left(\frac{I_{nT}}{K_m}\right)^{h_1} + \left(\frac{I_{nT}}{K_m}\right)^{h_2} \cdot \frac{T_T}{K_n}} \quad (16)$$

where  $h_1$  is the Hill coefficient,  $h_2$  and  $K_n$  are fitting parameters with  $h_2 < h_1$  and  $K_n < K_m$ . We study the condition  $\frac{T_T}{K_m} < 1 + \frac{I_{nT}}{K_m}$  in two different cases:

- I. Open-loop case: if  $I_{nT} \ll K_m$ , then we must design the circuit such that  $T_T/K_m < 1$  to satisfy the above condition; when  $I_{nT} \gg K_m$ , the condition is automatically satisfied for practical ranges of  $T_T$  in cells.
- II. Closed-loop (feedback) case: in the positive-feedback-and-shunt topology,  $T_T$  increases as  $I_{nT}$  increases from transcriptional positive feedback. Thus,  $I_{nT}$  and  $T_T$  track each other. Hence, if  $I_{nT} \ll K_m$ ,  $T_T$  is small such that we also have  $T_T/K_m < 1$  and the condition is automatically satisfied; when  $I_{nT} \gg K_m$ , the condition continues to be satisfied for practical ranges of  $T_T$  in cells as long as the creation of  $T_T$  via feedback is not excessively strong, a feature enabled by our shunting mechanism.

We use Eq. 16 to describe inducer-transcription factor binding reactions in combination with literature-based values for the Hill coefficient  $h_1$  and dissociation constant  $K_m$  (Supplementary

Table 2). Supplementary Figure 1 shows a schematic that represents our model of the binding reaction for an inducer and transcription factor.



**Supplementary Figure 1.** Schematic diagram of the binding reaction for an inducer and transcription factor.

### 2.3 Modeling $P_{lux}$ and $P_{BAD}$ Promoter Activity

Transcription factor (TF) binding to promoters is modeled according to the Shea-Ackers formalism<sup>3,4</sup>. The total expression  $P_T$  from a promoter is described by a weighted sum of the basal level probability ( $1-P$ ) and the induced level probability  $P$ :

$$P_T = Const_1 \cdot (1 - P) + Const_2 \cdot P \rightarrow P_T = Const_1 + (Const_2 - Const_1) \cdot P, \quad (17)$$

where  $Const_1$  and  $Const_2$  are constants that correspond to basal or induced expression respectively. In this study we used two activator-type transcription factors: LuxR<sup>5</sup> and AraC<sup>6</sup>. The probability of the Lux promoter ( $P_{lux}$ ) being induced is described by the following equation:

$$P = \frac{\frac{LuxR_C}{K_d}}{1 + \frac{LuxR_C}{K_d}}, \quad (18)$$

where  $K_d$  is the dissociation constant for the binding of the inducer-transcription factor (AHL-LuxR) complex ( $LuxR_C$ ) to the promoter  $P_{lux}$ . The concentration of the bound-promoter complex (AHL-LuxR- $P_{lux}$ ) is directly proportional to the probability of the promoter being induced and the concentration of promoter binding sites ( $O_T$ ):

$$LuxR_{Cb} = O_T \cdot \frac{\frac{LuxR_C}{K_d}}{1 + \frac{LuxR_C}{K_d}} \quad (19)$$

The sum of the free (AHL-LuxR) complex ( $LuxR_C$ ) and bound (AHL-LuxR) complex ( $LuxR_{Cb}$ ) are equal to the total (AHL-LuxR) complex  $LuxR_{CT}$ :

$$LuxR_{CT} = LuxR_C + LuxR_{Cb} \quad (20)$$

The  $P_{\text{BAD}}$  promoter is activated by the AraC transcription factor when it is induced by arabinose. The probability of the  $P_{\text{BAD}}$  promoter being induced by the arabinose-AraC complex is described by the following equation<sup>7</sup>:

$$P = \frac{\frac{\text{AraC}_C}{K_d}}{1 + \frac{\text{AraC}_C}{K_d} + \frac{\text{AraC}}{K_{df}}}, \quad (21)$$

where  $\text{AraC}_C$  is the concentration of the arabinose-AraC complex,  $\text{AraC}$  is the concentration of free AraC transcription factor,  $K_d$  is the dissociation constant for binding of the arabinose-AraC complex to the  $P_{\text{BAD}}$  promoter, and  $K_{df}$  is the dissociation constant for free AraC binding to  $P_{\text{BAD}}$ . The probability of free AraC binding to the promoter is equal to:

$$P = \frac{\frac{\text{AraC}}{K_{df}}}{1 + \frac{\text{AraC}_C}{K_d} + \frac{\text{AraC}}{K_{df}}} \quad (22)$$

The concentration of the bound-promoter complex arabinose-AraC- $P_{\text{BAD}}$  ( $\text{AraC}_{Cb}$ ) is directly proportional to the probability of the promoter being induced and the number of the promoter binding sites ( $O_T$ ):

$$\text{AraC}_{Cb} = O_T \cdot \frac{\frac{\text{AraC}_C}{K_d}}{1 + \frac{\text{AraC}_C}{K_d} + \frac{\text{AraC}}{K_{df}}} \quad (23)$$

The concentration of the bound AraC ( $\text{AraC}_b$ ) to the promoter is directly proportional to the probability of binding the free AraC to the promoter and the number of the promoter binding sites:

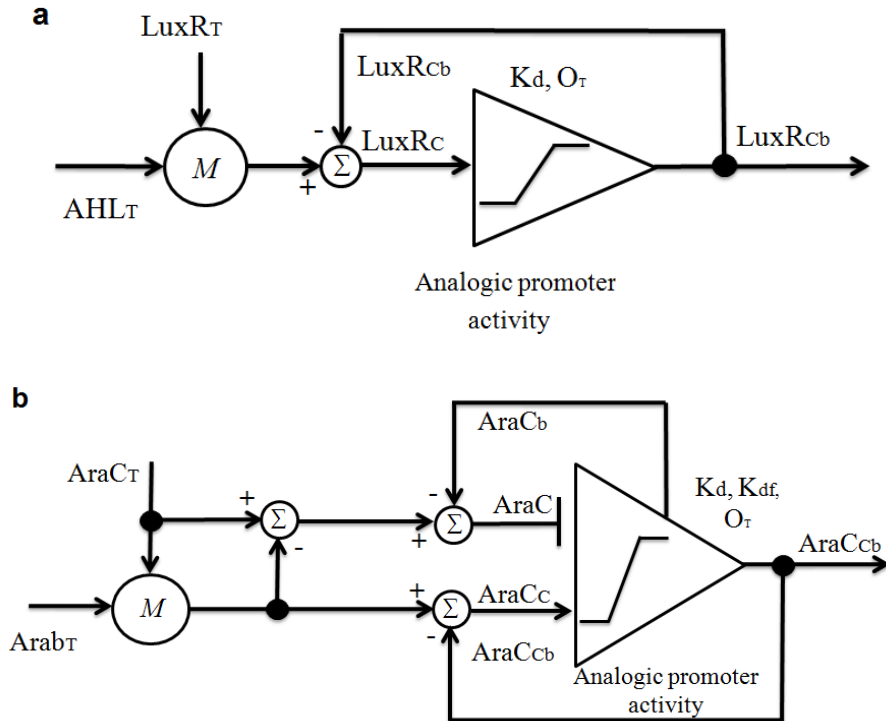
$$\text{AraC}_b = O_T \cdot \frac{\frac{\text{AraC}}{K_{df}}}{1 + \frac{\text{AraC}_C}{K_d} + \frac{\text{AraC}}{K_{df}}} \quad (24)$$

The sum of the free (arabinose-AraC) complex ( $\text{AraC}_C$ ) and bound (arabinose-AraC) complex ( $\text{AraC}_{Cb}$ ) to DNA is equal to the total (arabinose-AraC) complex  $\text{AraC}_{CT}$ , and the sum of free AraC ( $\text{AraC}$ ) and bound AraC ( $\text{AraC}_b$ ) to DNA is equal to  $\text{AraC}_T - \text{AraC}_{CT}$ :

$$\text{AraC}_{CT} = \text{AraC}_C + \text{AraC}_{Cb} \quad (25)$$

$$\text{AraC}_T - \text{AraC}_{CT} = \text{AraC} + \text{AraC}_b \quad (26)$$

Supplementary Figure 2 shows schematic diagrams for the models of promoter activity for LuxR and AraC, including the binding reaction which forms the complex between the inducer and the transcription factor. In our models, the expression of the output protein is proportional to the bound transcription factor complex ( $\text{LuxR}_{Cb}$  and  $\text{AraC}_{Cb}$ ).

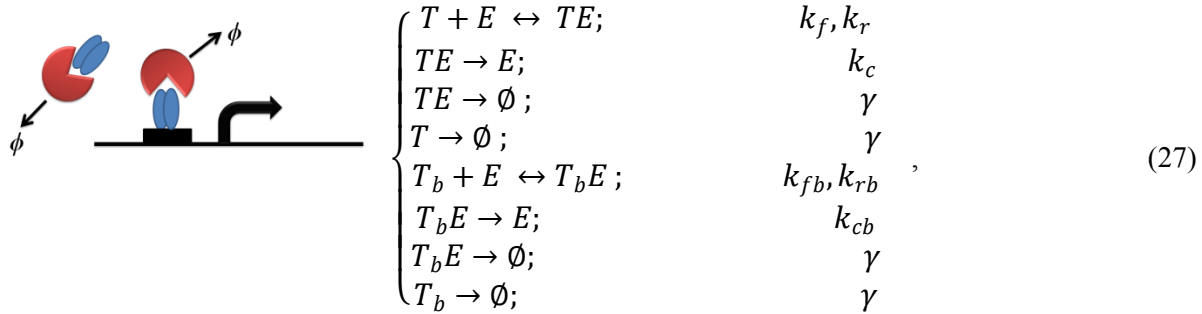


**Supplementary Figure 2.** Schematic diagram models of “analogic” promoter activity for (a) LuxR and (b) AraC.

Supplementary Figures 2a and 2b also show the effect of local negative feedback (the loops that subtract from the adders in Supplementary Figure 2) that is ubiquitous in chemical binding (Eq. 24): when a free molecule binds to another, it gets used up such that less free molecule is available to bind, lowering its level. The ‘analogic’ promoter in Supplementary Figure 2 models the linear as well as saturating behavior seen at DNA promoters as described by Equations 17–24. Note that AraC has a repressory effect when it is not bound to the inducer but has an activatory effect when it is bound to the inducer in Supplementary Figure 2b.

#### 2.4 Modeling of Degradation Rates in the Presence of Binding Sites

In our models as in others, free and DNA-bound transcription factor degrade at different rates<sup>8</sup>. Generally DNA can protect a transcription factor from degradation, thereby decreasing its degradation rate. The degradation process for a transcription factor can be described by the following reactions<sup>9,10</sup>:



where  $T$  is the concentration of free transcription factor;  $T_b$  is the concentration of transcription factor bound to DNA;  $E$  is the concentration of free protein-degrading enzyme;  $k_f$  and  $k_{fb}$  are the forward reaction rates of the binding of free transcription factor and DNA-bound transcription factor to the protein-degrading enzyme, respectively;  $k_r$  and  $k_{rb}$  are the reverse reaction rates of the binding of free transcription factor and DNA-bound transcription factor to the protein-degrading enzyme, respectively;  $k_c$  and  $k_{cb}$  are the forward reaction rates of enzyme function and release for the enzyme-free-transcription-factor complex and the enzyme-DNA-bound-transcription-factor-complex, respectively; and  $\gamma$  is the dilution rate of total transcription factor due to cell growth. We assume that the degradation rate is not directly affected by the binding of inducers to transcription factors.

The set of ordinary differential equations which model the degradation process is:

$$\frac{dTE}{dt} = k_f \cdot T \cdot E - k_r \cdot TE - k_c \cdot TE - \gamma \cdot TE \quad (28.1)$$

$$\frac{dT}{dt} = -k_f \cdot T \cdot E + k_r \cdot TE - \gamma \cdot T \quad (28.2)$$

$$\frac{dT_bE}{dt} = k_{fb} \cdot T_b \cdot E - k_{rb} \cdot T_bE - k_{cb} \cdot T_bE - \gamma \cdot T_bE \quad (28.3)$$

$$\frac{dT_b}{dt} = -k_{fb} \cdot T_b \cdot E + k_{rb} \cdot T_bE - \gamma \cdot T_b \quad (28.4)$$

In steady state  $dTE/dt=0$ ,  $dT_bE/dt=0$ , which leads to:

$$TE = \frac{T \cdot E}{K}; \quad \text{where } K = \frac{k_r + k_c + \gamma}{k_f} \quad (29.1)$$

$$T_bE = \frac{T_b \cdot E}{K_b}; \quad \text{where } K_b = \frac{k_{rb} + k_{cb} + \gamma}{k_{fb}} \quad (29.2)$$

The decay of free and bound transcription factor can be expressed by:

$$\frac{dT}{dt} = -k_f \cdot T \cdot E + k_r \cdot TE - \gamma \cdot T = -(k_c + \gamma) \cdot TE - \gamma \cdot T \quad (30.1)$$

$$\frac{dT_b}{dt} = -k_{fb} \cdot T_b \cdot E + k_{rb} \cdot T_bE - \gamma \cdot T_b = -(k_{cb} + \gamma) \cdot T_bE - \gamma \cdot T_b \quad (30.2)$$

Substituting Eq. 29 into Eq. 30, we get:

$$\frac{dT}{dt} = -\frac{(k_c + \gamma)}{K} \cdot T \cdot E - \gamma \cdot T \quad (31.1)$$

$$\frac{dT_b}{dt} = -\frac{(k_{cb} + \gamma)}{K_b} \cdot T_b \cdot E - \gamma \cdot T_b \quad (31.2)$$

The sum of free protein-degrading enzyme  $E$  and bound enzyme to the transcription factors ( $TE$  and  $T_bE$ ) is equal to the total enzyme concentration ( $E_T$ ):

$$E_T = E + TE + T_bE \quad (32)$$

Substituting Eq. 29.1 and Eq. 29.2 into Eq. 32, we can express the concentration of free protein-degrading enzyme as:

$$E = \frac{E_T}{1 + \frac{T}{K} + \frac{T_b}{K_b}} \quad (33)$$

In the general case where there are multiple protein species that are degraded by enzyme  $E$ , the concentration of free protein-degrading enzyme can be described as:

$$E = \frac{E_T}{1 + \sum_i \frac{T_i}{K_i} + \sum_j \frac{T_{bj}}{K_{bj}}} \quad (34)$$

Where  $i$  pertains to different free proteins and transcription factors, and  $j$  is different bound transcription factors to DNA. In this model, the degradation of free transcription factors or proteins is significantly faster than the degradation of bound transcription factors to DNA such that most protein-degrading enzyme is typically free or associated with bound transcription factors. Therefore, if we assume that  $T_i/K_i \ll T_{bj}/K_{bj}$  the free protein-degrading enzyme concentration can be expressed by:

$$E = \frac{E_T}{1 + \sum_j \frac{T_{bj}}{K_{bj}}} \quad (35)$$

Substituting the general form of the free protein-degrading enzyme concentration (Eq. 35) into Eq. 31, the general decay of free and bound transcription factors can be modeled as:

$$\frac{dT_i}{dt} = -\mu_i \cdot T_i - \gamma \cdot T_i \quad (36.1)$$

$$\frac{dT_{bi}}{dt} = -\mu_{bi} \cdot T_{bi} - \gamma \cdot T_{bi}, \quad (36.2)$$

where:

$$\mu_i = \frac{(k_{ci} + \gamma)}{K} \frac{E_T}{\left(1 + \sum_j \frac{T_{bj}}{K_{bj}}\right)} \quad (37.1)$$

$$\mu_{bi} = \frac{(k_{cbi} + \gamma)}{K_{bi}} \frac{E_T}{\left(1 + \sum_j \frac{T_{bj}}{K_{bj}}\right)} \quad (37.2)$$

## 2.5 Modeling Transcription Factor Expression in the Presence of Binding Sites

The steady-state mass action model assumes that there is a balance between the overall production rate and the degradation rate of the transcription factor<sup>8</sup>:

$$\frac{dT_{Ti}}{dt} = G - \mu_i \cdot T_i - \mu_{bi} \cdot T_{bi} - \gamma \cdot T_i - \gamma \cdot T_{bi}, \quad (38)$$

where  $G$  is the total production rate. The sum of the free and the bound forms of transcription factor to DNA is equal to the total transcription factor ( $T_{Ti} = T_i + T_{bi}$ ):

$$\frac{1}{\mu_i + \gamma} \cdot \frac{dT_{Ti}}{dt} = \frac{G}{\mu_i + \gamma} - T_{Ti} + T_{bi} \frac{\mu_i}{\mu_i + \gamma} \cdot \left(1 - \frac{\mu_{bi}}{\mu_i}\right) \quad (39)$$

In steady state we get:

$$T_{Ti} = \frac{G}{\mu_{eff}} + T_{bi} \cdot \theta_i \quad (40)$$

Where  $\mu_{eff}$  is given by:

$$\mu_{eff} = \mu_i + \gamma = \mu_{oi} \left( \frac{1}{1 + \sum_j \frac{T_{bj}}{K_{bj}}} + \frac{\gamma}{\mu_{oi}} \right) \quad (41)$$

Where  $\mu_{oi} = \frac{(k_c + \gamma)}{K} \cdot E_T$ , and the “protection parameter”  $\theta_i = \frac{\mu_i}{\mu_i + \gamma} \left(1 - \frac{\mu_{bi}}{\mu_i}\right)$ . The protection parameter generally varies in the range  $0 \leq \theta_i \leq 1$ , with two extreme cases:

1.  $\theta = 0$ : this situation can occur when the degradation rate of the bound TF is equal to the degradation rate of the free TF ( $\mu_{bi} = \mu_i$ ) or when the dilution rate dominates over the degradation rate ( $\gamma \gg \mu_i$ ).
2.  $\theta = 1$ : this situation can occur when the degradation of the bound TF is very slow compared to the degradation of the free TF, and the dilution rate is negligible compared with the free TF degradation rate.

## 2.6 Positive-Feedback Model

Positive-feedback loops are commonly used motifs in genetic circuits and depending on their context exhibit different behavior, including bi-stability in toggle-switch circuits<sup>11</sup> and hysteresis in digital memory devices<sup>12</sup>. While positive feedback has many different forms, the simplest form of genetic positive feedback is the production of a transcriptional activator by its promoter

(Supplementary Figure 3a and 3c): when an inducer (AHL/AraB) binds to an input transcription factor (LuxR/AraC), the resulting complex can bind to a promoter ( $P_{lux}/P_{BAD}$ ) to stimulate expression of output transcription factors. If these output transcription factors are identical to the input transcription factors (LuxR/AraC), then a positive-feedback loop is created. High values of  $\theta$  increase the effect of positive feedback through reduced degradation.

A schematic diagram that represents LuxR positive feedback is shown in Supplementary Figure 3b, where the total production rate and the degradation rate are calculated from Eq. 17 and Eq. 41 and shown below:

$$G = g \cdot (LuxR_{Cb} + Basal) \quad (42.1)$$

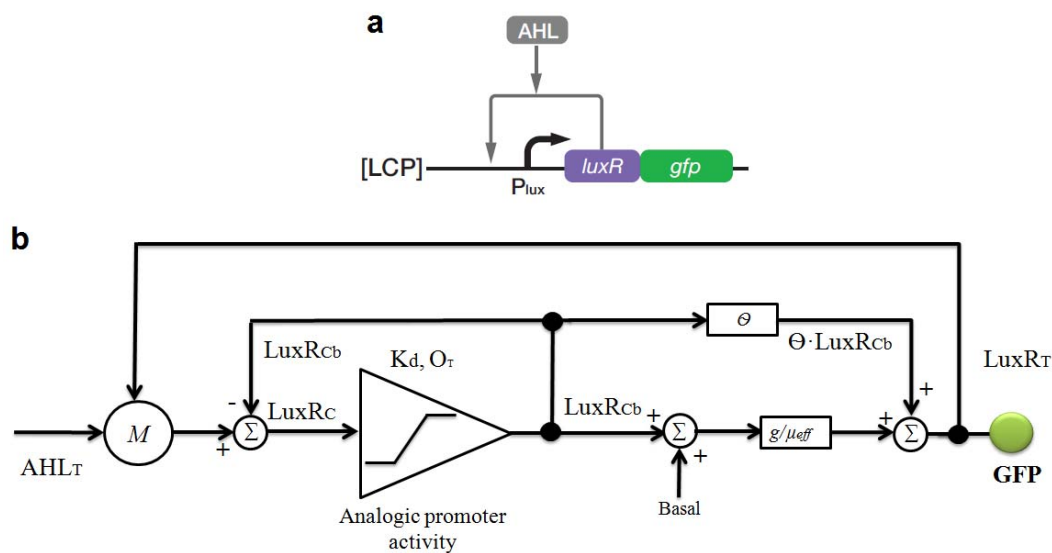
$$\mu_{eff} = \mu_0 \left( \frac{\gamma}{\mu_0} + \frac{1}{1 + \frac{LuxR_{Cb}}{K_b}} \right) \quad (42.2)$$

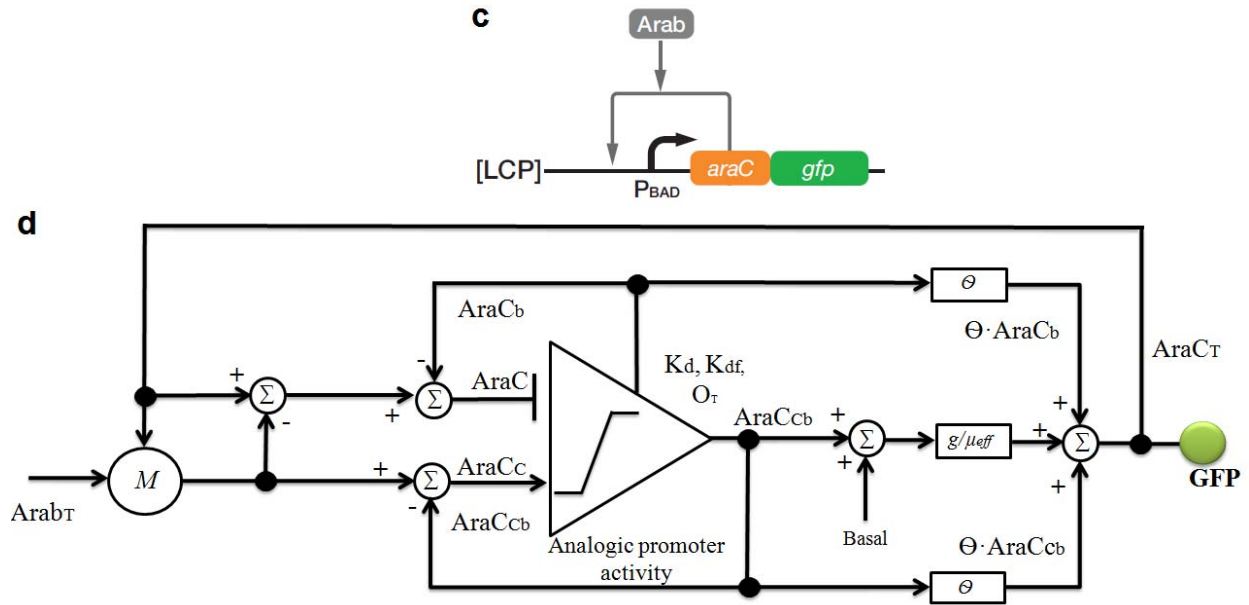
where  $g$  is the production rate for induced promoter expression and  $Basal$  is the basal level. Similarly, the schematic diagram for AraC positive feedback is shown in Supplementary Figure 3d, where the total production rate and the degradation rate are calculated according to Eq. 17, Eq. 22-26, and Eq. 41 and shown below:

$$G = g \cdot (AraC_{Cb} + Basal) \quad (43.1)$$

$$\mu_{eff} = \mu_0 \left( \frac{\gamma}{\mu_0} + \frac{1}{1 + \frac{AraC_{Cb} + AraC_b}{K_b}} \right) \quad (43.2)$$

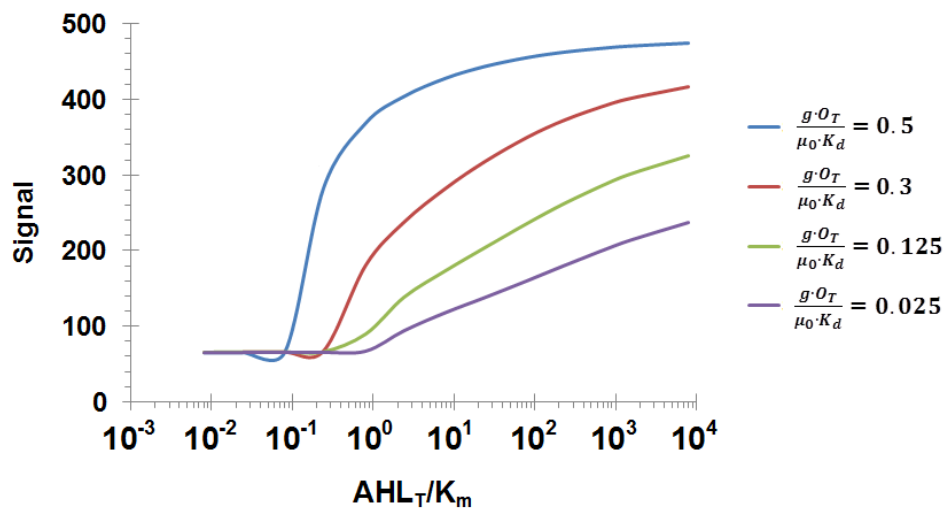
The modeling and experimental results are presented in Supplementary Figure 6.





**Supplementary Figure 3.** Positive-feedback circuits. (a) Genetic circuit for LuxR, (b) analog schematic diagram for the LuxR system, (c) genetic circuit for AraC, (d) analog schematic diagram for the AraC system.

Supplementary Figure 4 shows the influence of increasing  $K_d$  (the dissociation of the AHL-LuxR complex to the promoter) on the positive-feedback signal. When  $K_d$  increases, the input dynamic range increases and the signal output decreases. To increase  $K_d$  but maintain signals at a high level, we constructed a positive-feedback-and-shunt (PF-Shunt) circuit: The shunt circuit helps maintain a low  $K_d$  while the positive feedback increases signal levels.



**Supplementary Figure 4.** Simulation results of our positive-feedback circuit versus inducer concentration for different values of  $K_d$ .

## 2.7 Positive Feedback and Shunt Model (PF-Shunt)

The shunt circuit with positive feedback is illustrated in Supplementary Figure 6a. The contribution of the shunt on the performance of the circuit can be summarized as follows:

### 1. Increasing the number of binding sites for transcription factors:

$$\text{I. For LuxR } \mu_{eff} = \mu_0 \left( \frac{\gamma}{\mu_0} + \frac{1}{1 + \frac{LuxR_{cb1} + LuxR_{cb2}}{K_b}} \right)$$

$$\text{For AraC } \mu_{eff} = \mu_0 \left( \frac{\gamma}{\mu_0} + \frac{1}{\left(1 + \frac{AraC_{cb1} + AraC_{cb2} + AraC_{b1} + AraC_{b2}}{K_b}\right)} \right)$$

$$\text{II. For LuxR : } LuxR_{CT} = LuxR_C + LuxR_{Cb1} + LuxR_{Cb2}$$

$$\text{For AraC: } AraC_{CT} = AraC_C + AraC_{Cb1} + AraC_{Cb2}$$

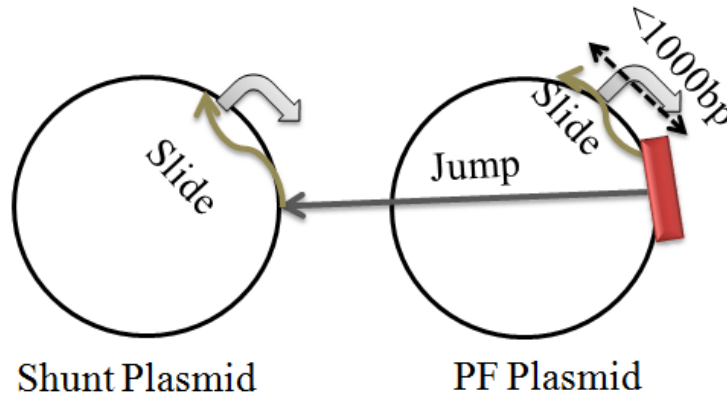
$$AraC_T - AraC_{CT} = AraC + AraC_{b1} + AraC_{b2}$$

$$\text{III. For LuxR : } LuxR_T = \frac{g}{\mu_{eff}} + LuxR_{Cb1} \cdot \theta + LuxR_{Cb2} \cdot \theta$$

$$\text{For AraC: } AraC_T = \frac{g}{\mu_{eff}} + AraC_{Cb1} \cdot \theta + AraC_{b1} \cdot \theta + AraC_{Cb2} \cdot \theta + AraC_{b2} \cdot \theta$$

where subscripts with “1” refer to the positive-feedback plasmid and subscripts with “2” refer to the shunt plasmid.

2. **Increasing plasmid copy number and changing the diffusion time of the transcription factors:** There are two ways that transcription factors search for their binding sites: the first is local and fast consisting of hops and slides on DNA, while the second is global and slow consisting of jumps<sup>13</sup>. Supplementary Figure 5 illustrates these concepts. We assume that in the positive-feedback plasmid, the search is mainly local (the distance between the transcription factor production site and the promoter binding site is around 1 Kbp), while in the shunt plasmid, the search is global (the transcription factor needs to jump from the positive-feedback plasmid production site to the shunt-plasmid promoter binding site).



**Supplementary Figure 5.** Transcription factors search for their promoter by sliding and jumping.

In the case that the plasmids are distributed uniform inside the cell, we can assume that the distance between the plasmid copy numbers  $\Delta x$  is approximately equal to  $(V/N)^{1/3}$ , where  $N$  is the total plasmid copy number and  $V$  is the cell volume. Since the jumping of transcription factors between the plasmids is described by a 3D diffusion process, we can express the jumping time as<sup>14</sup>:

$$\tau_{jump} = \frac{\langle \Delta x^2 \rangle}{2 \cdot D} \quad \rightarrow \quad \tau_{jump} = \frac{\left(\frac{V}{N}\right)^{2/3}}{2 \cdot D} \quad (44)$$

The forward reaction rate of TF binding to DNA is inversely proportional to the search time, such that:

$$K_{d1} = K_{-11} \cdot \tau_{slide1} \quad (45.1)$$

$$K_{d2} = K_{-12} \cdot (\tau_{slide2} + \tau_{jump}), \quad (45.2)$$

where  $K_{d1}$  and  $K_{d2}$  are the dissociation constants of the transcription factor for the PF plasmid and shunt plasmid respectively,  $K_{-11}$  and  $K_{-12}$  are proportional to the reverse reaction rates of the transcription factor binding to the promoter of the PF plasmid and shunt plasmid, respectively, and  $\tau_{slide1}$  and  $\tau_{slide2}$  are the sliding times of the transcription factor in the PF plasmid and shunt plasmid, respectively. If we assume that the sliding time is not dependent on the plasmid copy number, then dividing Eq. 45.1 by Eq. 45.2 yields:

$$\frac{K_{d1}}{K_{d2}} = \frac{\rho}{1 + \frac{\beta}{N^{2/3}}} \quad (46.1)$$

$$\frac{\tau_{jump}}{\tau_{slide2}} = \frac{V^{2/3} \cdot k_2}{2 \cdot \ln(2) \cdot D} \cdot \frac{1}{N^{2/3}} \quad \rightarrow \quad \beta = \frac{V^{2/3} \cdot k_2}{2 \cdot \ln(2) \cdot D} \quad (46.2)$$

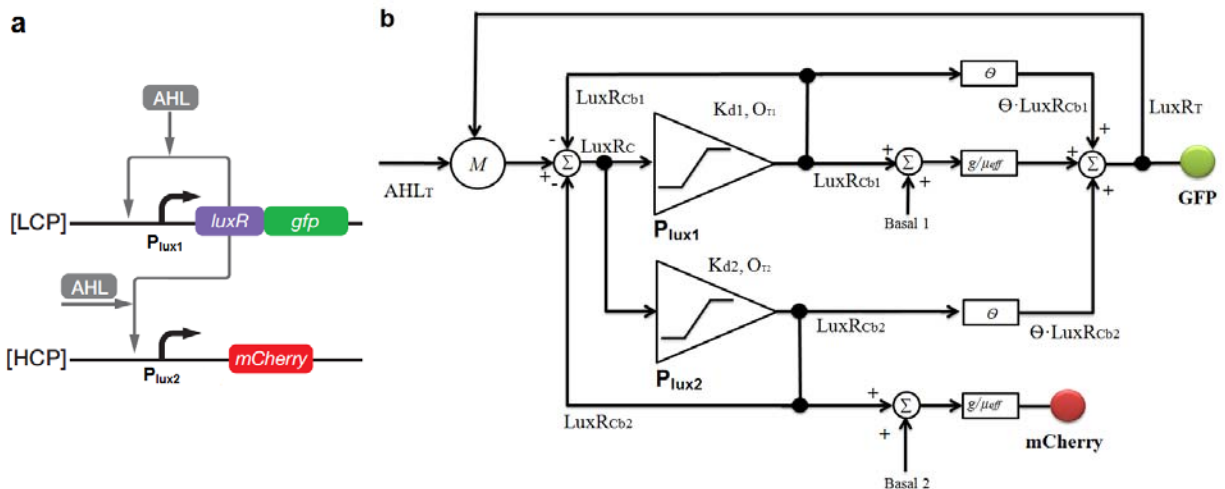
$$\rho = \frac{K_{-11} \cdot \tau_{slide1}}{K_{-12} \cdot \tau_{slide2}} \quad (46.3)$$

where  $D$  is the diffusion coefficient, and  $(k_2 = \ln(2)/\tau_{slide2})$  is a rate constant that describes transcription-factor binding to the shunt-plasmid promoter.

We note two important points:

1. In our models, transcription-factor diffusion processes only influence the  $K_d$  of the shunt plasmid and not that of the PF plasmid. Therefore,  $K_{d1}$  is defined as the reference dissociation constant (when the distance between the TF gene and its cognate binding site on the same plasmid is less than 1 Kbp<sup>13</sup> or the search type is local).
2. When we fit our model (Supplementary Figure 6) to experimental data we found that  $\rho = 1$  indicating that sliding processes within DNA are similar between the plasmids and that it is the jumping across plasmids that leads to differences in  $K_d$  that vary with plasmid copy number.

The experimental and modeling results of the PF-shunt circuit for LuxR and AraC with different copy numbers are presented in Figure 1, Figure 2, and Supplementary Figure 6. The fitting parameters are shown in Supplementary Table 2.





results for the GFP signal of the LuxR circuit. This data appears in Figure 2b in the main text and is reproduced here for clarity; (d) experimental and modeling results for the mCherry signal of the LuxR circuit. This data appears in Figure 2c in the main text and is reproduced here for clarity; (e) PF-shunt genetic circuit for AraC; (f) schematic diagram model for AraC; (g) experimental and modeling results for the GFP signal of the AraC circuit; (h) experimental and modeling results for the mCherry signal of the AraC circuit. This data appears in Figure 1e in the main text and is reproduced here for clarity.

## 2.8 Modeling the $P_{lacO}$ Promoter

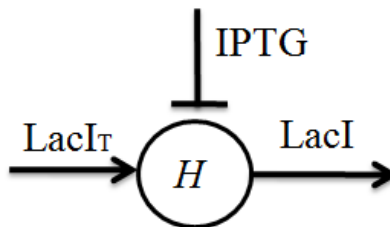
Using transcriptional activators and repressors in multi-component circuits, we developed several synthetic analog gene circuits. The first circuit gives a wide-dynamic-range negative-slope logarithm (Supplementary Figure 31) and the second circuit gives a power law (Figure 3e-3f). In both circuits, we used LacI and its cognate  $P_{lacO}$  promoter. Here, we present our model for the LacI-regulated promoter,  $P_{lacO}$ <sup>15</sup>. To do so, we capture the quantitative relationship between the inducer (IPTG) concentration and the free repressor (LacI) concentration. We can model the free LacI ( $LacI$ ) and the IPTG-LacI complex ( $LacI_C$ ) by a Hill function<sup>7,2</sup>:

$$LacI_C = LacI_T \frac{\left(\frac{IPTG}{K_m}\right)^{h_1}}{1 + \left(\frac{IPTG}{K_m}\right)^{h_1}} \quad (47)$$

Where  $LacI_T$  is the total LacI concentration,  $K_m$  is the dissociation constant between IPTG and LacI, and  $h_1$  is the Hill coefficient which represents cooperativity between IPTG and LacI. The concentration of free LacI is expressed by:

$$LacI = LacI_T - LacI_C \quad (48)$$

Supplementary Figure 7 shows the schematic diagram model of the binding reaction of IPTG and the LacI repressor



**Supplementary Figure 7.** Schematic diagram model of the binding reaction of IPTG and the LacI repressor.

We consider three possible binding states for the  $P_{lacO}$  promoter: (1) The promoter is empty with probability 1, (2) Free LacI repressor is bound to the promoter with probability  $LacI/K_{df}$ , and (3)

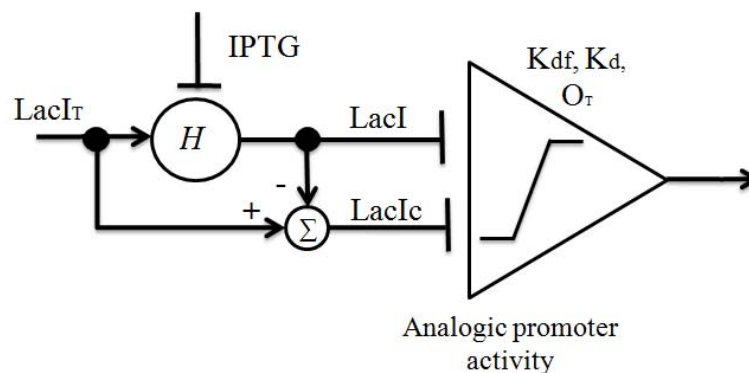
IPTG-LacI complex ( $LacI_C$ ) is bound to the promoter with probability  $LacI_C/K_d$ , where  $K_{df} \ll K_d$ . The probability of the  $P_{lacO}$  promoter being in an open complex  $P$  is described by the following equation:

$$P = \frac{1}{1 + \left(\frac{LacI}{K_{df}}\right)^{ni} + \left(\frac{LacI_C}{K_d}\right)^{ni}}, \quad (49)$$

where  $ni$  represents the cooperativity between LacI and the promoter. In this work we used the  $P_{lacO}$  promoter in two networks:

- A wide-dynamic-range negative-slope logarithm circuit (Supplementary Figure 31): In this case, the IPTG concentration is high such that the majority of the LacI protein is unbound to DNA.
- Power-law circuit (Figure 3e-3f): In this case, the  $P_{lacO}$  promoter is on a low-copy plasmid and LacI is produced from a high-copy plasmid. The IPTG level varies in this circuit.

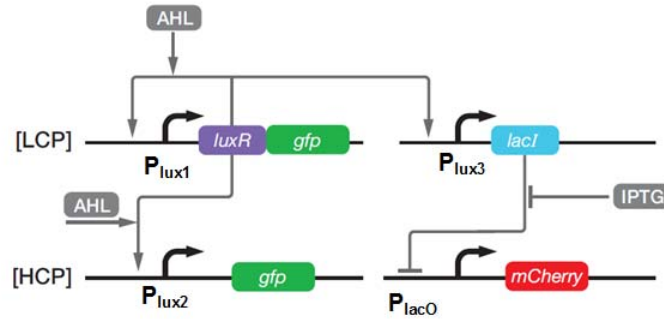
In both cases, we may assume that the DNA-bound LacI is very small compared to the unbound LacI and also that the DNA-bound IPTG-LacI complex is small compared to the unbound IPTG-LacI complex. In this case, we assume a protection parameter  $\Theta = 0$  (Eq. 40). The schematic diagram for  $P_{lacO}$  in steady state is shown in Supplementary Figure 8.



**Supplementary Figure 8.** The schematic diagram of the  $P_{lacO}$  promoter.

## 2.9 Modeling the WDR Negative-Logarithm Circuit

The genetic circuit of the wide-dynamic-range negative-slope is shown in Supplementary Figure 9a. The circuit includes a two-stage cascade; the first stage is the PF-shunt LuxR circuit, which gives a wide-dynamic-range positive slope for expressing LacI, and the second stage is the control of the  $P_{lacO}$  promoter by LacI, which, due to its repressing action, yields a negative slope. Supplementary Figure 9 shows the network diagram of the genetic circuit.



### Supplementary Figure 9. Wide-dynamic-range negative-slope genetic circuit.

The WDR PF-shunt subcircuit of Supplementary Figure 9 is shown in Supplementary Figure 10a. An analog schematic diagram that represents this subcircuit is shown in Supplementary Figure 10b and the modeling and experimental results that correspond to this subcircuit are shown in Supplementary Figure 31b and Supplementary Figure 10c.

The dissociation constant for binding of LuxR to the P<sub>lux</sub> promoter is defined according to Eq. 47. We use  $\frac{K_{d1}}{K_{d2}} = \frac{\rho}{1 + \frac{\beta}{N^{2/3}}}$ , where  $N$  is sum of the high and the low copy number and  $\frac{K_{d1}}{K_{d3}} = \frac{\rho}{1 + \frac{\beta}{N^{2/3}}}$ , where  $N$  is low copy number. Subscripts ‘1’, ‘2’, and ‘3’ correspond to the P<sub>lux1</sub>, P<sub>lux2</sub>, and P<sub>lux3</sub> promoters in Supplementary Figure 9. Since the number of DNA binding sites for the LuxR transcription factor at sites 1 and 3 are identical, we use values for  $O_{T3} = O_{T1}$ .

The experimental characterization and the modeling results of the P<sub>lacO</sub> promoter are shown in Supplementary Figure 11. The total production rate of LacI is calculated according to:

$$G = g \cdot O_T \cdot P, \quad (50)$$

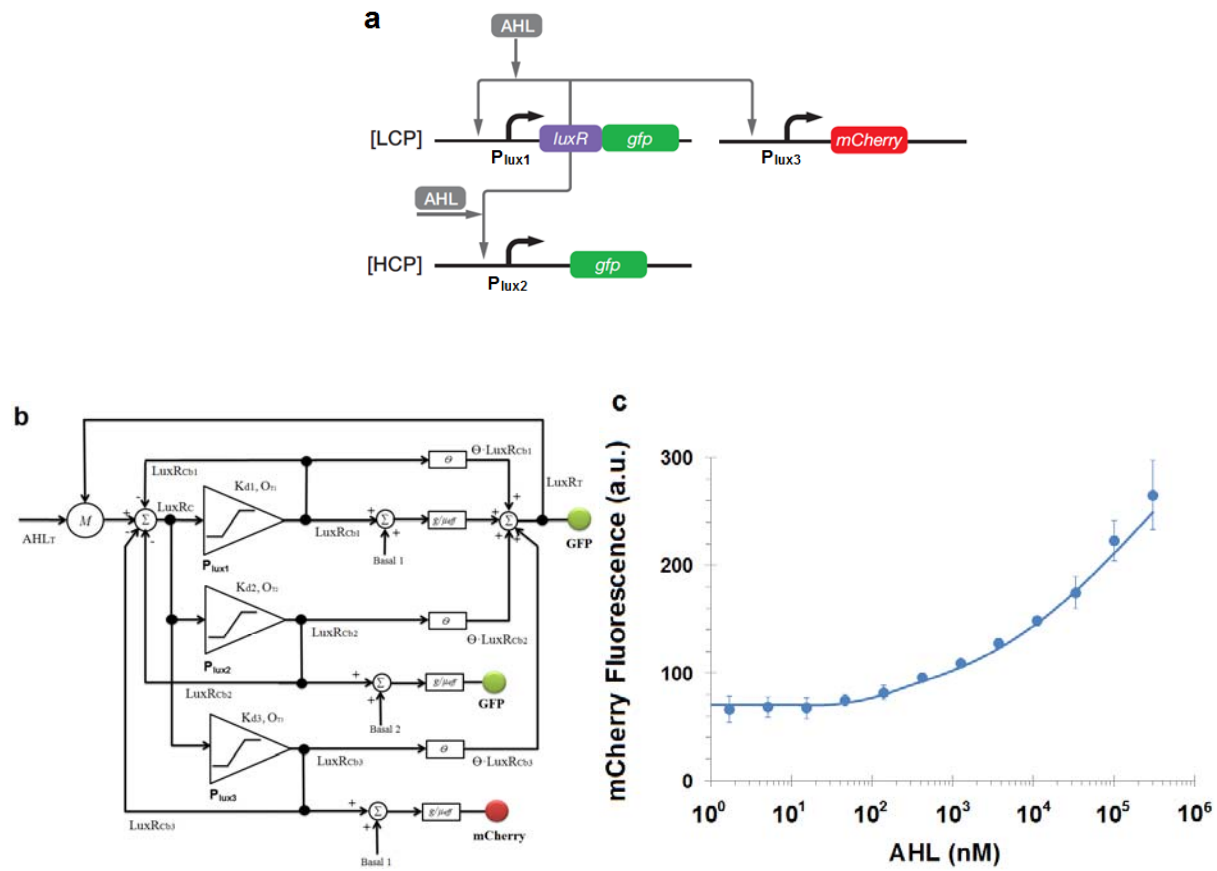
where  $g$  is the production rate,  $O_T$  is number of P<sub>lacO</sub> binding sites, and  $P$  is the probability of the P<sub>lacO</sub> promoter being in an open complex (Eq. 49). Since the output of the P<sub>lacO</sub> promoter is the mCherry reporter protein, the degradation rate is calculated according to:

$$\mu_{eff} = \mu_0 + \gamma \quad (51)$$

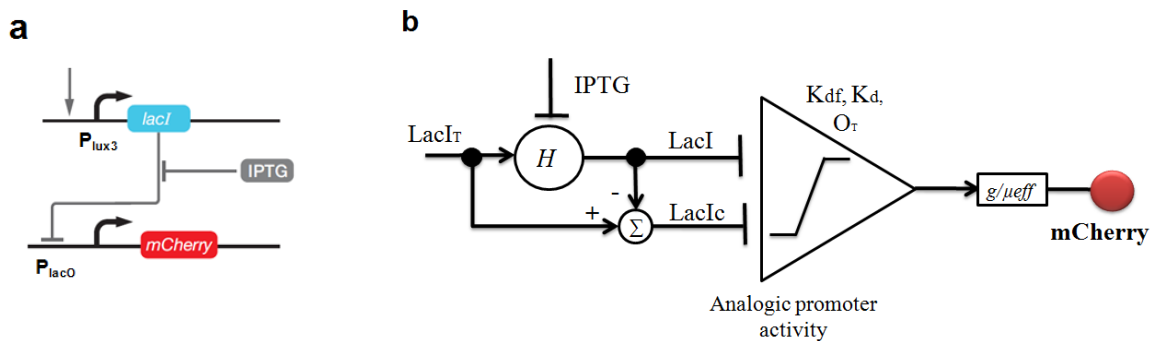
Model parameters are listed in Table 2. We found that the ratio  $\frac{K_{df}}{K_d} = 9 \times 10^{-4}$  is consistent with published parameters<sup>16</sup>.

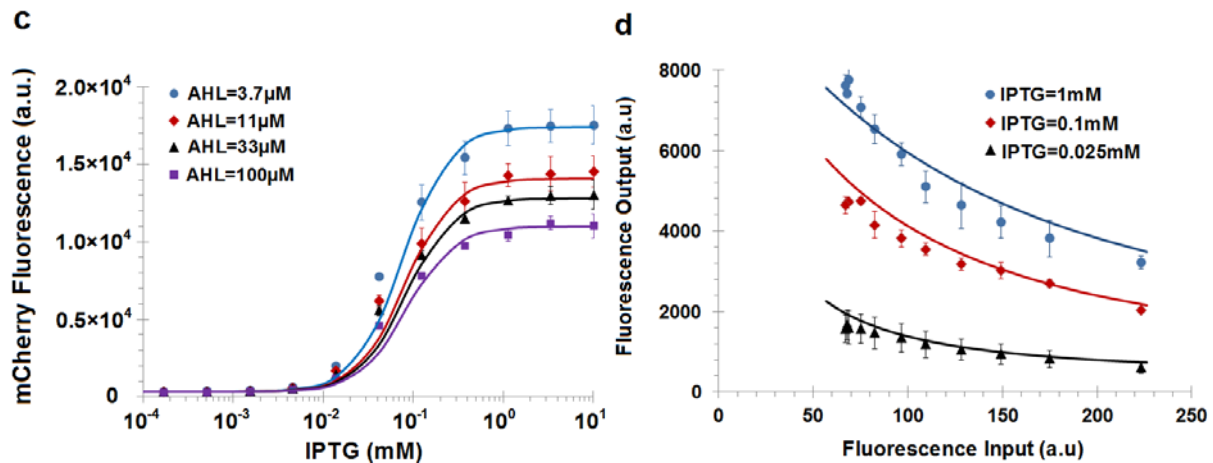
By combining the WDR PF-shunt subcircuit of Supplementary Figure 10 and the P<sub>lacO</sub> module of Supplementary Figure 31d and Supplementary Figure 11, we achieve a wide-dynamic-range negative-slope logarithm circuit as shown in Supplementary Figure 9. The experimental and

modeling results of this overall wide-dynamic-range negative-slope circuit are presented in Supplementary Figure 31 and Supplementary Figure 12.

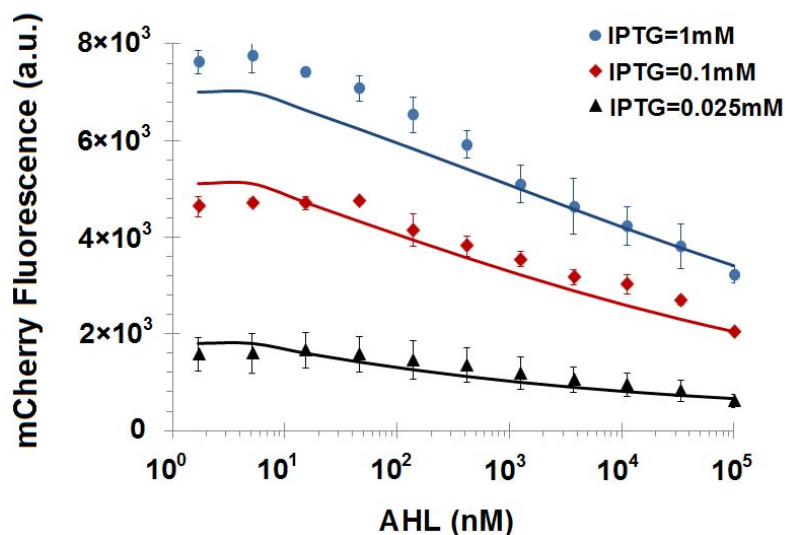


**Supplementary Figure 10.** Wide-dynamic-range PF-shunt subcircuit. (a) Genetic circuit; (b) analog schematic diagram; (c) experimental and modeling results. This data appears in Supplementary Figure 31b and is reproduced here for clarity.





**Supplementary Figure 11.** Characterization of the  $P_{\text{lacO}}$  promoter. (a) Genetic circuit; (b) analog schematic diagram; (c) experimental and modeling results as a function of IPTG. This data appears in Supplementary Figure 31f and is reproduced here for clarity; (d) experimental and modeling results as a function of LacI. This data appears in Supplementary Figure 31d and is reproduced here for clarity.



**Supplementary Figure 12.** Experimental and modeling results for our wide-dynamic-range negative-slope circuit. This same data appears in Supplementary Figure 31g and is reproduced here for clarity.

### 2.10 Modeling the Power Law Circuit

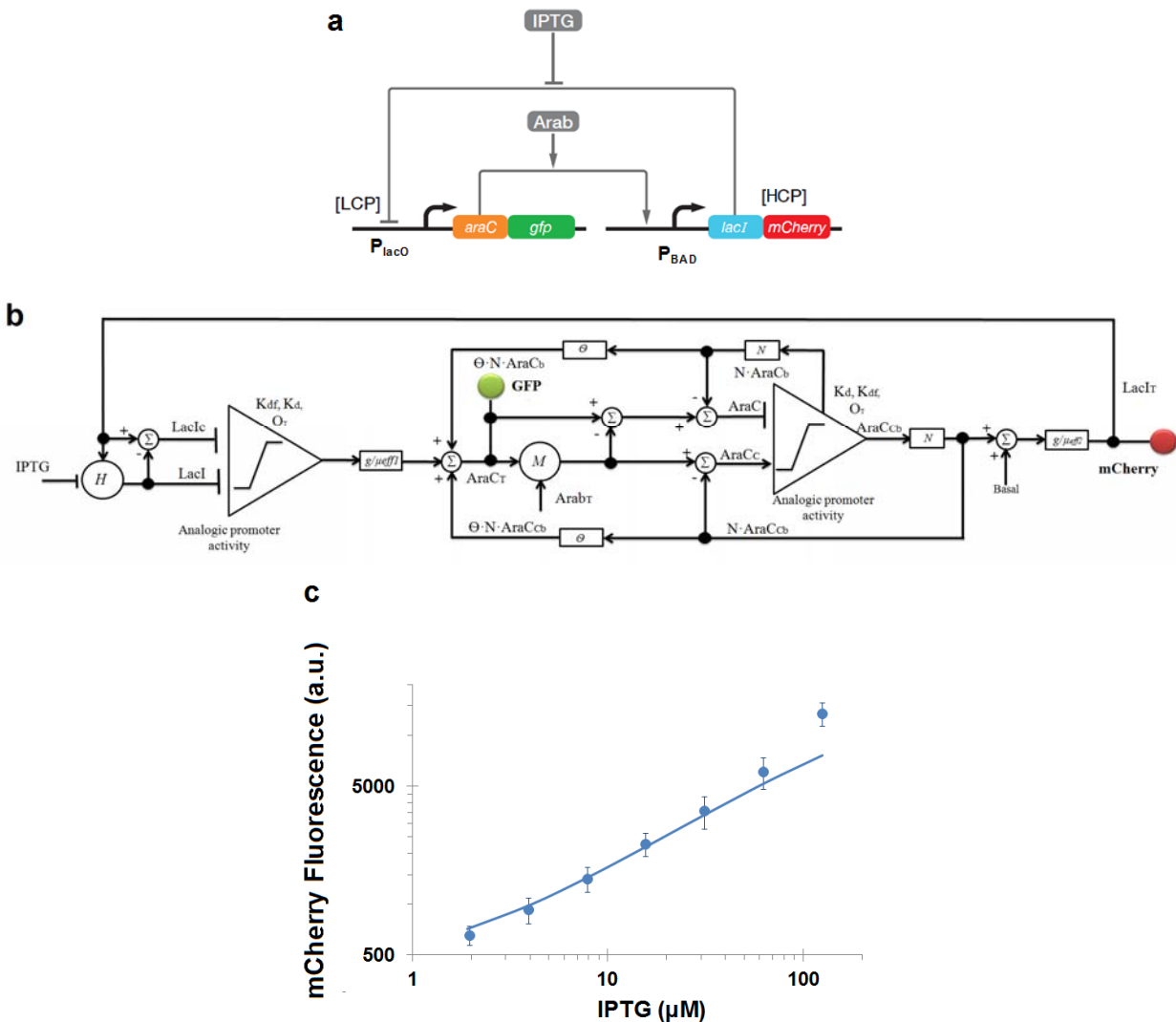
We used negative feedback to create a genetic power-law circuit (Figure 3e and Supplementary Figure 13a). The circuit includes a two-stage cascade with negative feedback where the first stage involves an AraC- $P_{\text{BAD}}$  feedforward path and the second stage involves a LacI- $P_{\text{lacO}}$

feedback path. The analog schematic diagram of the power-law function circuit is presented in Supplementary Figure 13b, where:

$$\mu_{eff1} = \mu_0 \left( \frac{\gamma}{\mu_0} + \frac{1}{\left(1 + \frac{AraC_{cb1} + AraC_{cb2} + AraC_{b1} + AraC_{b2}}{K_b}\right)} \right) \quad (52.1)$$

$$\mu_{eff2} = \mu_0 + \gamma \quad (52.2)$$

$N$  is the copy number of the high copy plasmid (HCP). The experimental and modeling results of the power-law circuit are shown in Figure 3f and Supplementary Figure 13d.

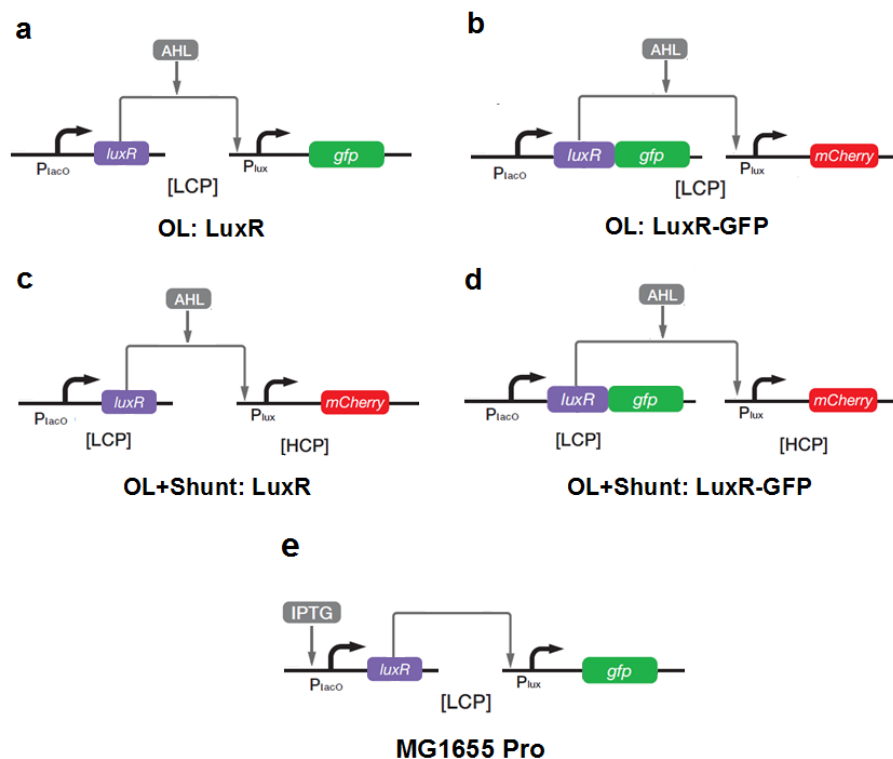


**Supplementary Figure 13.** Power law circuit. (a) Genetic circuit, (b) analog schematic diagram model, (c) experimental and model results. This data appears as Figure 3f in the main text and is reproduced here for clarity.

### 3 Supplementary Experiments

#### 3.1 *LuxR*-Based Open Loop Circuits

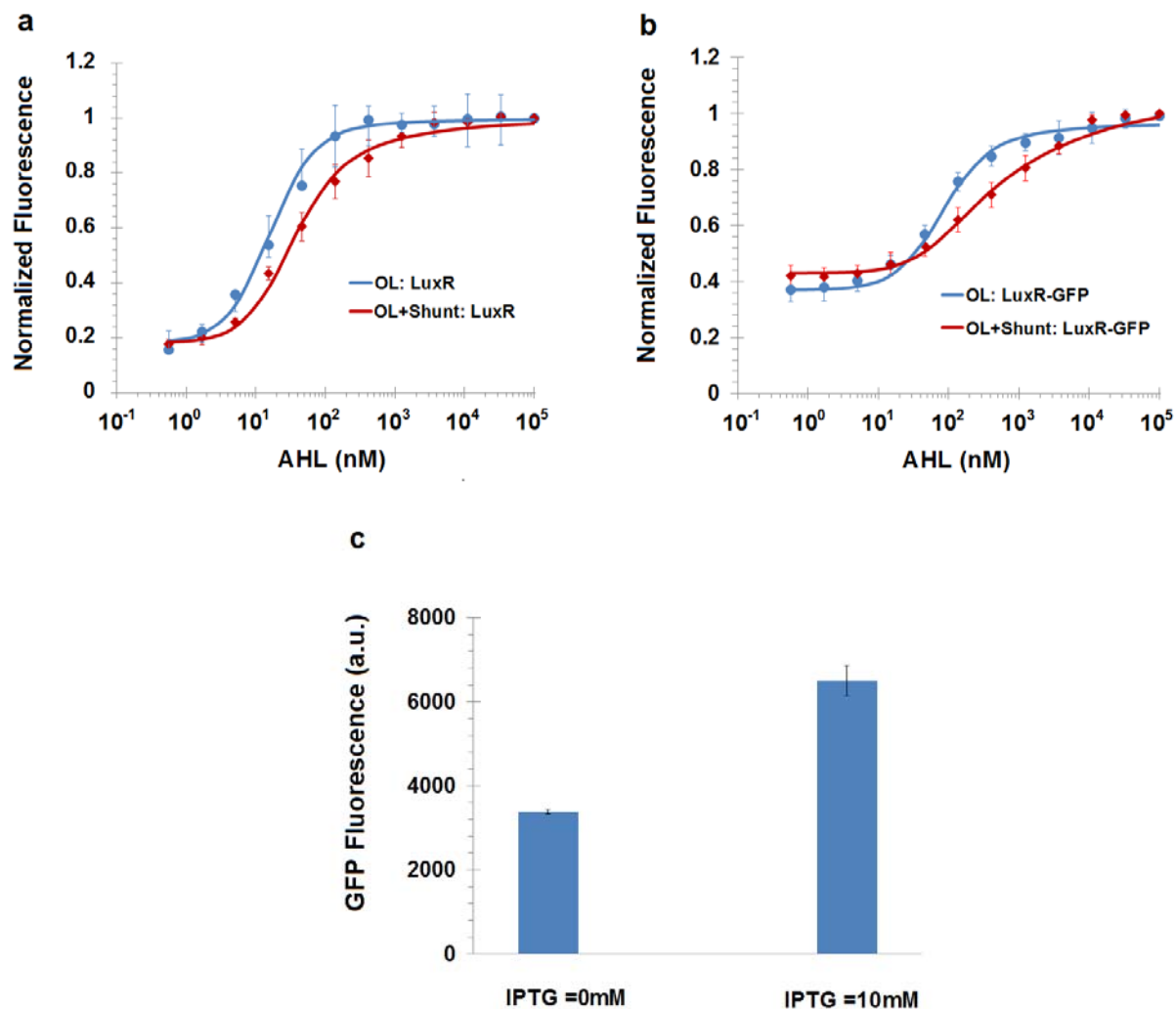
We constructed four open loop circuits to test the effect of adding a shunt plasmid. The first circuit is shown in Supplementary Figure 14a, where the transcription factor and its promoter are on the same low-copy plasmid (LCP). The second circuit is shown in Supplementary Figure 14c, where the transcription factor is on a LCP and its promoter is on a different high-copy plasmid (HCP). In Supplementary Figures 14b and 14d, we fused *LuxR* to GFP and repeated the LCP and HCP experiments of Supplementary Figures 14a and 14c respectively.



**Supplementary Figure 14.** Different topologies for open-loop (OL) circuits with a  $P_{lux}$  promoter. (a) Both the transcription factor *LuxR*, under the control of the  $P_{lacO}$  promoter, and the output signal *GFP*, under the control of the  $P_{lux}$  promoter, are expressed from the same low-copy plasmid (LCP). (b) The transcription factor *LuxR*, under the control of the  $P_{lacO}$  promoter, is expressed from a LCP and the output signal *mCherry*, under the control of the  $P_{lux}$  promoter, is expressed from a HCP. (c) Both the transcription factor *LuxR* fused to *GFP*, under the control of the  $P_{lacO}$  promoter, and the output signal *mCherry*, under the control of the  $P_{lux}$  promoter, are expressed from the same plasmid (LCP). (d) The transcription factor *LuxR* fused to *GFP*, under the control of the  $P_{lacO}$  promoter, is expressed from a LCP and the output signal *mCherry*, under the control of the  $P_{lux}$  promoter, is expressed from a HCP. (e) To demonstrate that *LuxR* does not exhibit repression at the  $P_{lux}$  promoter in the absence of AHL, we placed *LuxR* under the control

of the  $P_{lacO}$  promoter and GFP under the control of the  $P_{lux}$  promoter. Both of these components were located on the same low-copy plasmid. Testing of this circuit was performed in MG1655 Pro cells, where the LacI repressor is constitutively expressed and represses the  $P_{lacO}$  promoter. Expression from the  $P_{lacO}$  promoter can be induced by the addition of IPTG.

The experimental and modeling results of the open-loop circuits are shown in Supplementary Figure 15. In Supplementary Figure 15a and 15b, the concentration of the inducer AHL was varied and the expression of mCherry or GFP was measured. Model parameters are shown in Supplementary Table 2. In Supplementary Figure 15c, we tested GFP fluorescence of the circuit without any addition of AHL to demonstrate that high levels of LuxR expression (IPTG = 10 mM) led to no repression of the  $P_{lux}$  promoter.

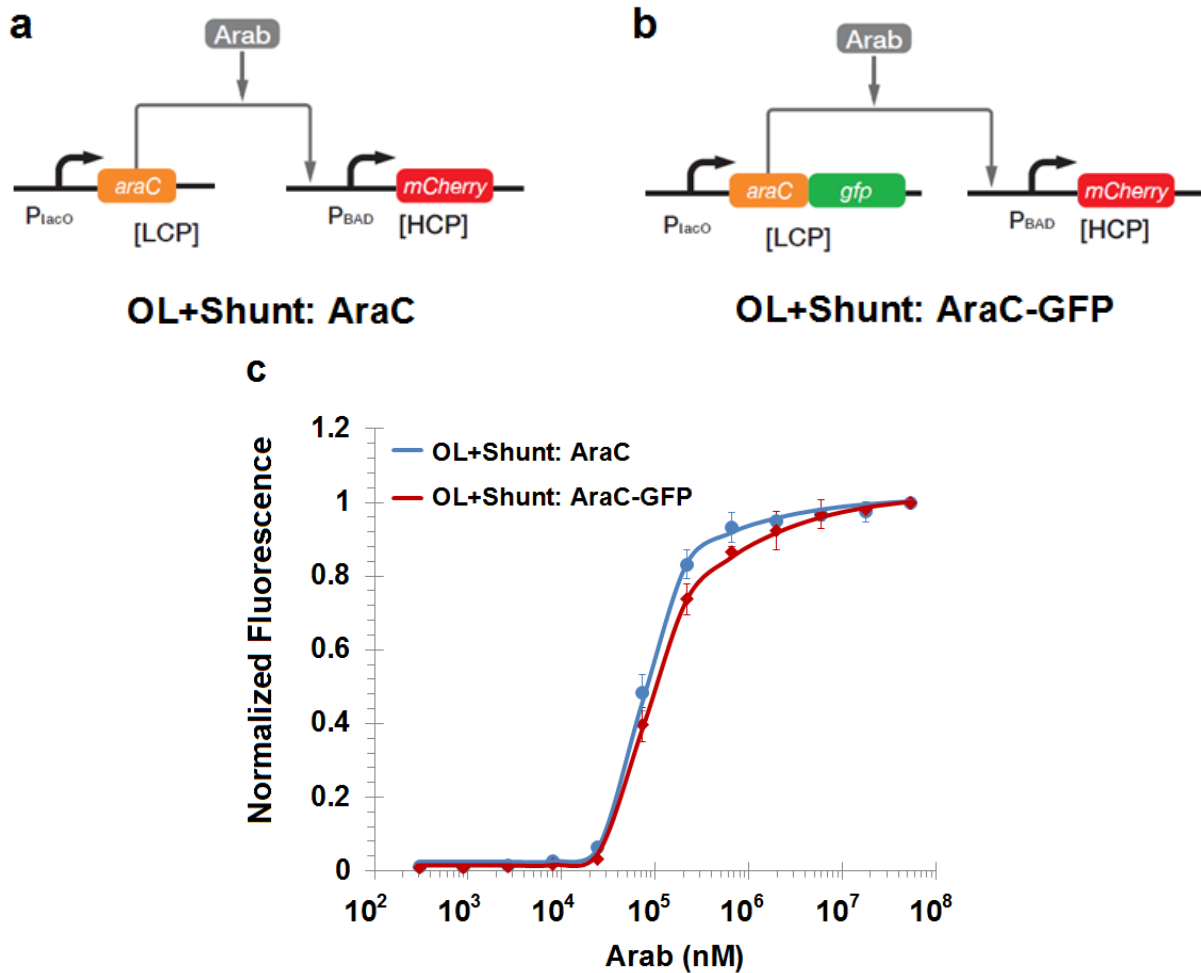


**Supplementary Figure 15.** Transfer functions for the open-loop LuxR circuits in different topologies. (a) The OL: LuxR circuit (blue circles, schematic in Supplementary Figure 14a) and the OL+Shunt: LuxR circuit (red diamonds, schematic in Supplementary Figure 14c) are shown. (b) The OL: LuxR-GFP circuit (blue circles, schematic in Supplementary Figure 14b) and the

OL+Shunt: LuxR-GFP circuit (red diamonds, schematic in Supplementary Figure 14d) are shown. Model fits are shown as solid lines. (c) LuxR does not repress the  $P_{lux}$  promoter in the absence of AHL for the circuit shown in Supplementary Figure 14e. When LuxR is expressed at high levels from an inducible  $P_{lacO}$  promoter (IPTG = 10 mM), the GFP output from the  $P_{lux}$  promoter is higher than when LuxR is expressed at low levels (IPTG = 0 mM).

### 3.2 AraC-Based Open Loop Circuits

We constructed two open loop circuits with AraC. The first circuit is shown in Supplementary Figure 16a, where the transcription factor is on a LCP and its promoter is on a different high-copy plasmid (HCP). The second circuit is shown in Supplementary Figure 16b, where we fused AraC to GFP. The experimental results and modeling fits are shown in Supplementary Figure 16c. Model parameters are shown in Supplementary Table 2.

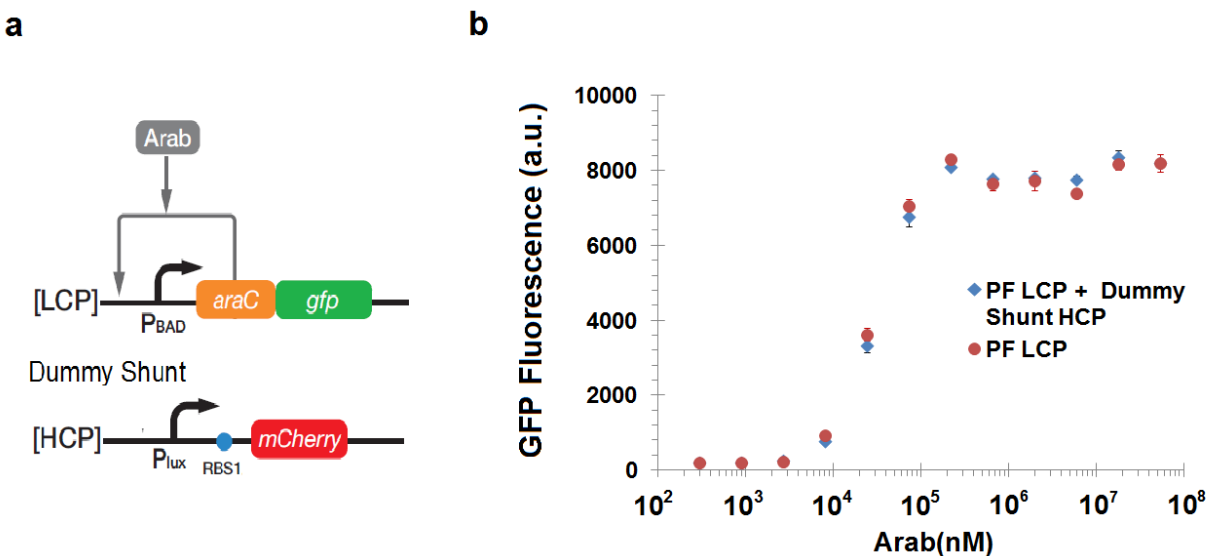


**Supplementary Figure 16.** Experimental data and schematics for AraC-based open-loop circuits with shunts. (a) The transcription factor AraC, under the control of the  $P_{lacO}$  promoter, is

expressed from a LCP and, in the presence of arabinose, activates transcription of mCherry from the  $P_{BAD}$  promoter on a HCP. (b) The transcription factor AraC-GFP, under the control of the  $P_{lacO}$  promoter, is expressed from a LCP and, in the presence of arabinose, activates transcription of mCherry from the  $P_{BAD}$  promoter on a HCP. (c) The mCherry output of the OL+Shunt: AraC circuit is shown in blue circles and the mCherry output of the OL+Shunt: AraC-GFP circuit is shown in red diamonds (This data appears in Figure 1d in the main text and is reproduced here for clarity). Model results are shown in solid lines.

### 3.3 Dummy Shunt Circuit

To test the specific effect of the shunt on linearization, we constructed a new circuit (Supplementary Figure 17a) which includes a “dummy” shunt for the AraC-GFP transcription factor that was based on the  $P_{lux}$  promoter. We compared these results to AraC-GFP positive feedback without a shunt. The experimental data is shown in Supplementary Figure 17b and demonstrates that the dummy shunt has negligible effects on the transfer function.



**Supplementary Figure 17.** (a) Schematic of AraC-GFP positive feedback with a dummy shunt. (b) AraC-GFP positive feedback plus dummy shunt is shown in blue diamonds and AraC-GFP positive feedback alone is shown in red circles.

**Supplementary Table 1.** List of abbreviations used in this study

<b>Symbol</b>	<b>Description</b>
<i>AHL</i>	Free <i>N</i> -( $\beta$ -Ketocaproyl)-L-homoserine lactone 3OC <sub>6</sub> HSL concentration
<i>AHL<sub>T</sub></i>	Total AHL concentration
<i>Arab</i>	Free Arabinose concentration
<i>Arab<sub>T</sub></i>	Total Arab concentration
<i>IPTG</i>	Free Isopropyl- $\beta$ -D-1-thiogalactopyranoside concentration
<i>LuxR</i>	Free LuxR concentration
<i>LuxR<sub>C</sub></i>	AHL-LuxR complex concentration
<i>LuxR<sub>Cb</sub></i>	Bound-promoter AHL-LuxR complex concentration
<i>LuxR<sub>CT</sub></i>	Total AHL-LuxR complex concentration
<i>LuxR<sub>T</sub></i>	Total LuxR concentration
<i>AraC</i>	Free AraC concentration
<i>AraC<sub>C</sub></i>	Arab-AraC complex concentration
<i>AraC<sub>Cb</sub></i>	Bound-promoter Arab-AraC complex concentration
<i>AraC<sub>CT</sub></i>	Total Arab-AraC complex concentration
<i>AraC<sub>T</sub></i>	Total AraC concentration
<i>LacI</i>	Free LacI concentration
<i>LacI<sub>C</sub></i>	IPTG-LacI complex concentration
<i>LacI<sub>T</sub></i>	Total LacI concentration
<i>P<sub>lux</sub></i>	LuxR promoter
<i>P<sub>BAD</sub></i>	AraC promoter
<i>P<sub>lacO</sub></i>	LacI promoter
<i>T</i>	Free transcription factor concentration (LuxR, AraC, LacI)
<i>T<sub>b</sub></i>	Bound-promoter transcription factor concentration
<i>T<sub>T</sub></i>	Total transcription factor concentration (LuxR <sub>T</sub> , AraC <sub>T</sub> , LacI <sub>T</sub> )

$I_n$	Free ligand concentration (AHL, Arab, IPTG)
$I_{nT}$	Total ligand concentration (AHL <sub>T</sub> , Arab <sub>T</sub> )
$E$	Free protein-degrading enzyme concentration
$E_T$	Total protein-degrading enzyme concentration
$O_T$	Number of promoter binding sites
$P$	Probability of a free transcription factor or inducer-transcription-factor complex binding to the promoter
$N$	Plasmid copy number
$V$	Cell volume
$D$	3D diffusion coefficient
$\tau_{slide}$	Sliding time of the transcription factor
$\tau_{jump}$	Jumping time of the transcription factor
$K_m$	Dissociation constant for inducer-transcription factor binding
$h_1$	Hill coefficient for inducer-transcription factor binding
$K_n$	Parameter for cooperative inducer-transcription factor binding
$h_2$	Parameter for cooperative inducer-transcription factor binding
$K_d$	Dissociation constant between inducer-transcription-factor complexes and promoter
$K_{df}$	Dissociation constant between free transcription factors and promoter
$G$	Total production rate
$g$	Production rate for induced promoter
<i>Basal</i>	Basal level of promoter activity
$\gamma$	Dilution rate due to cell division
$\mu$	Protein degradation rate due to protein-degrading enzyme
$\mu_{eff}$	Effective protein degradation rate
$K_b$	Michaelis-Menten constant for the protein-degrading enzyme
$\Theta$	Protection parameter

**Supplementary Table 2.** Parameter values for biochemical circuit models.

Parameters	$P_{lux}$ Promoter	$P_{BAD}$ Promoter	$P_{lacO}$ Promoter
$K_m$	125nM <sup>a</sup>	$90 \times 10^3$ nM <sup>a</sup>	1.4mM <sup>a</sup>
$h_1$	1.4	3	1.4-1.65 <sup>c</sup>
$K_n$	400	1000	
$h_2$	1.05	2.5	
$K_d$	800	140	$1.76 \times 10^4$
$K_{df}$		$140 \times 9^b$	7
$g/\mu_0$	800	55	55
$g_0/\mu_0$	5	0.05	
$O_{T1}$	$5 \times 1$	$5 \times 10$	$5 \times 10$
$N$	63 for HCP 18 for MCP	63 for HCP 30 for MCP	
$O_{T2}$	$O_{T1} \times N$	$O_{T1} \times N$	
$\rho$	1	1	
$\beta$	25	100	
$K_b$	30	$1.5 \times 10^4$	
$\Theta$	1	0.2	
$\gamma/\mu_0$	0.2	0.2	
<i>ni</i>			1

<sup>a</sup> Parameter was set according to the literature (Ref. 8).

<sup>b</sup>  $K_d/K_{df}$  was set according to the literature (Ref. 16).

<sup>c</sup> For the wide-dynamic-range negative-slope circuit we obtained 1.65 for this parameter. In the negative-feedback circuit where mCherry is fused to the C-terminus of LacI we obtained 1.4.

The parameters:  $h_1$ ,  $h_2$ ,  $N$ ,  $\rho$ ,  $\beta$ ,  $\Theta$  and  $\gamma/\mu_0$  are unitless.

The parameters:  $K_n$ ,  $K_d$ ,  $K_{df}$ ,  $g/\mu_0$ ,  $g_0/\mu_0$ ,  $O_{T1}$ ,  $O_{T2}$ , and  $K_b$  have the units of the measured signal.

## 4 Simple Mathematical Models for Synthetic Analog Genetic Circuits

In this section we fit our experimental results to simple mathematical approximations which enable straightforward analog circuit design. These approximations are not based on physical parameters as discussed in our previous sections. However, they are useful in allowing quick design and insights into circuit behavior.

### 4.1 Simple Mathematical Model for the WDR Positive-Logarithm Circuit

General genetic circuits including our wide-dynamic-range PF-shunt circuit can be empirically approximated by a simple Hill function<sup>8</sup>:

$$f(I_n) = a \cdot \frac{\left(\frac{I_n}{b}\right)^n}{1 + \left(\frac{I_n}{b}\right)^n} + d, \quad (53)$$

where  $I_n$  is the inducer concentration (AHL, Arab),  $n$  is the Hill coefficient,  $a$  is an amplification parameter,  $d$  is the basal level of expression and  $f(\cdot)$  represents the output. The Hill function  $x^n/(1+x^n)$  can be re-written as:

$$\frac{x^n}{1+x^n} = \frac{(x^n+1)-1}{1+x^n} = 1 - (1+x^n)^{-1} = 1 - e^{-\ln(1+x^n)} \quad (54)$$

For small values of  $\ln(1+x^n)$ , we get:

$$\frac{x^n}{1+x^n} \approx 1 - (1 - \ln(1+x^n)) = \ln(1+x^n) \quad (55)$$

Then, we approximate our PF-shunt output as:

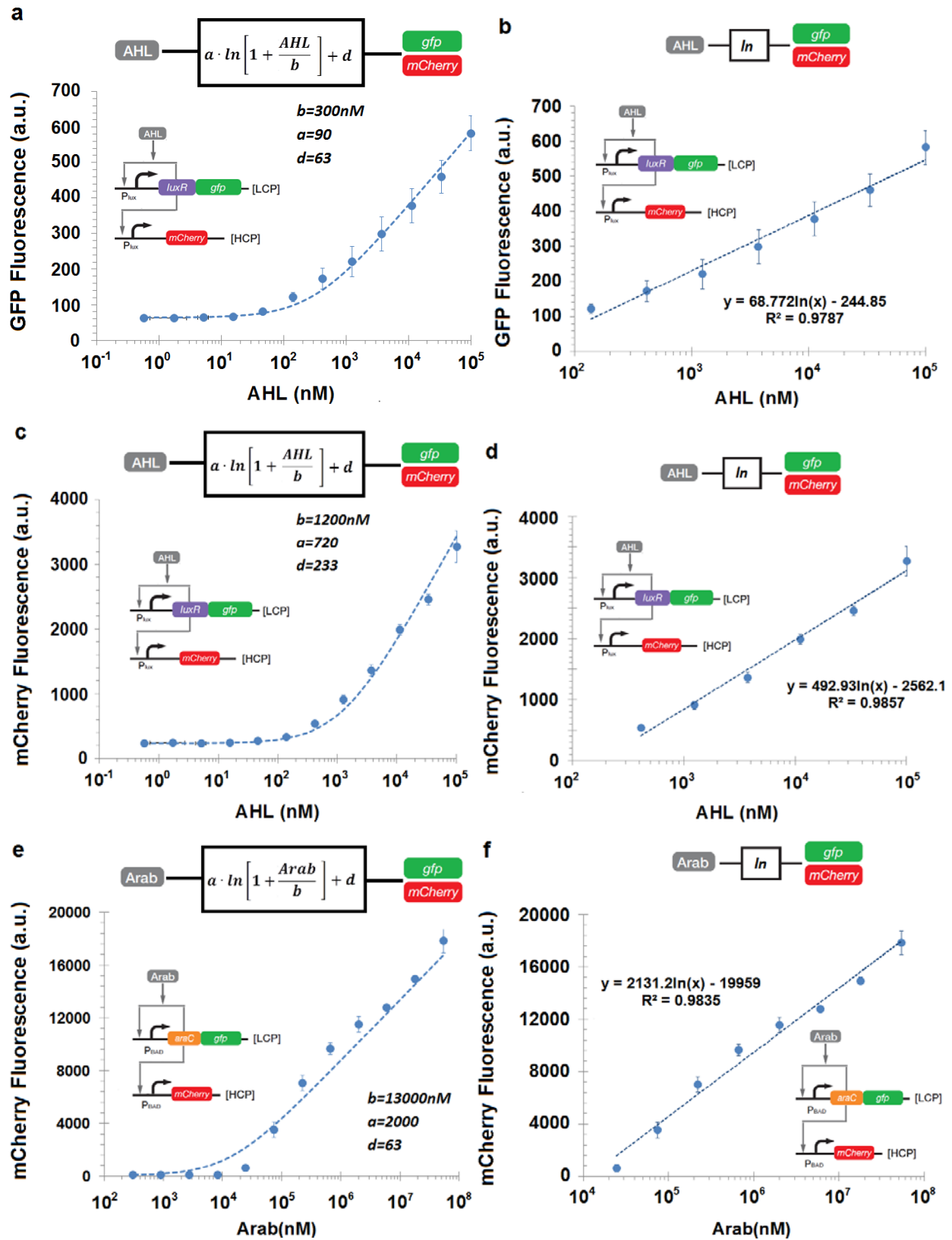
$$f(I_n) = a \cdot \ln\left(1 + \left(\frac{I_n}{b}\right)^n\right) + d \quad (56)$$

For  $(I_n/b)^n > 1$ , we can approximate Eq. 56 as:

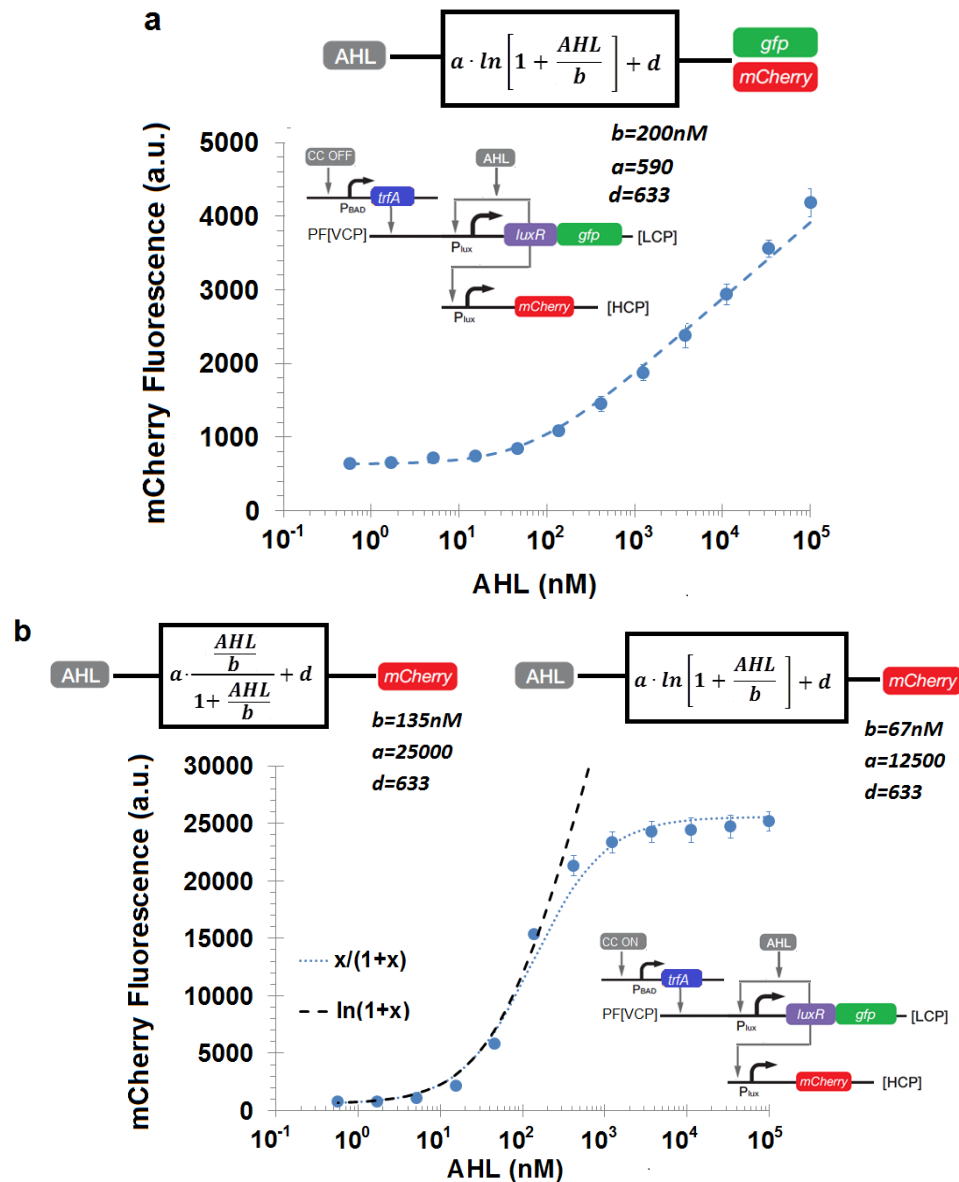
$$f(I_n) = a \cdot n \cdot \ln\left(\frac{I_n}{b}\right) + d \quad (57)$$

In practice,  $a$  and  $n$  are represented by one parameter  $a' = an$  and  $n$  is set to 1 in all fits.

Because log-domain electronic circuits obey the exponential laws of Boltzmann thermodynamics like biochemical circuits do, highly accurate biochemical functions and Hill-function approximations thereof can be implemented by analog circuits that only use a single transistor or a handful of transistors<sup>1,20</sup>. Therefore, the  $\ln(1+x)$  function is a good approximation for describing the input-output behavior of electronic circuits as well.



**Supplementary Figure 18.** Logarithmic approximations to the PF-shunt circuit. (a) GFP signal for LuxR is fit to  $\ln(1+x)$ , (b) GFP signal for LuxR is fit to  $\ln(x)$ , (c) mCherry signal for LuxR is fit to  $\ln(1+x)$ , (d) mCherry signal for LuxR is fit to  $\ln(x)$ , (e) mCherry Signal for AraC is fit to  $\ln(1+x)$ , (f) mCherry Signal for the AraC is fit to  $\ln(x)$ . The data shown in this figure are also found in Figure 1 and Figure 2 of the main text and are reproduced here for clarity.



**Supplementary Figure 19.** (a) The mCherry signal is fit to  $\ln(1+x)$  when the copy-control, CC, is OFF (PF is LCP and Shunt is HCP); this model function provides a good fit over the entire input range. (b) Dotted line: the mCherry signal is fit to the Hill function  $x/(1+x)$  when CC is ON (PF is HCP and the Shunt is HCP); this model function provides a good fit over

the entire input range. Dashed line: the mCherry signal is fit to  $\ln(I+x)$  when CC is ON (PF is HCP and the Shunt is HCP); this model function provides a good fit over only a limited range of low AHL concentrations. This data appears in Figure 2e in the main text and is reproduced here for clarity.

#### 4.2 Simple Mathematical Model for the WDR Negative-Logarithm Circuit

The wide-dynamic-range negative-slope circuit includes two stages:

(1) A wide-dynamic-range positive-slope circuit fit to  $a_1 \cdot \ln\left(1 + \frac{AHL}{b_1}\right) + d$  (Eq. 56) as shown in Supplementary Figure 20a.

(2) The output of  $P_{lacO}$  promoter can be approximated by a Hill function:

$$f(LacI_T) = a_2 \cdot \frac{1}{1 + \frac{LacI_T}{b_2}} \quad (58)$$

According to the approximation of Eq. 55,  $P_{lacO}$  promoter activity is then well-fit by:

$$\frac{1}{1+x} = e^{-\ln(1+x)} \cong 1 - \ln(1+x) \quad (59.1)$$

$$f(lacI_T) = d_2 - a_2 \cdot \ln\left(1 + \frac{LacI_T}{b_2}\right) \quad (59.2)$$

The fitting results for  $P_{lacO}$  promoter activity are shown in Supplementary Figure 20b. Substituting Eq. 56 in Eq. 59 we find that the output of our two-stage cascade can be fit by:

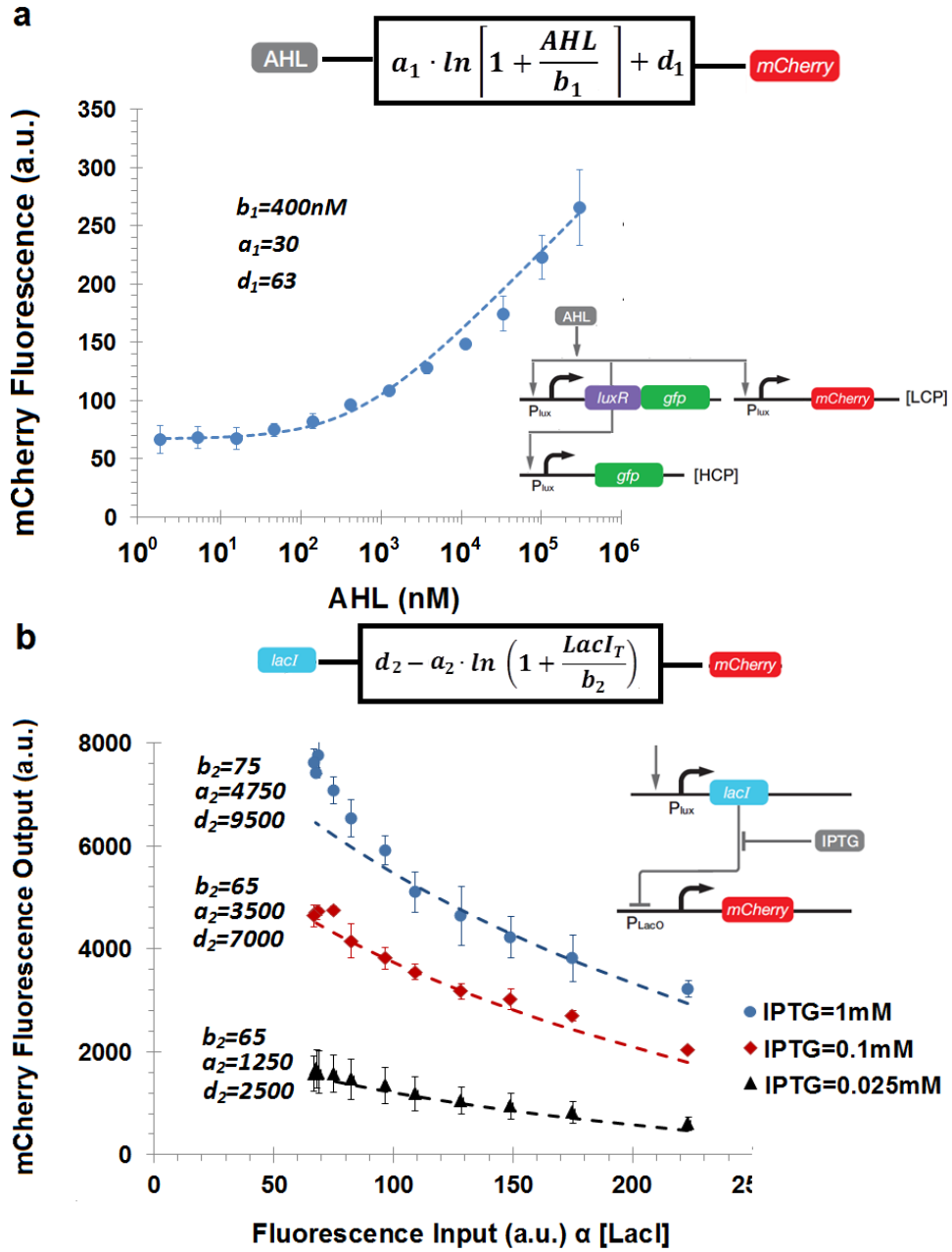
$$f(AHL) = d_2 - a_2 \cdot \ln\left(1 + \frac{a_1}{b_2} \cdot \ln\left(1 + \frac{AHL}{b_1}\right) + \frac{d_1}{b_2}\right) \quad (60)$$

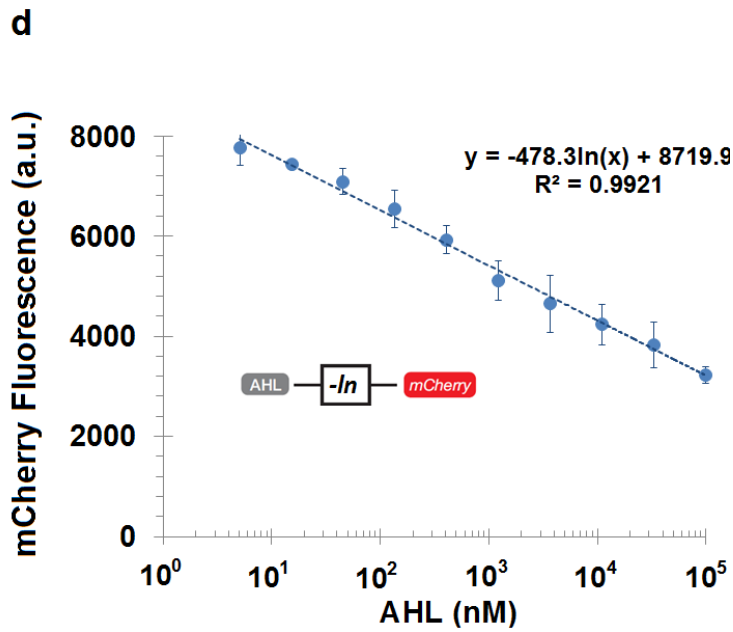
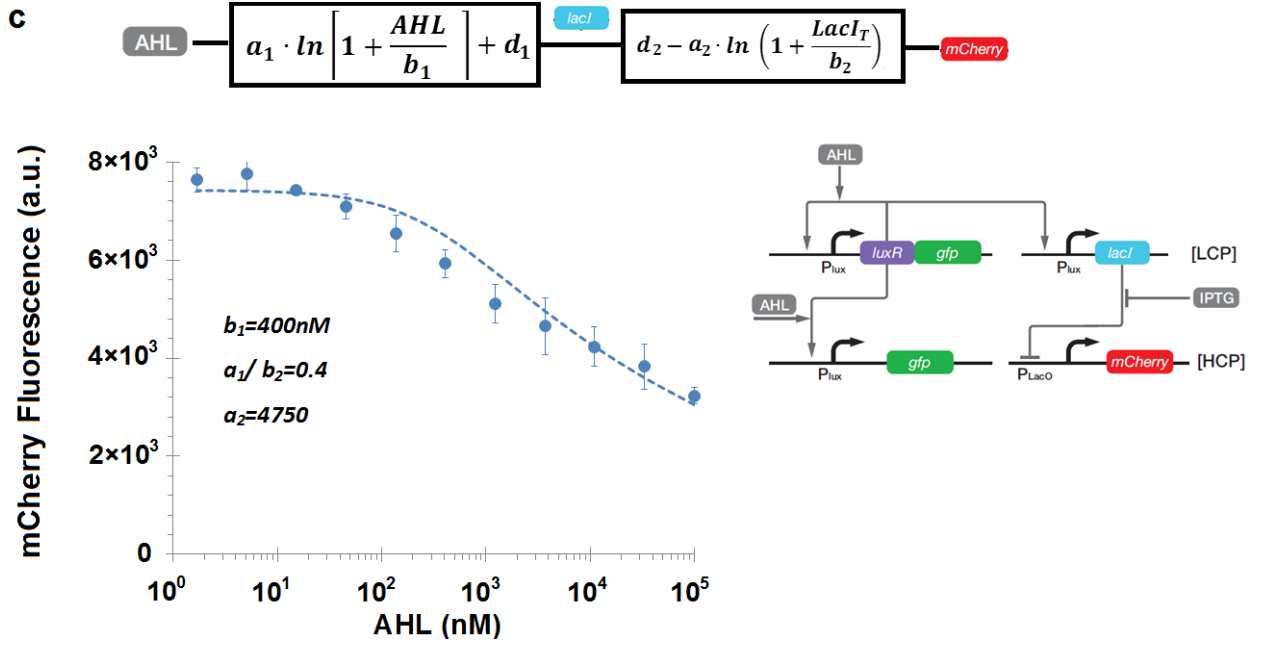
The fitting results are shown in Supplementary Figure 20c. Since we expressed LacI in a LCP and IPTG is high (the dissociation constant of the IPTG-LacI complex binding to DNA is large), then the ratio  $a_1/b_2 \ll 1$ . Using the approximation  $\ln(1+z) \approx z$  (for  $z \ll 1$ ), we can approximate Eq. 60 by an equation of the form:

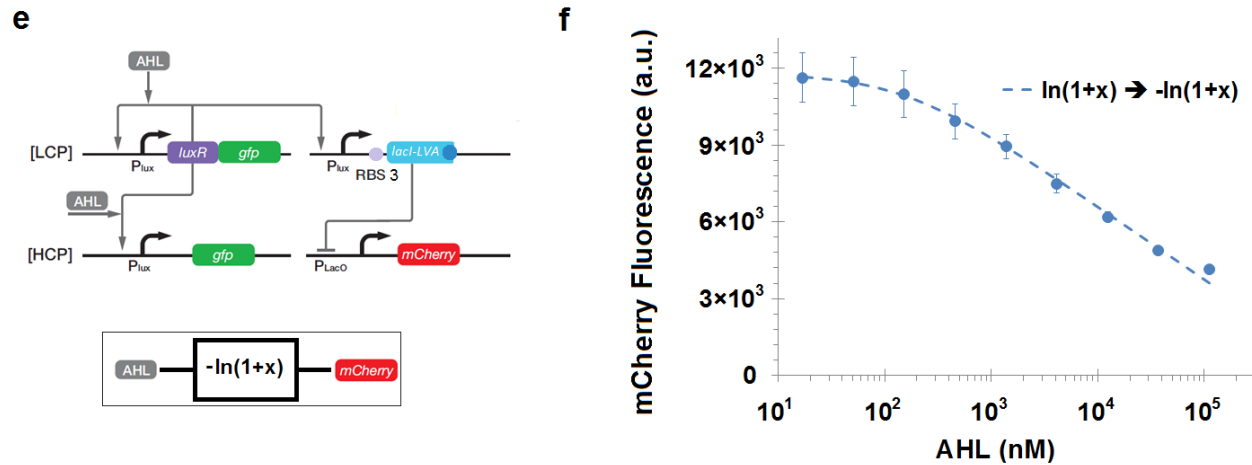
$$f(AHL) = d_2 - c \cdot \ln\left(1 + \frac{AHL}{b_1}\right) \quad (61)$$

For  $1 \ll AHL/b_1$ , we get a negative-slope logarithm function:

$$f(AHL) = d_2 - c \cdot \ln\left(\frac{AHL}{b_1}\right) \quad (62)$$







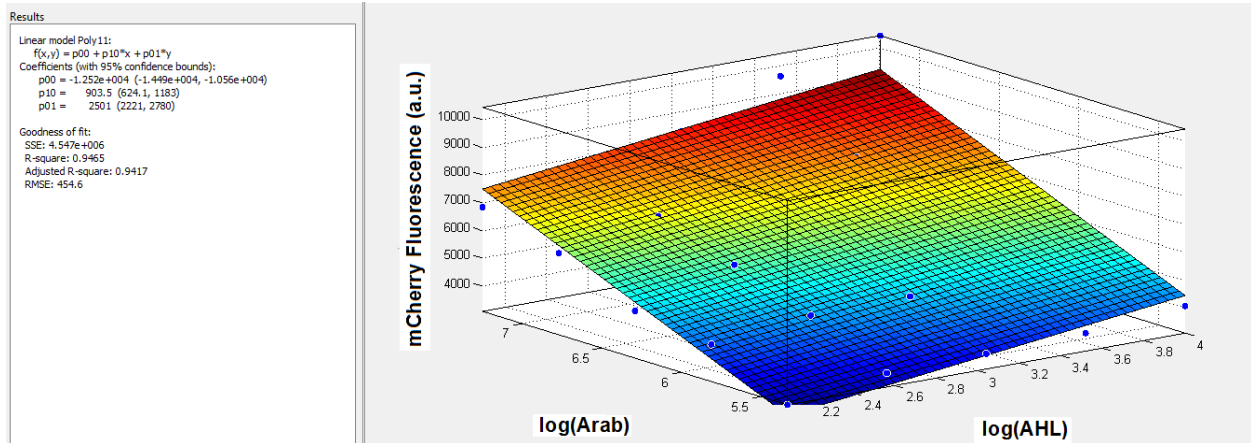
**Supplementary Figure 20.** (a) The mCherry output signal is fit to  $\ln(1+x)$ . This data appears in Supplementary Figure 31b and is reproduced here for clarity. (b) The  $P_{lacO}$  output signal is fit by  $-\ln(1+x)$ . This data appears in Supplementary Figure 31d and is reproduced here for clarity. (c) The mCherry signal, which represents the output of a cascade of two stages is fit by Eq. 60. This data appears in Figure 3h in the main text and is reproduced here for clarity. (d) The mCherry signal is fit to a log-linear negative slope. (e) A wide-dynamic-range negative-logarithm circuit that does not require an inducer (IPTG) for tuning LacI expression. (f) Experimental data showing the AHL-to-mCherry transfer function for the circuit of (e). The dashed blue line is a fit to the  $-\ln(1+x)$  function.

External tuning of our multi-stage analog circuits via inducers is not essential in our framework, which is an advantage for the scalability of our circuits in situations where an inducer may not be available. For example, Supplementary Figures 20e-f show that the WDR negative-logarithm function can be achieved without the need for external tuning of LacI repression with the inducer IPTG: We tagged LacI with a C-terminal *ssrA*-based degradation tag (TSAANDENYALVA<sup>23</sup>) and expressed it with a weaker RBS (RBS3, Supplementary Table 4) (Supplementary Figure 20e) to tune expression rather than using an inducer, and obtained good experimental results (Supplementary Figure 20f).

#### 4.3 Simple Mathematical Model for the Log-Linear Adder Circuit

The log-linear adder circuit can be fit by the simple expression, indicating a sum of log-transformed inputs:

$$f(AHL, Arab) = a_1 \ln\left(\frac{AHL}{b_1}\right) + a_2 \ln\left(\frac{Arab}{b_2}\right) \quad (63)$$



**Supplementary Figure 21.** Matlab surface fits to the adder circuit data. This data appears in Figure 3b in the main text and is reproduced here for clarity.

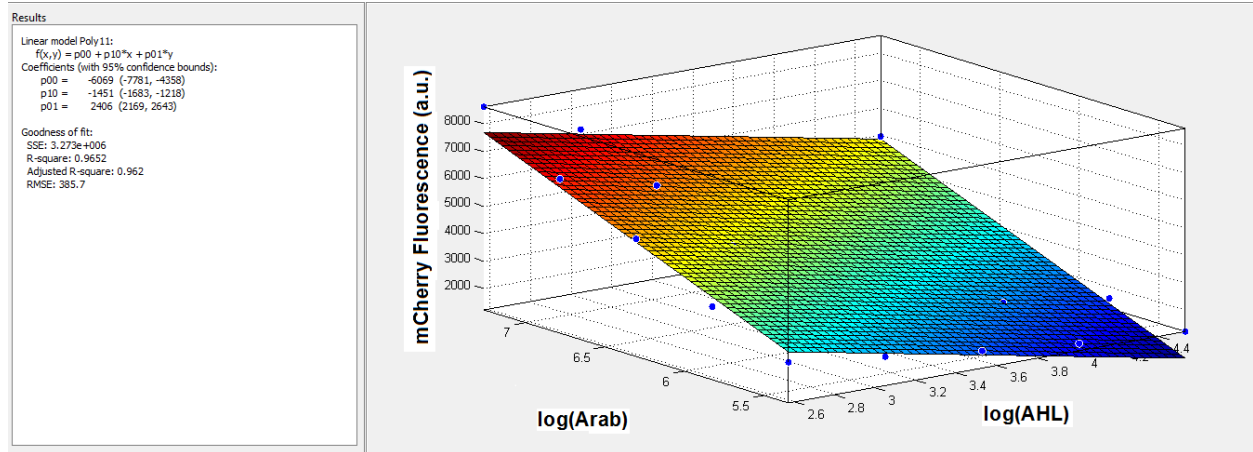
#### 4.4 Simple Mathematical Model for the Ratiometer Circuit

The ratiometer can be fit by the simple mathematical expression, indicating a difference between log-transformed inputs:

$$f(AHL, Arab) = Const - a_1 \ln\left(\frac{AHL}{b_1}\right) + a_2 \ln\left(\frac{Arab}{b_2}\right) \quad (64.1)$$

In the case that  $a_1=a_2=a$ :

$$f(AHL, Arab) = Const + a \ln\left(\frac{Arab}{AHL} \cdot \frac{b_1}{b_2}\right) \quad (64.2)$$



**Supplementary Figure 22.** Matlab surface fits to the ratiometer circuit data. This data appears in Figure 3d in the main text and is reproduced here for clarity.

#### 4.5 Simple Mathematical Model for the Power Law Circuit

In Supplementary Figure 13, we presented a power-law genetic circuit and derived a detailed biochemical model that captures its behavior. Here, we derive a simple mathematical model of its operation.

From Supplementary Figure 13a,  $AraC_T = \frac{G_1}{1 + \frac{LacI_T}{K_{df}} \left( \frac{1}{1 + \left(\frac{IPTG}{K_m}\right)^{h_1}} \right)}$ , from the LCP. Here,  $G_1$  represents

maximal production from the  $P_{lacO}$  promoter. Similarly, from the HCP,  $LacI_T = \frac{G_2}{1 + \frac{K_d}{AraC_T}}$  where

$G_2$  represents maximal production from the  $P_{BAD}$  promoter. These two equations need to be consistent as per the negative-feedback loop of Supplementary Figure 13a. Hence, if we substitute the  $AraC_T$  term from the first equation into the second equation and solve for the  $LacI_T$  term, we get:

$$LacI_T = \frac{-K_{df} \left( 1 + \left( \frac{IPTG}{K_m} \right)^{h_1} \right) \left( 1 + \frac{G_1}{K_d} \right) + \sqrt{\left( K_{df} \left( 1 + \left( \frac{IPTG}{K_m} \right)^{h_1} \right) \left( 1 + \frac{G_1}{K_d} \right) \right)^2 + 4 \frac{G_2 G_1 K_{df}}{K_d} \left( 1 + \left( \frac{IPTG}{K_m} \right)^{h_1} \right)}}{2} \quad (65)$$

According to Eq. 46.1, for the  $LacI$  production from the HCP we get:

$$K_d \rightarrow K_d \cdot N_{HCP} \cdot \left( 1 + \frac{\beta}{(N_{HCP} + N_{LCP})^{2/3}} \right) \quad (66.1)$$

$$G_2 \rightarrow N_{HCP} G_2 \quad (66.2)$$

Similarly, from Eq. 46.1, for the  $AraC$  production from the LCP we get:

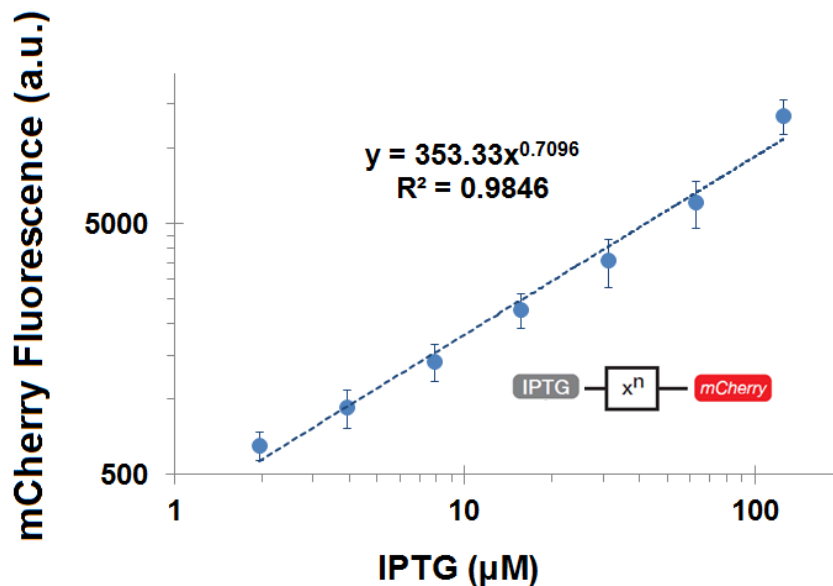
$$K_{df} \rightarrow K_{df} \left( 1 + \frac{\beta}{(N_{HCP} + N_{LCP})^{2/3}} \right) \quad (67)$$

For large  $N_{HCP}$  we get:

$$LacI_T = \frac{\sqrt[4]{\frac{G_2 G_1 K_{df}}{K_d} \left( 1 + \left( \frac{IPTG}{K_m} \right)^{h_1} \right)}}{2} \quad (68)$$

In the range where  $\left( \frac{IPTG}{K_m} \right)^{h_1} \gg 1 \rightarrow LacI_T \propto \left( \frac{IPTG}{K_m} \right)^{h_1/2}$

Thus, we have a power-law circuit as confirmed by the measurements of Supplementary Figure 13 and as shown by Supplementary Figure 23.



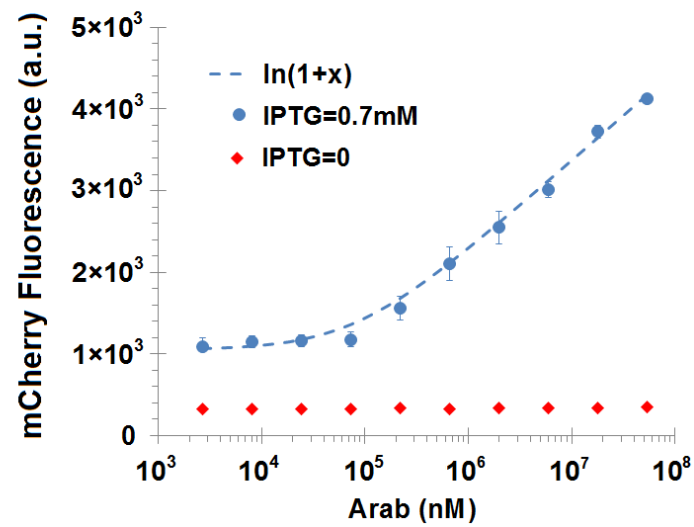
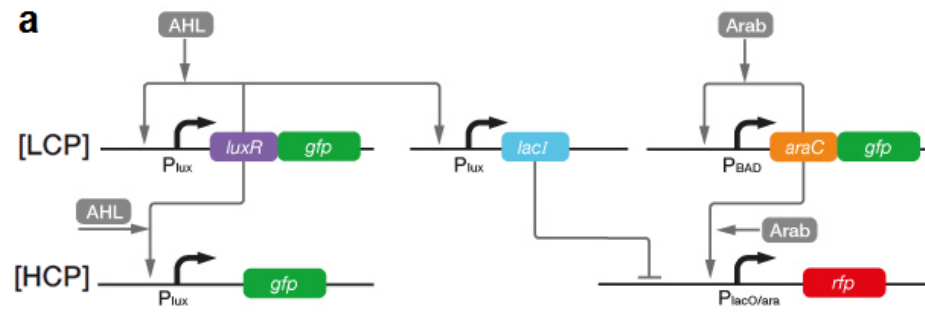
**Supplementary Figure 23.** The IPTG-to-mCherry transfer function is a mathematical power law function. This data appears in Figure 3f in the main text and is reproduced here for clarity.

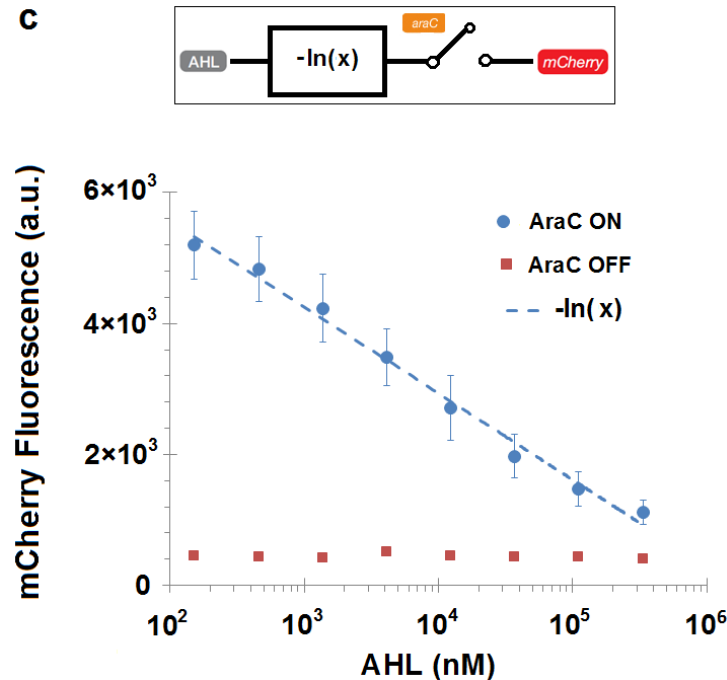
## 5 Mixed Analog-Digital Circuits

Analog functions can be integrated with digital control as a powerful mixed-signal strategy for tuning dynamic circuit behavior. To demonstrate such functionality, we built a positive-logarithm circuit that could be toggled by the presence or absence of an input inducer (Supplementary Figure 24a). This toggling was achieved by using a hybrid promoter ( $P_{lacO/ara}$ ), repressed by LacI and activated by AraC, as the output of the AraC-based positive-logarithm circuit. In the absence of IPTG, the output of the circuit was OFF with respect to the arabinose input; whereas in the presence of IPTG, the output of the circuit was a wide-dynamic-range positive logarithm on the arabinose input (Supplementary Figure 24b). We found that the

arabinose-to-GFP transfer function was well-fit by a simple mathematical function of the form  $\ln(1 + x)$ , in the presence of IPTG (when the switch is “ON”).

The same circuit can implement a negative-logarithm circuit with AHL as its input that can be digitally toggled by the presence or absence of arabinose. As shown in Supplementary Figure 24c, this circuit implements a negative logarithm in the presence of arabinose whereas it is shut OFF in the absence of arabinose. This circuit requires no addition of external IPTG to function, similar to the circuit in Supplementary Figure 20e. Thus, it demonstrates that complex mixed-signal functions can be implemented and scaled without the need for additional external inducer inputs.

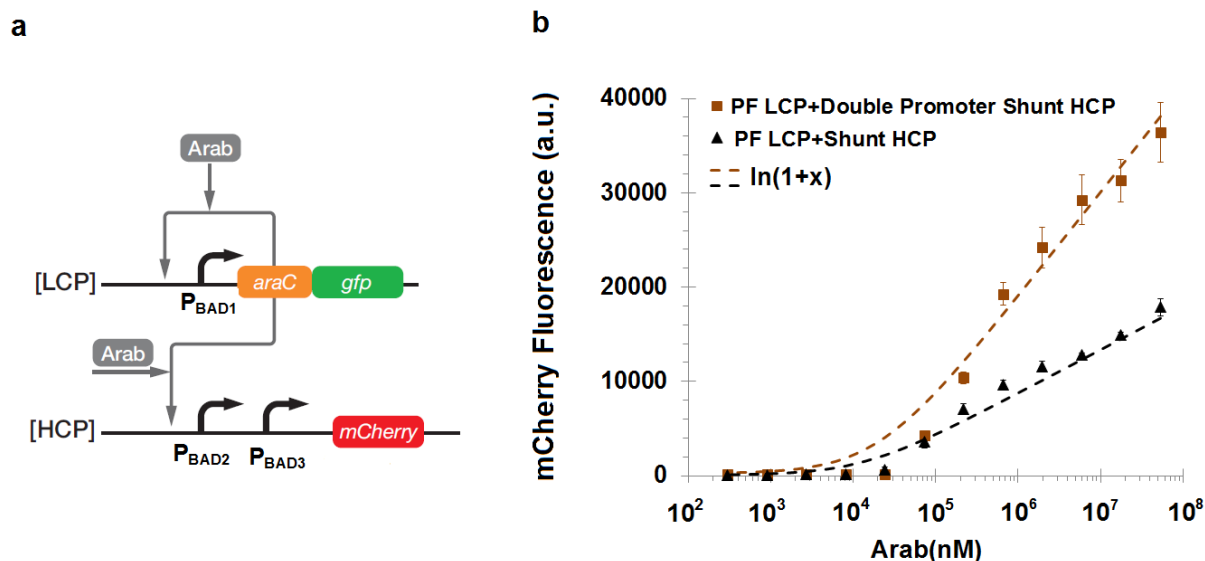




**Supplementary Figure 24.** Mixed-signal control and log-linear functions constructed with synthetic gene circuits. (a) Hybrid promoters, such as  $P_{lacO/ara}$ , enable digital toggling of analog input-output transfer functions, such as the WDR logarithm. (b) When IPTG is low (0 mM), the arabinose-to-mCherry transfer function is correspondingly OFF. When IPTG is high (0.7 mM), the transfer function implements a positive-logarithm transformation on arabinose as an input that spans almost three orders of magnitude. AHL was held constant at 5  $\mu$ M. The dashed blue line is the fit of the  $\ln(1+x)$  function. (c) When AraC is OFF (arabinose = 0 mM), the AHL-to-mCherry transfer function is correspondingly OFF. When AraC is ON (arabinose = 66 mM), the transfer function implements a negative-logarithm transformation on AHL as an input that spans almost three orders of magnitude. The dashed blue line is the fit of the  $-\ln(x)$  function.

## 6 A Double-Promoter PF-Shunt Circuit

We constructed a new wide-dynamic-range PF-shunt circuit with two identical promoters on the shunt HCP. The circuit is shown in Supplementary Figure 25a. The PF LCP has a single  $P_{BAD}$  promoter and the shunt HCP has two identical  $P_{BAD}$  promoters. The output of the PF LCP with this double-promoter shunt circuit is a wide-dynamic-range positive logarithm with higher gain than the PF LCP with a single promoter shunt HCP circuit (Supplementary Figure 25b). These results indicate that the input-to-output gain of our circuits can be tuned. We found that the arabinose-to-mCherry transfer function is well fit by a simple mathematical function of the form  $\ln(1+x)$ .



**Supplementary Figure 25.** A wide-dynamic-range PF-shunt circuit with two tandem promoters on the HCP. (a) The circuit includes a single  $P_{BAD}$  promoter on the LCP and two  $P_{BAD}$  promoters on the shunt HCP. (b) Experimental measurements from the double-promoter PF-shunt circuit (brown squares) are contrasted with those from an equivalent PF-shunt circuit with a single promoter on the HCP (black triangles). The fits correspond to  $\ln(1+x)$  functions. The data for the PF LCP + Shunt HCP (black triangles) are reproduced from Figure 1d for comparison.

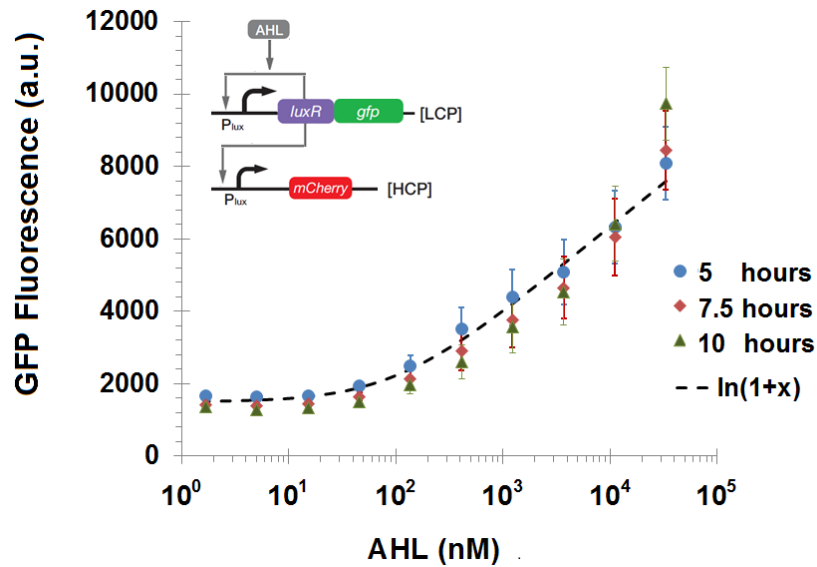
## 7 Dynamic Measurements of Analog Genetic Circuits

Time-course experiments were performed on our AHL wide-dynamic-range circuit positive-logarithm circuit (the circuit of Figure 2b). *E. coli* strains were picked from LB agar plates and grown overnight at 37°C and 300 rpm in 3 mL of LB medium with appropriate antibiotics and inducers (carbenicillin (50  $\mu\text{g/ml}$ ), kanamycin (30  $\mu\text{g/ml}$ ) and AHL 3OC6HSL). Overnight cultures were diluted 1:100 into 3 mL of LB medium with added antibiotics and were then incubated at 37°C and 300 rpm for 20 minutes. 200  $\mu\text{l}$  of culture was then moved into a 96-well plate, combined with inducers, and incubated in a VWR microplate shaker at 37°C and 700 rpm.

Once the diluted cultures grew to an OD600 of  $\sim 0.5$  ( $\sim 3$  hours), 20  $\mu\text{l}$  of culture was moved into a new 96-well plate containing 200  $\mu\text{l}$  of media, antibiotics, and inducers and then incubated in a VWR microplate shaker at 37°C and 700 rpm.

At OD600  $\sim 0.5$ , 50  $\mu\text{l}$  of culture was moved to a 96-well plate with 200  $\mu\text{l}$  of PBS and taken to a FACS machine for measurement. In addition, 20  $\mu\text{l}$  of culture was moved into a new 96-well plate containing 200  $\mu\text{l}$  of media, antibiotics, and inducers and then incubated in a VWR microplate shaker at 37°C and 700 rpm. This iterative dilution, growth, and measurement process was repeated over 10 hours.

The experimental results corresponding to different times are shown in Supplementary Figure 26 below. The GFP output of the PF-shunt circuit is a wide-dynamic-range positive logarithm and well-fit by a simple mathematical function of the form  $\ln(1+x)$  at 5 hours, 7.5 hours, and 10 hours.



**Supplementary Figure 26.** Time-course experiments (5 hours, 7.5 hours, and 10 hours) of the LuxR-based PF-shunt circuit. The dotted line corresponds to a  $\ln(1+x)$  function.

## 8 Sensitivity Analysis

Here, we explore the effects of our circuit motifs on sensitivity. If we change the input signal  $I_n$  to  $I_n + \Delta I_n$  and measure the response  $\Delta f$  in the output signal  $f$ , then the sensitivity is defined as<sup>24</sup>:

$$S = \frac{\Delta f / \langle f \rangle}{\Delta I_n / \langle I_n \rangle} \quad (69)$$

where  $\langle \rangle$  denotes the stationary values of  $I_n$  and  $f$ .

We calculate the sensitivity for input-output transfer curves that fit a log-linear function and for input-output transfer curves that fit a Hill function:

- (1) If the input-output transfer curve does not saturate and fits a log-linear function (Eq. 56); for example, in our PF-and-shunt circuits, then:

$$f = a \cdot \ln \left( 1 + \frac{I_n}{b} \right) + d$$

$$\Delta f = a \cdot \frac{\Delta I_n}{\left( 1 + \frac{\langle I_n \rangle}{b} \right) \cdot b} \quad (70.1)$$

$$\frac{\Delta f}{\langle f \rangle} = \frac{\frac{\Delta I_n \cdot \langle I_n \rangle}{\langle I_n \rangle \cdot b}}{\left(1 + \frac{\langle I_n \rangle}{b}\right) \cdot \left(\ln\left(1 + \frac{\langle I_n \rangle}{b}\right) + \frac{d}{a}\right)} \quad (70.2)$$

In the limit that  $\Delta \rightarrow 0$ , the sensitivity, defined in Equation (69), is given by:

$$S = \frac{\langle I_n \rangle}{b + \langle I_n \rangle} \cdot \frac{1}{\ln\left(1 + \frac{\langle I_n \rangle}{b}\right) + \frac{d}{a}} \quad (70.3)$$

(2) If the input-output transfer curve saturates and fits a Hill function (Eq. 53), for example, in circuits with strong positive feedback and in circuits with open-loop motifs, then:

$$f = a \cdot \frac{I_n^n}{I_n^n + b^n} + d$$

$$\Delta f = a \cdot n \frac{\langle I_n \rangle^{n-1}}{\langle I_n \rangle^n + b^n} \cdot \frac{b^n}{\langle I_n \rangle^n + b^n} \Delta I_n \quad (71.1)$$

$$\Delta f = n \frac{b^n}{\langle I_n \rangle^n + b^n} \cdot a \frac{\langle I_n \rangle^n}{\langle I_n \rangle^n + b^n} \cdot \frac{\Delta I_n}{\langle I_n \rangle} \quad (71.2)$$

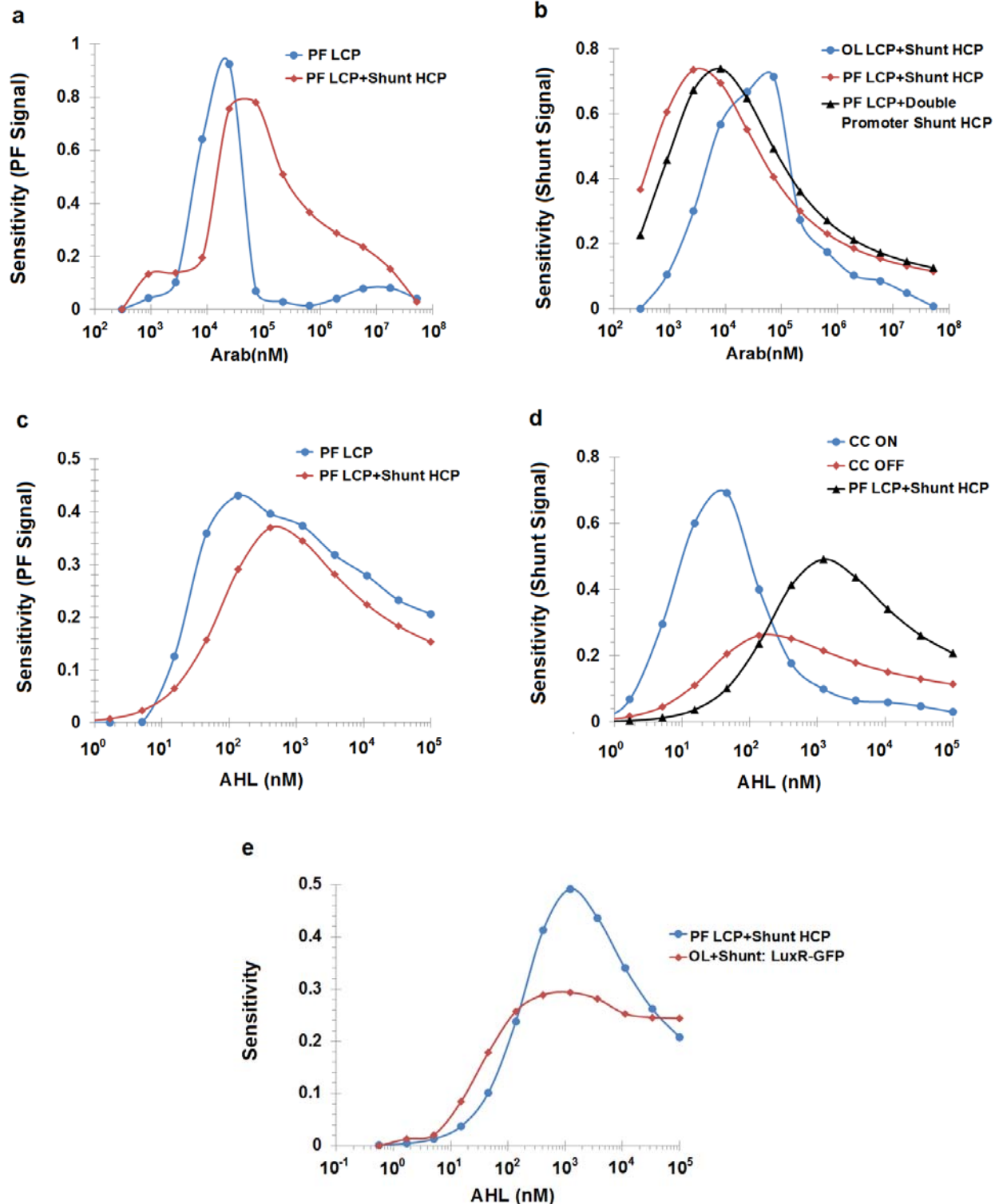
In the limit that  $\Delta \rightarrow 0$ , the sensitivity is given by:

$$S = n \left( \frac{\langle f \rangle - d}{\langle f \rangle} \right) \left( 1 - \frac{\langle f \rangle - d}{a} \right) \quad (71.3)$$

Supplementary Figure 27 shows the sensitivity for our analog PF-shunt circuit versus various controls. For the AraC-based circuits, our analog motifs (PF LCP with a HCP shunt; PF LCP with a double-promoter HCP shunt) showed peak sensitivities comparable to circuits with positive-feedback only (Supplementary Figure 27a) or with open-loop operation (Supplementary Figure 27b). Notably, across much of the input range, our analog motifs had higher sensitivities than the other motifs. For the LuxR-based circuits, our analog PF-shunt motif (PF LCP with a HCP shunt) had comparable or higher sensitivities than circuits with positive feedback only (Supplementary Figure 27c) or with open-loop operation (Supplementary Figure 27e). Thus, our analog motifs compare favorably in relation to other commonly used circuit motifs in synthetic biology.

In Figure 2d, we described a circuit motif that can be toggled between analog and digital behaviors by the addition of a CopyControl (CC) reagent to change the copy number of a variable-copy plasmid (VCP) containing a LuxR-based positive-feedback loop. As shown in Supplementary Figure 27d, the peak sensitivity of this circuit when operated with strong positive feedback that leads to digital behavior (CC ON) exceeds that of the circuit when operated with graded positive feedback that yields analog behavior (CC OFF) by a factor of  $\sim 2.6$ . However, the sensitivity of the circuit that exhibits digital behavior is significantly lower than the sensitivity of the circuit that exhibits analog behavior for over two orders of magnitude. The sensitivity of the digital circuit is also significantly lower than the sensitivity of an analog circuit with a PF LCP and a HCP shunt for over two orders of magnitude, and here the peak sensitivity is only lower by

a factor of 1.5. Thus, as may be expected from the nature of their input-output curves, digital and analog behavior provide complementary advantages: better sensitivity over a narrow dynamic range (digital), or better sensitivity over a wide dynamic range (analog). Both circuits are useful depending on the application, in both biological and electronic design.

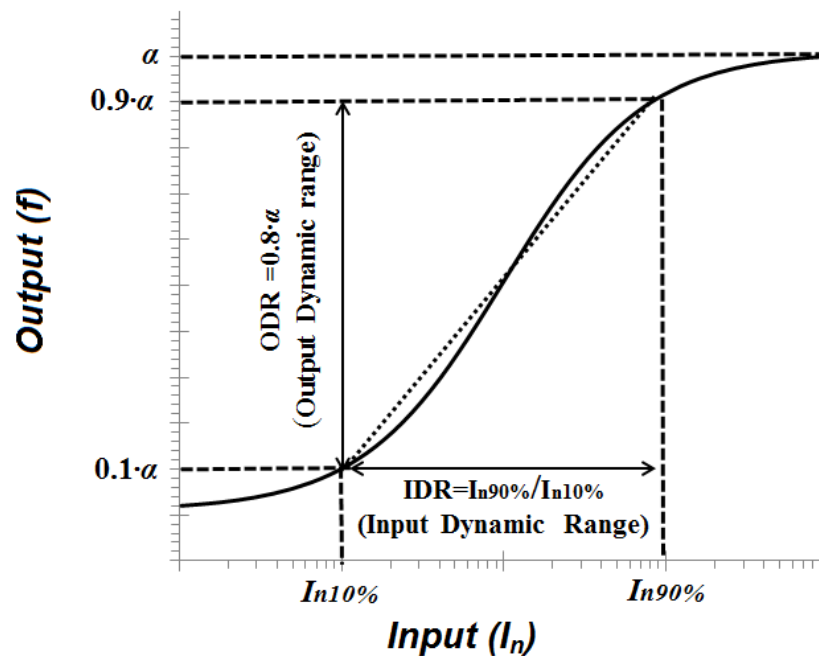


**Supplementary Figure 27.** Sensitivity values for various circuit motifs. (a) Sensitivities for the arabinose-to-GFP transfer functions for PF LCP versus PF LCP with a HCP shunt (Supplementary Figure 6). (b) Sensitivities for the arabinose-to-mCherry transfer functions for OL LCP with a HCP shunt (Figure 1d), PF LCP with a HCP shunt (Figure 1d), and PF LCP with

a double promoter HCP shunt (Supplementary Figure 25). (c) Sensitivities for the AHL-to-GFP transfer functions for PF LCP and PF with a HCP shunt (Figure 2b). (d) Sensitivities for the AHL-to-mCherry transfer functions for the PF VCP with a HCP shunt and CC OFF (Figure 2e), PF VCP with a HCP shunt and CC ON (Figure 2e), and PF LCP with a HCP shunt (Figure 2b). (e) Sensitivities for the AHL-to-mCherry transfer functions for LuxR-GFP expressed in an open-loop fashion with a HCP shunt (OL+Shunt: LuxR-GFP, Supplementary Figure 15b) and PF LCP with a HCP shunt (Figure 2b).

As described in Madar *et al.* and illustrated in Supplementary Figure 28a, we define the output dynamic range (ODR) as the difference between the 90% and 10% of the maximal output ( $\alpha$ ) and the input dynamic range (IDR) as the ratio of the input concentrations required for 90% and 10% of the maximal output<sup>25</sup>. This definition allows us to define the parameter  $a$  in Eq. 70.3, which is the slope of the relationship between the output  $f$  and  $\log(I_n)$ :

$$a = \frac{0.8 \cdot \alpha}{\log(IDR)} \quad (72)$$



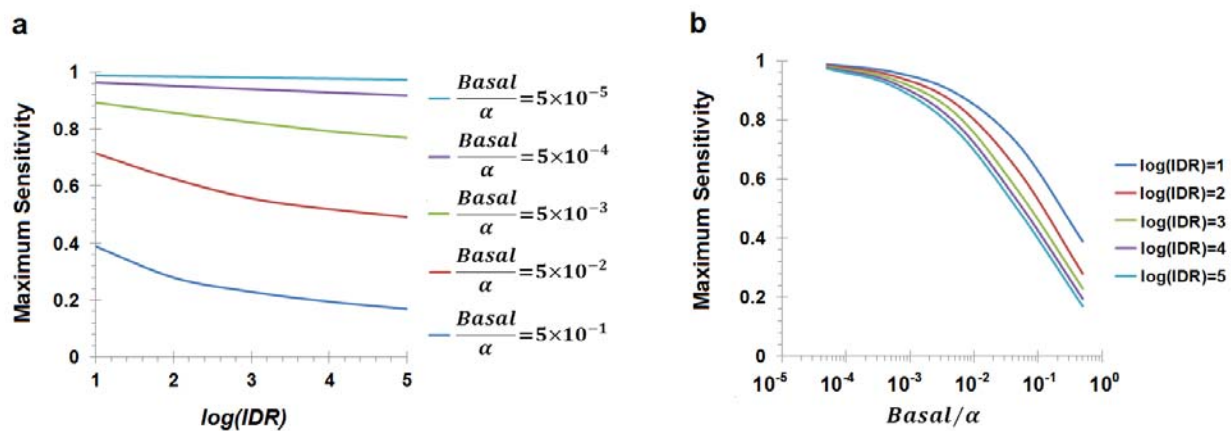
**Supplementary Figure 28.** Definition of Input Dynamic Range ( $IDR = I_{n90\%}/I_{n10\%}$ ) and Output Dynamic Range ( $ODR = 0.8 \cdot \alpha$ ).

Rewriting Eq. 70.3 by substituting in Eq. 72, the sensitivity of our analog circuits can be defined as:

$$S = \frac{\langle I_n \rangle / b}{1 + \langle I_n \rangle / b} \cdot \frac{1}{\ln(1 + \langle I_n \rangle / b) + 1.25 \cdot \frac{Basal}{\alpha} \cdot \log(IDR)}, \quad (73)$$

where  $d$  in Eq. 70.3, is defined as the basal level (*Basal*) of the transfer function.

Based on Eq. 73, the sensitivity is influenced by the IDR and the ratio between the basal level and the maximum output,  $\alpha$ . Supplementary Figure 29 shows the tradeoff between sensitivity and IDR for different values of the basal level and maximum output. As seen in Supplementary Figure 29a, for low basal-to-maximum-output ratios, the influence of the IDR on the sensitivity is very small, whereas for high basal-to-maximum output ratios, increasing the IDR decreases the sensitivity. This relationship may explain the enhanced sensitivities of the AraC-based circuits compared with the LuxR-based circuits in Supplementary Figure 27, as the AraC-based circuits were observed to have lower basal levels than LuxR-based circuits<sup>7</sup>. This analysis also indicates that reducing the basal level (e.g., via the use of riboregulators<sup>26</sup>) could enhance the sensitivity of future designs.



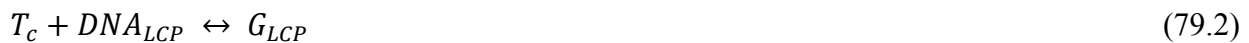
**Supplementary Figure 29.** Tradeoffs between sensitivity and IDR as a function of the basal level and the maximum output of analog transfer functions.

## 9 Minimal Models for Linearization via Positive Feedback

In this section, we describe minimal models for graded positive feedback without a shunt and for graded positive feedback with a shunt that are based only on biochemical reactions. These minimal models, while less accurate than our previously described complex biophysical models, nevertheless provide insight and intuition about the mechanism of linearization enabled by positive feedback. For example, they reveal that the use graded positive-feedback enables linearization and wide-dynamic-range operation on just a single plasmid if the  $K_d$  for biochemical binding of the transcription-factor complex to DNA is appropriate: The strength of the positive feedback, which depends on this  $K_d$ , must not be too strong to yield latching or reduced-dynamic-range analog operation; it must not be too weak to make the positive feedback ineffective at compensating for saturating effects. Indeed, our scheme for widening the log-linear dynamic range of operation via graded positive feedback is conceptually general and applies to both genetic and electronic circuits: expansive *sinh*-based linearization of compressive *tanh*-based functions in log-domain electronic circuits<sup>27</sup> is analogous to the use of expansive positive-

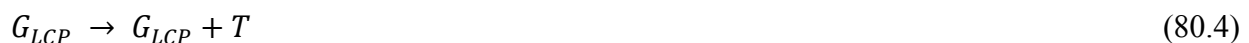
feedback linearization of compressive biochemical binding functions in log-domain genetic circuits, and such circuits show an optimum as well.

The set of the biochemical reactions which describe graded positive feedback without a shunt can be described by:

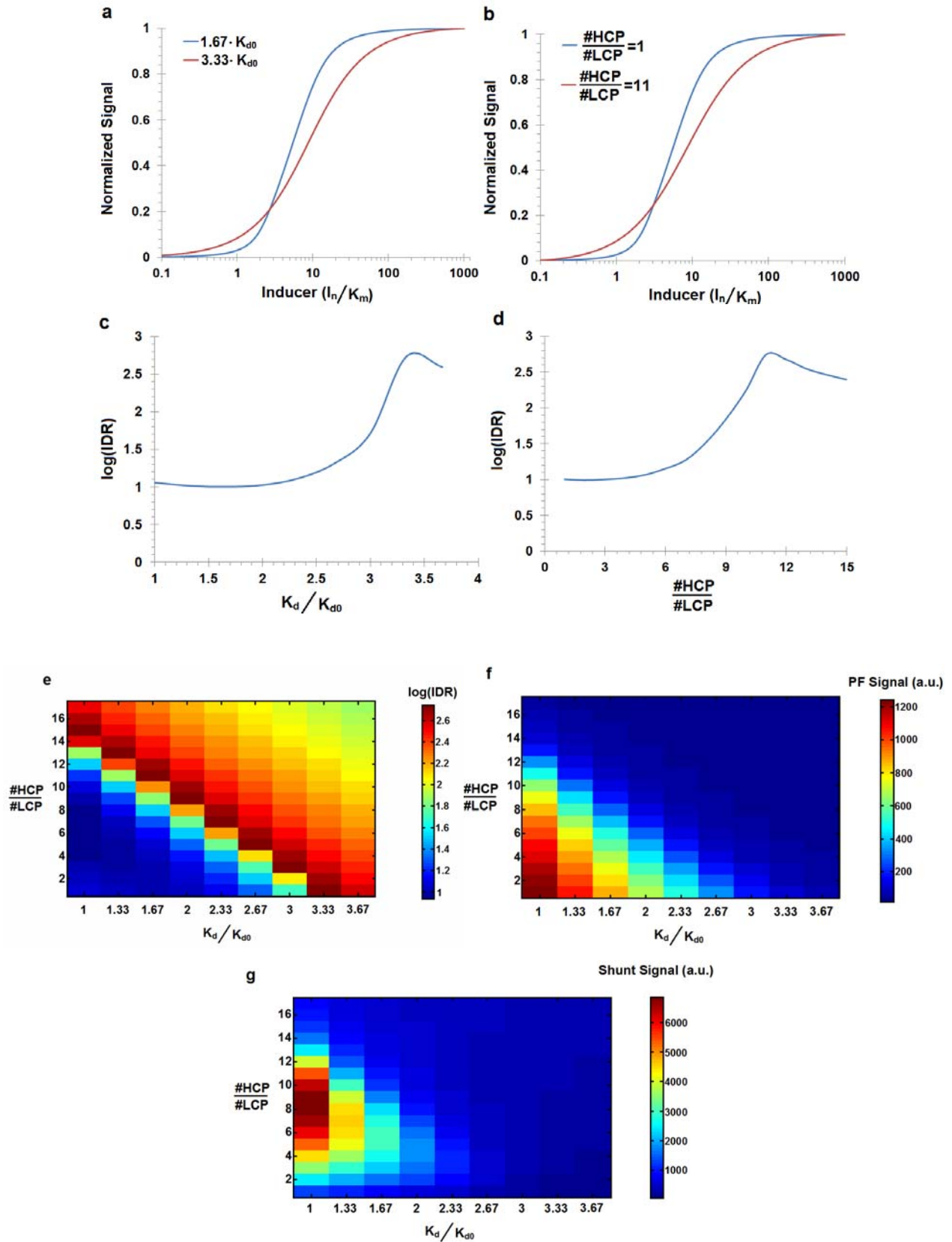


Eq. 79.1 describes the binding reaction of the inducer to the transcription factor. Eq. 79.2 describes the binding of the complex to the promoter. Eq. 79.3 describes the positive feedback loop and Eq. 79.4 describes the degradation of the transcription factor due to dilutive cell division. We define the input dynamic range (IDR) as the ratio of the input concentrations required for 90% and 10% of the maximal output<sup>25</sup> as shown in Supplementary Figure 28a.

A minimal set of biochemical equations for graded positive feedback involving a shunt are given by:



Eq. 80.1 describes the binding of the inducer to the transcription factor. Eq. 80.2 and Eq. 80.3 describe the binding of the complex to the promoter on the LCP and HCP. For simplicity in the minimal model, we assume that the forward and reverse rates of binding to the LCP and HCP are equal. Eq. 80.4 describes the positive-feedback loop and Eq. 80.5 describes the expression of the signal by the shunt. The final two reactions describe the degradation of the transcription factor and the signal, which we assume is identical due to dilutive cell division. The simulation results are shown in Supplementary Figure 30b. By decreasing the probability of binding of the transcription factor to the promoter, or by adding shunt binding sites, we can generate graded positive feedback with wide input dynamic range.



**Supplementary Figure 30.** Simulation results for the input dynamic range (IDR) of the minimal model of our positive-feedback circuit without and with a shunt plasmid. (a) Graded positive feedback without a shunt (Eqs. 79.1-79.4). (b) Graded positive feedback with a shunt (Eqs. 80.1-80.7). (c) The IDR obtained for Eqs. 79.1-79.4 as a function of  $K_d$  for the transcription-factor-promoter binding. (d) The IDR obtained for Eqs. 80.1-80.7 as a function of the ratio between the shunt HCP and the PF LCP. (e) A heat map shows the IDR as a function of  $K_d$  and the ratio between the copy numbers of the shunt HCP and the PF LCP. (f) A heat map of the PF signal. (g) A heat map of the shunt HCP signal. (Parameters:  $K_m=100$ ,  $K_{d0}=540$ ,  $A_{max}=1800$  e.g., the ratio between the maximum production rate in Eqs. 79.3, 80.4, and 80.5 and the degradation rate in Eqs. 79.4, 80.6, and 80.7,  $A_{Basal}=10$  e.g., the ratio between the basal production rate and the degradation rate).

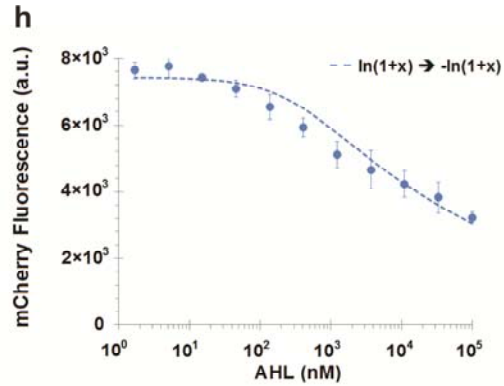
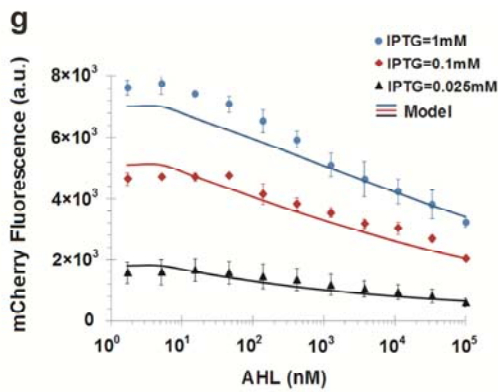
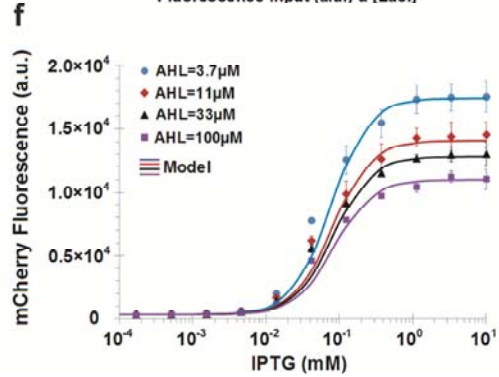
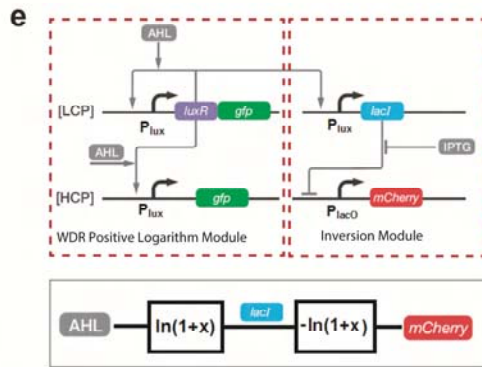
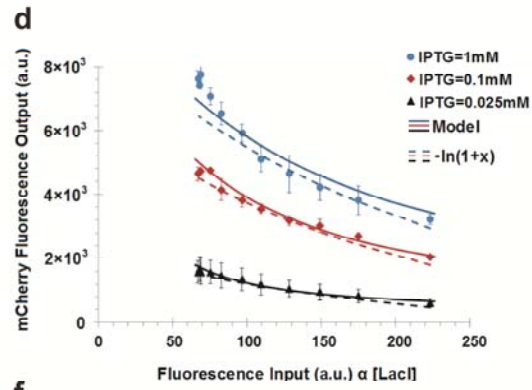
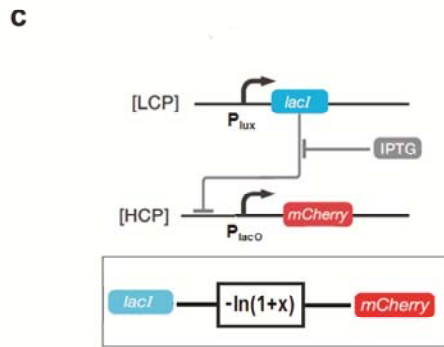
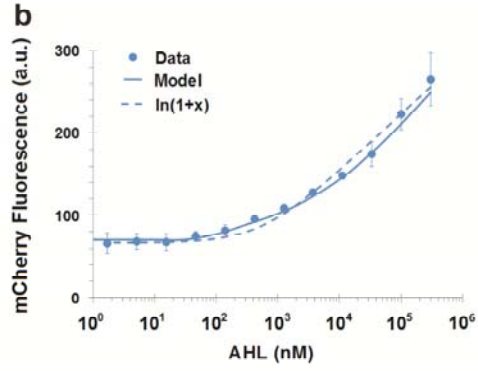
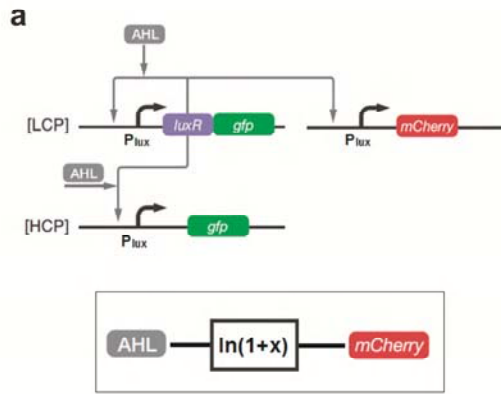
Supplementary Figures 30a-b illustrate that graded positive feedback, whether accomplished by altering the  $K_d$  in Eqs. 79.1–79.4 or by altering the copy-number ratio in Eqs. 80.1–80.7, widens the log-linear dynamic range of operation. Supplementary Figures 30c-d show that the maximum input dynamic range (IDR) of operation in both of these cases occurs when the positive feedback is not too strong or too weak. The exact optimum will depend on the details of the biochemical models and these results correspond to our minimal models. The heat maps shown in Supplementary Figures 30e-g reveal how the IDR, PF, and shunt HCP signals change as the ( $K_d$ , HCP/LCP ratio) vector is varied. Supplementary Figure 30e visually echoes the findings of Supplementary Figures 30c-d, which also reveal that the IDR is maximized when the positive feedback is not too strong or too weak.

## 10 Composition of Analog Functions

Our analog computation modules can be composed into more complex circuits for higher-order functions. To demonstrate such composition, we sought to create a circuit for implementing wide-dynamic-range negative logarithms, a broadly useful computation for calculations such as pH and pKa. This function was built by combining our PF-shunt positive-logarithm motif with a repressor module (Supplementary Figure 31). Since the former has an inducer input and a protein output and the latter has a protein input and a protein output, they can be cascaded together to yield a multi-module system. To achieve this function, we first added an additional output promoter to the LCP in our positive-logarithm PF-shunt motif and showed that its behavior was predicted by our biochemical models and was also well fit by a  $\ln(1+x)$  mathematical function (Supplementary Figure 31a-31b). We then used this output promoter to express the transcriptional repressor protein LacI and thus to repress production of a downstream mCherry protein from a synthetic LacI-regulated promoter ( $P_{lacO}$ ). This LacI-to-mCherry inversion module was accurately matched by our biochemical models and well fit by a mathematical equation of the form  $-\ln(1+x)$  (Supplementary Figure 31c-31d). The combined wide-dynamic-range negative-logarithm circuit is a cascade of the wide-dynamic-range positive-

logarithm circuit and an inversion module (Supplementary Figure 31e) and exhibits a maximal dynamic range of over four orders of magnitude (i.e., >10,000-fold range of inputs), where the dynamic range is taken to be the span of inputs over which the output is well-fit by  $-\ln(x)$  (Supplementary Fig. 31g and Supplementary Figure 20). To tune the output of the wide-dynamic-range negative logarithm, we varied levels of the LacI inducer, IPTG (Supplementary Fig. 31f-g). Such tuning could also be achieved without the use of external inducers by tagging LacI with an *ssrA*-based degradation tag and expressing it from a weaker ribosome-binding sequence (Supplementary Figure 20e), or by mutagenizing the LacI transcription factor or its cognate promoter.

Complex synthetic analog circuits can be designed using detailed biochemical models. However, a simpler predictive abstraction can be derived from the fact that the behavior of our circuit motifs can be well fit to logarithmic functions. These biochemical models and mathematical functions provide complementary tools with varying levels of granularity for composing simple analog circuit modules (e.g., input-inducer-to-output-protein modules and input-protein-to-output-protein modules) to implement more complex functions in a predictable fashion. Indeed, abstractions with different levels of granularity are commonly used in other engineering fields during various stages of design<sup>1</sup>. For example, the straightforward cascade of logarithms from Supplementary Fig. 31b and Supplementary Fig. 31d yields a good fit to the experimental data (Supplementary Fig. 31h). Furthermore, mathematical approximations can simplify this cascade to a negative logarithm  $-\ln(x)$  over the experimentally observed wide dynamic range (Supplementary Information Section 4 and Supplementary Fig. 20).



**Supplementary Figure 31.** A synthetic two-stage analog cascade implementing a wide-dynamic-range negative-slope logarithm computation. **(a)** We modified the LuxR-based PF-shunt positive-logarithm circuit to include an additional output on the LCP, which is quantified by expression of mCherry. **(b)** AHL-to-mCherry transfer function: The solid line indicates modeling results of the detailed biochemical model whereas the dashed line shows the fit of a mathematical function of the form  $\ln(1 + x)$ . **(c)** An inversion module with input protein LacI, expressed from a LCP, and output protein mCherry, under the control of a HCP  $P_{\text{lacO}}$  promoter. **(d)** LacI-to-mCherry transfer function for different IPTG concentrations. LacI was expressed by replacing mCherry in Supplementary Fig. 31a with the *lacI* gene and thus, the mCherry fluorescence at a given AHL concentration was used as a surrogate for quantifying LacI concentration for a given AHL concentration. The solid line indicates modeling results of the detailed biochemical model whereas the dashed line shows the fit of a mathematical function of the form  $-\ln(1 + x)$ . **(e)** The negative-slope logarithm circuit combines the wide-dynamic-range (WDR) PF-shunt positive-logarithm circuit with the LacI-to-mCherry circuit. **(f)** By varying the amount of LacI produced using AHL, we achieve tunable IPTG-to-mCherry transfer functions. Solid lines indicate modeling results of the detailed biochemical model. Even at very high IPTG concentrations, increasing the amount of LacI reduced mCherry output. **(g)** Our circuit topology performs negative-slope logarithms on its input, AHL, to yield a mCherry output, over more than four orders of magnitude. The slope of the negative logarithm can be tuned with different IPTG concentrations. Solid lines indicate modeling results of the detailed biochemical model. **(h)** By simply cascading the  $\ln(1 + x)$  function that describes the PF-shunt positive-logarithm in Supplementary Fig. 31b with the  $-\ln(1 + x)$  function that describes the LacI-to-mCherry module in Supplementary Fig. 31d, we can describe the behavior of the wide-dynamic-range negative-logarithm circuit.

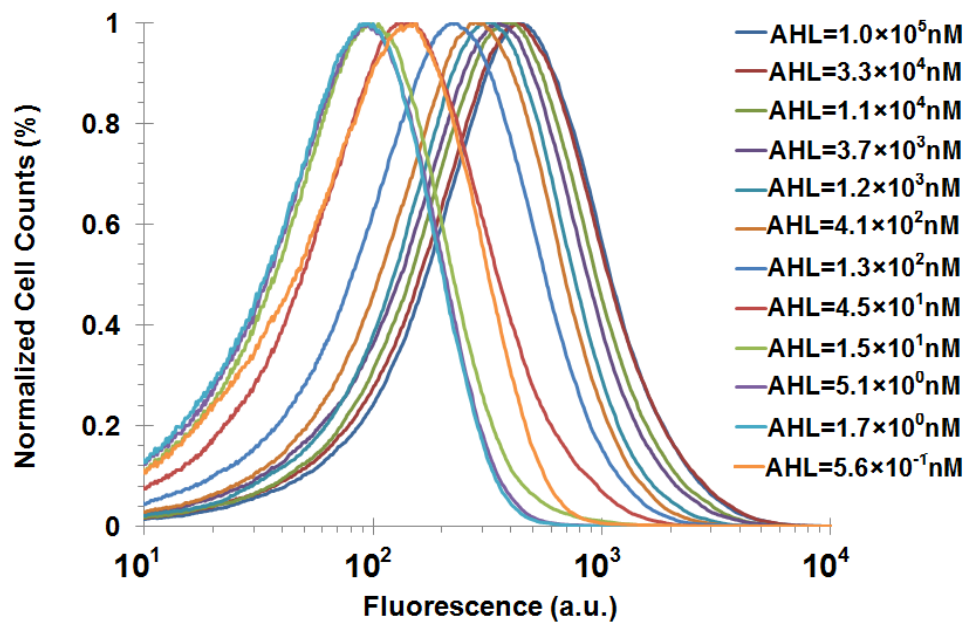
## 11 Potential Applications of Synthetic Analog Circuits

We have shown that our analog motifs can be applied to different transcription factor families (e.g., AraC and LuxR). Thus, our analog circuits should be generalizable to other TF-inducer systems via part mining to enable wide-dynamic-range biosensors that provide quantitative measurements of inducer concentrations rather than binary read-outs<sup>41,42</sup>. The mechanisms underlying our analog circuits may be adaptable to other host cells, including yeast and mammalian cells. Indeed, shunt or decoy TF binding sites are naturally present in eukaryotes and are expected to influence the behavior of gene networks<sup>43</sup>. They may also find applications in biotechnology by allowing engineers to finely tune the expression level of toxic proteins, enzymes in a metabolic pathway, or stress-response proteins<sup>44,45</sup>. For example, ratios between small-molecules (e.g., NAD<sup>+</sup>/NADH) and proteins (e.g., Oct3/4, Sox2, Klf4, and c-Myc for cellular reprogramming) are important control parameters that could serve as inputs into ratiometric circuits that trigger downstream effectors. More advanced systems may incorporate

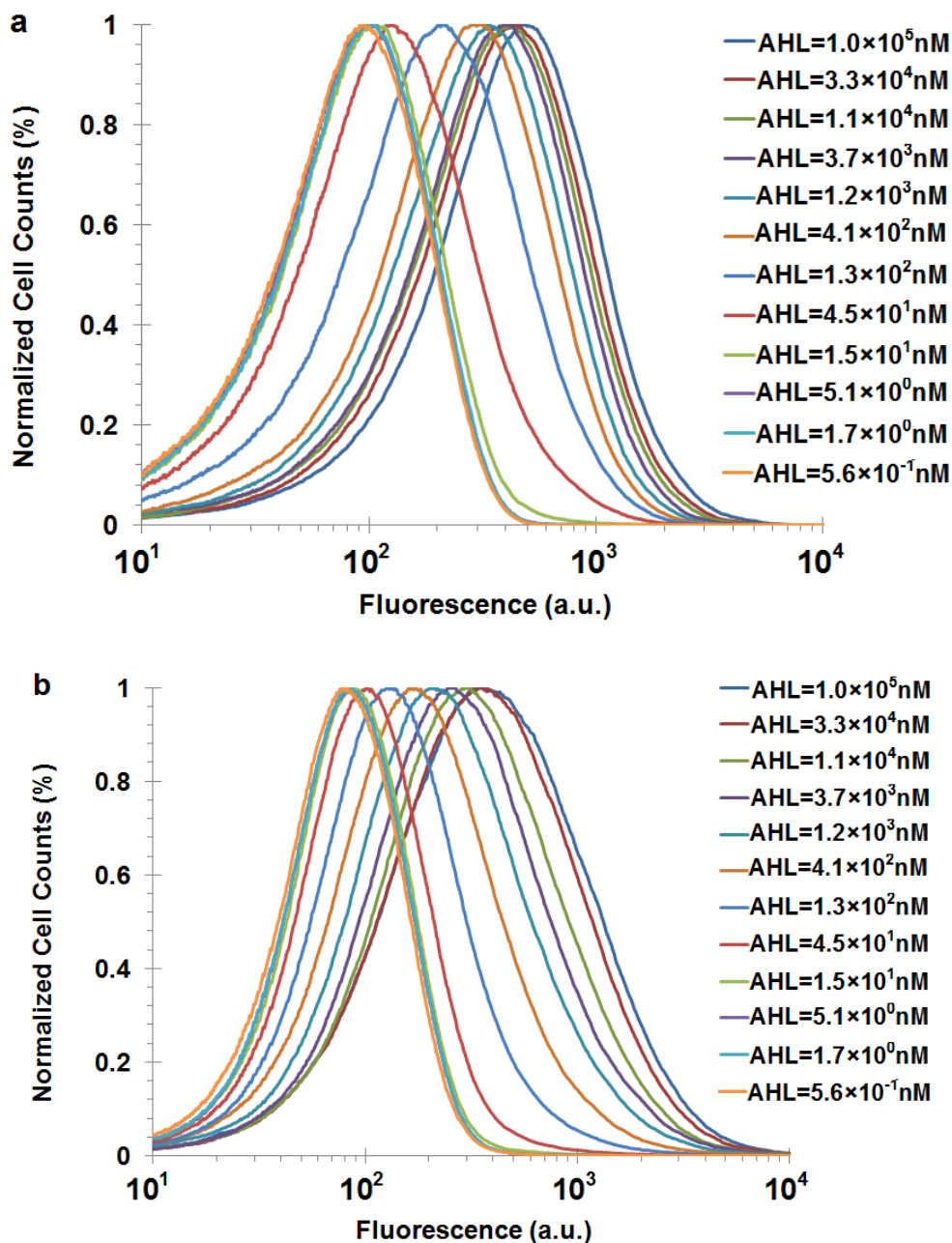
analog biosensors with feedback control of endogenous genetic circuits to regulate phenotypes in a precise and dynamic fashion.

## 12 FACS Data

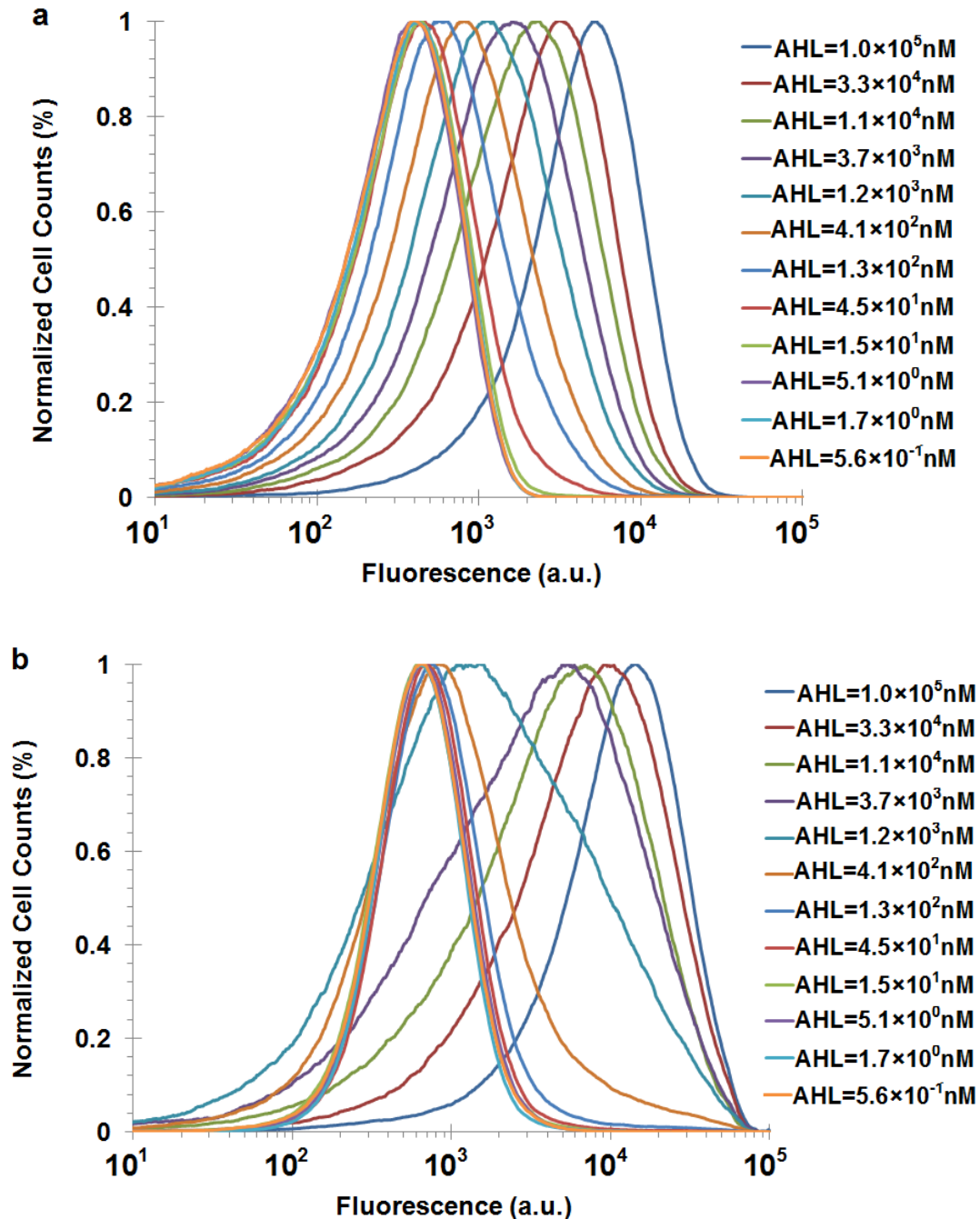
All fluorescence intensities were smoothed using Matlab.



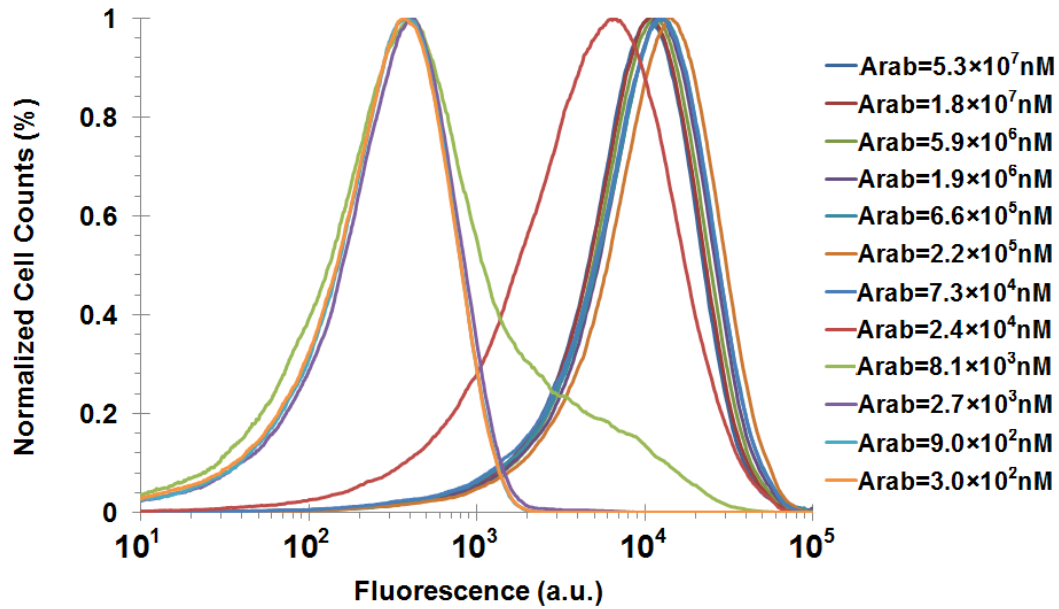
**Supplementary Figure 32.** GFP flow cytometry data for a population of cells containing the LuxR-GFP-based positive-feedback circuit on a LCP under the control of the  $P_{lux}$  promoter (Fig. 2a).



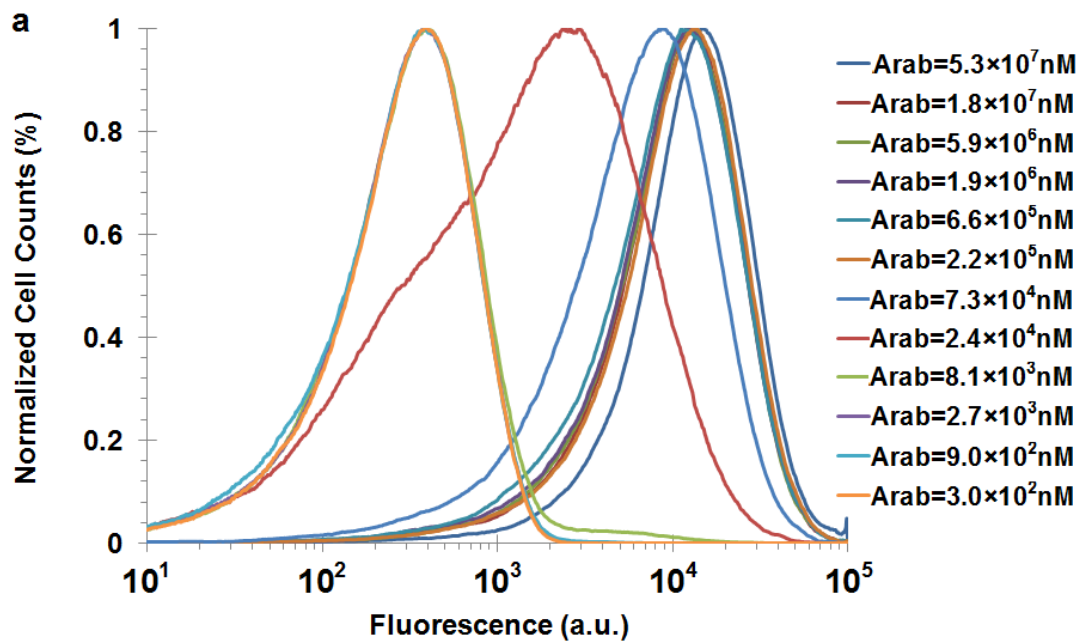
**Supplementary Figure 33.** Flow cytometry data for a population of cells containing the wide-dynamic-range positive-slope circuit with the  $P_{lux}$  promoter driving expression of LuxR-GFP from a LCP and a different  $P_{lux}$  promoter driving expression of mCherry from a MCP shunt (Fig. 2a). (a) GFP fluorescence. (b) mCherry fluorescence.

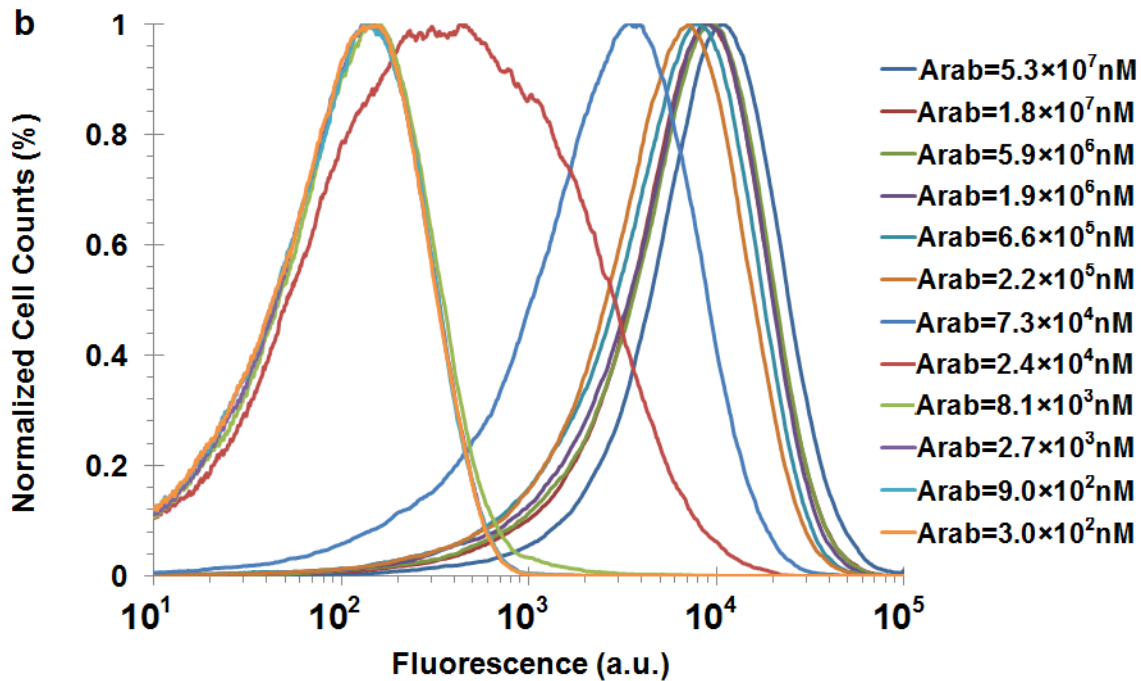


**Supplementary Figure 34.** Flow cytometry data for a population of cells containing the wide-dynamic-range positive-slope circuit with the  $P_{lux}$  promoter driving expression of LuxR-GFP from a LCP and a different  $P_{lux}$  promoter driving expression of mCherry from a HCP shunt (Fig. 2a). (a) GFP fluorescence. (b) mCherry fluorescence.

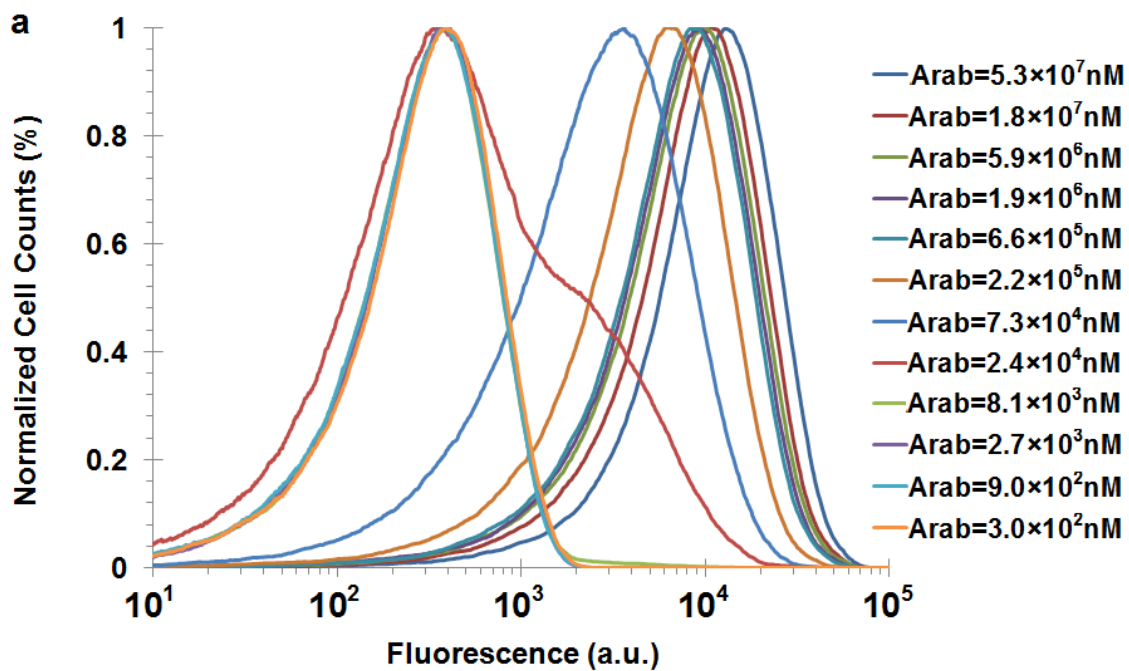


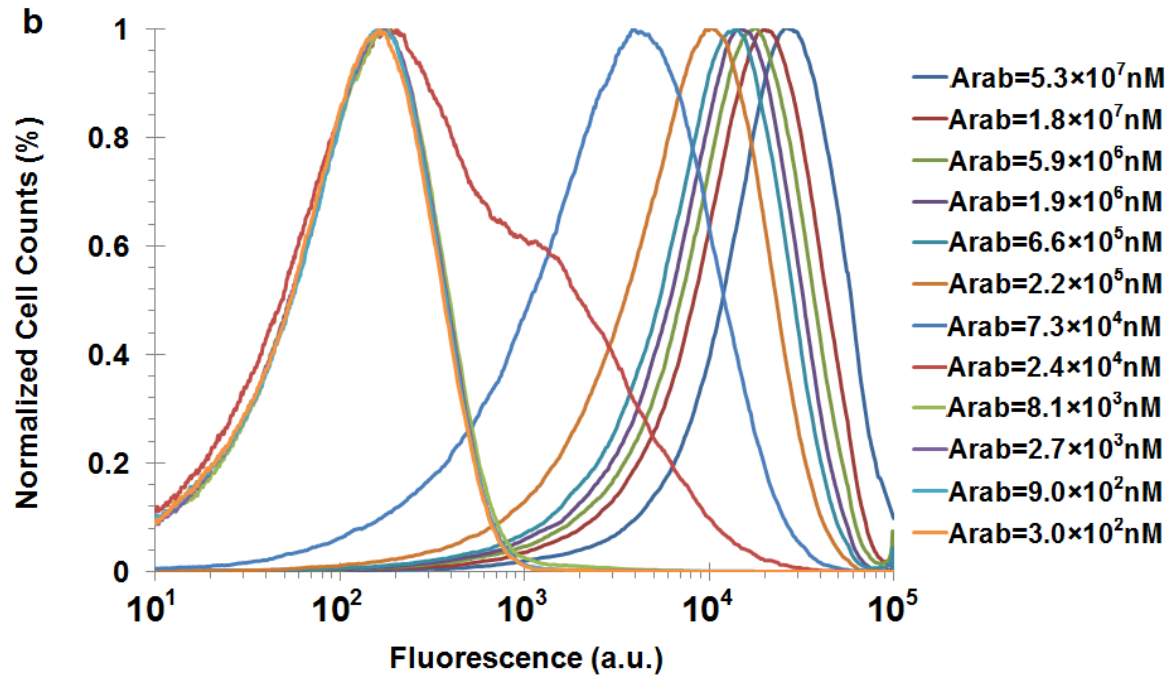
**Supplementary Figure 35.** GFP flow cytometry data for a population of cells containing the AraC-GFP-based positive-feedback circuit on a LCP under the control of the P<sub>BAD</sub> promoter (Fig. 1b).



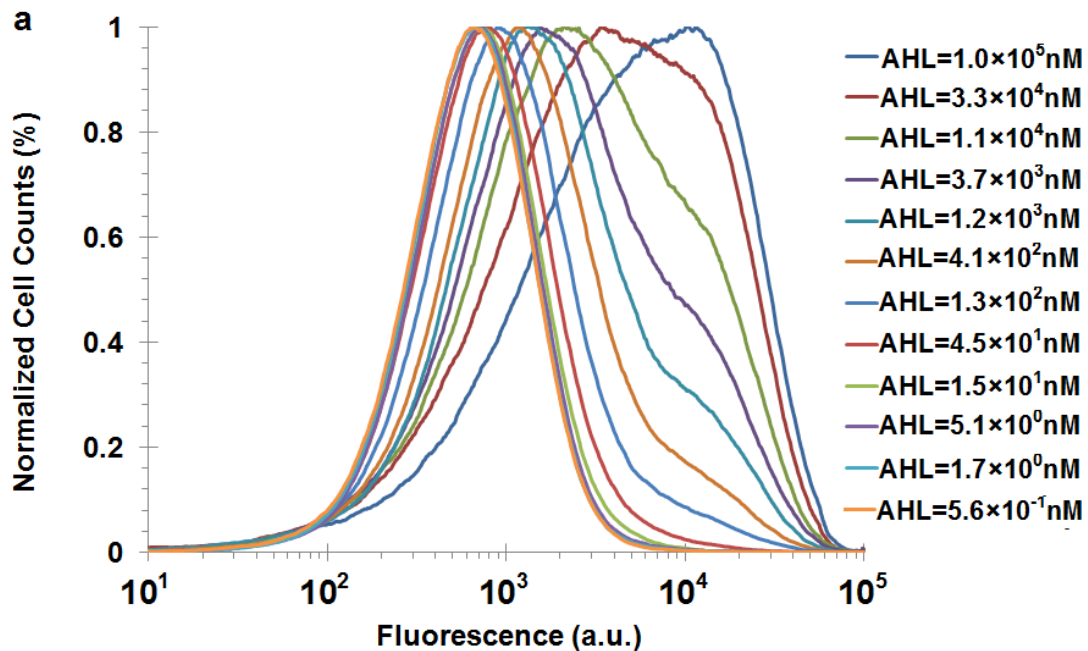


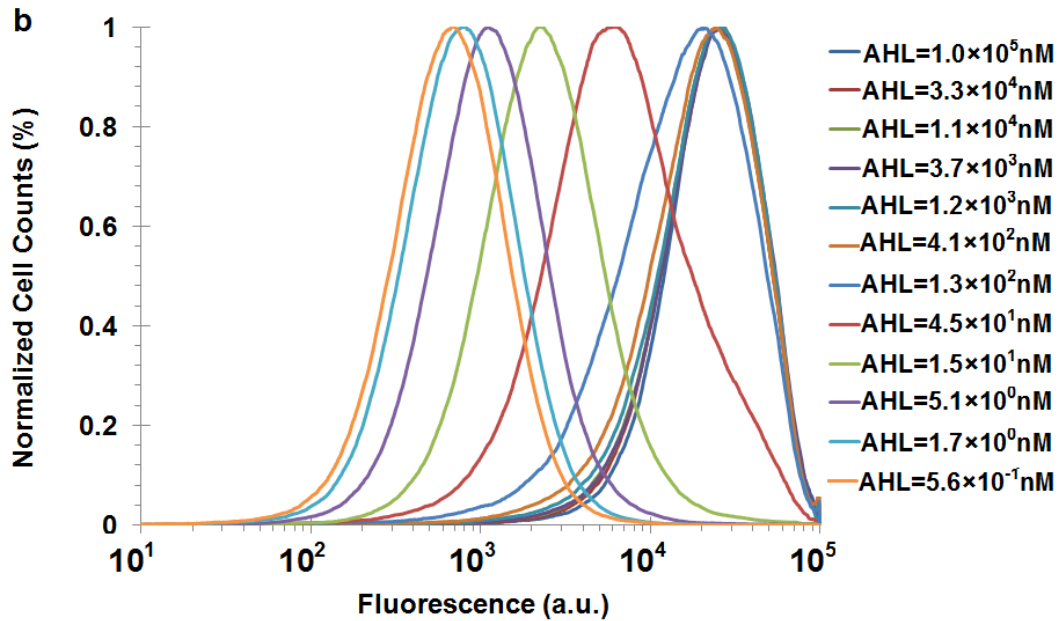
**Supplementary Figure 36.** Flow cytometry data for a population of cells containing the wide-dynamic-range positive-slope circuit with the  $P_{BAD}$  promoter driving expression of AraC-GFP from a LCP and a different  $P_{BAD}$  promoter driving expression of mCherry from a MCP shunt (Fig. 1b). (a) GFP fluorescence. (b) mCherry fluorescence.



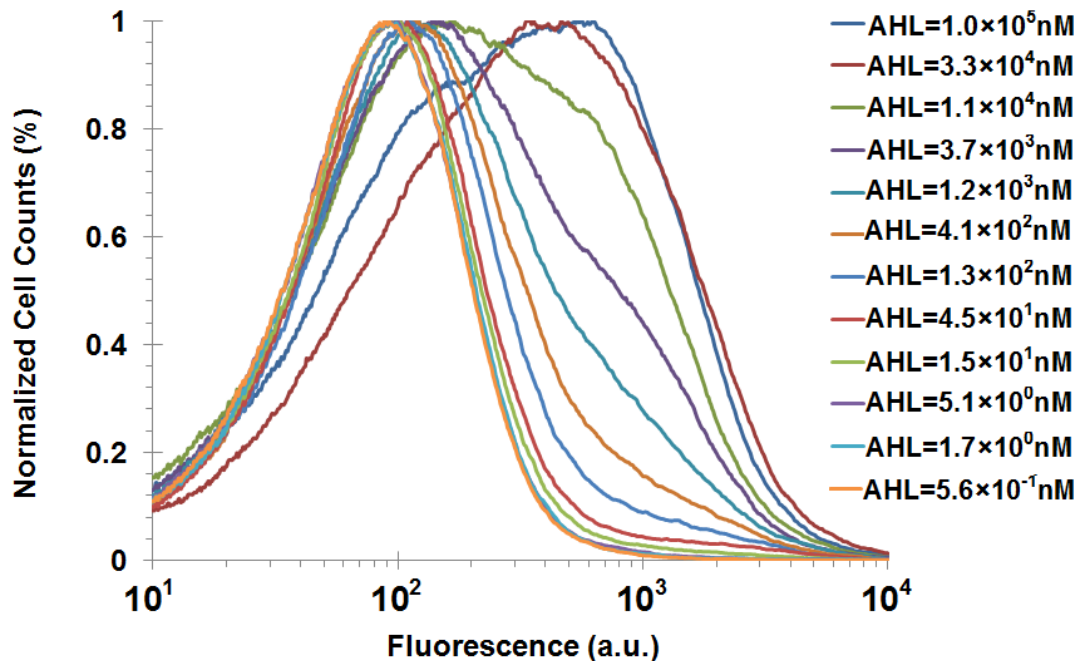


**Supplementary Figure 37.** Flow cytometry data for a population of cells containing the wide-dynamic-range positive-slope circuit with the  $P_{BAD}$  promoter driving expression of AraC-GFP from a LCP and a different  $P_{BAD}$  promoter driving expression of mCherry from a HCP shunt (Fig. 1b). (a) GFP fluorescence. (b) mCherry fluorescence.

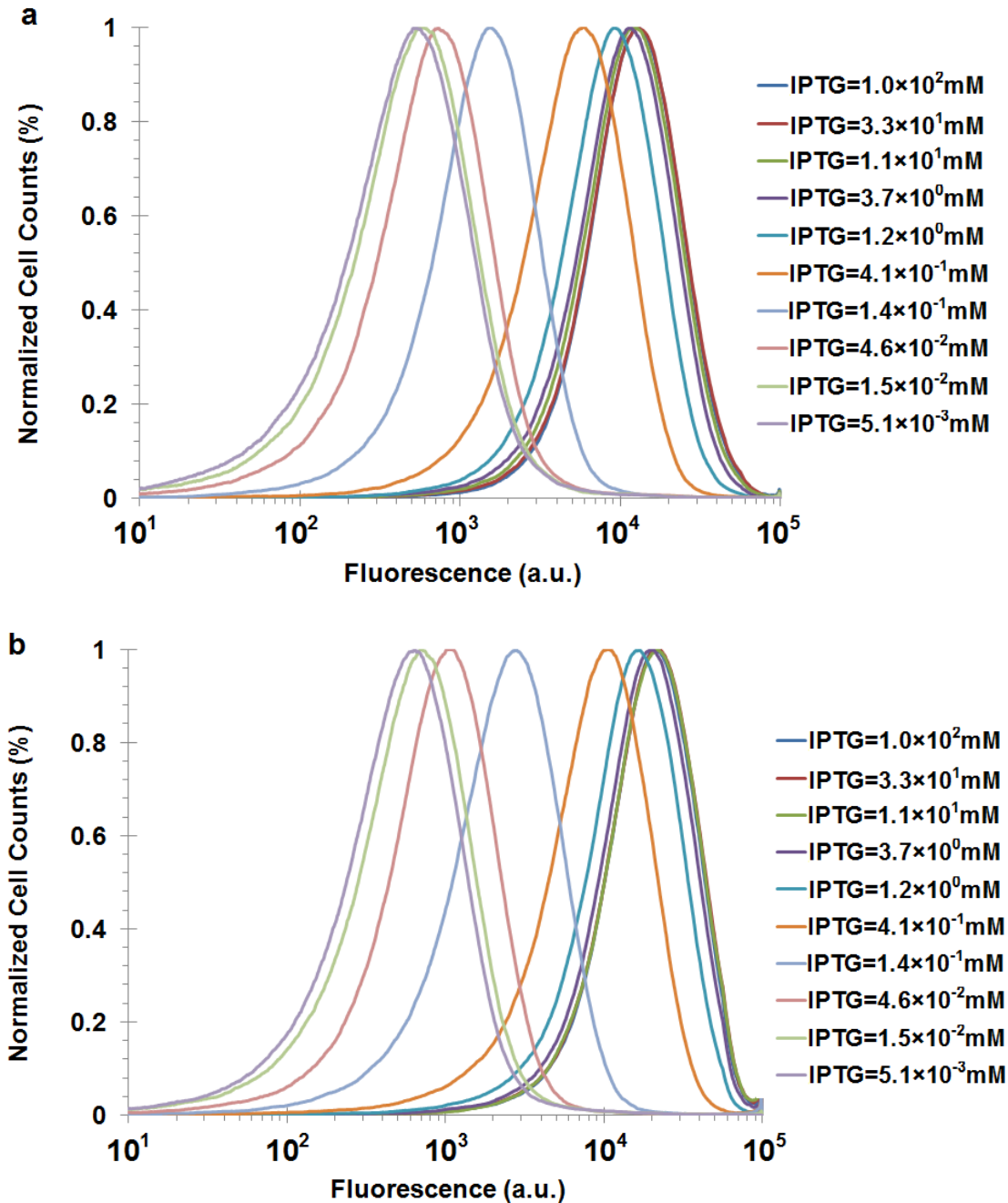




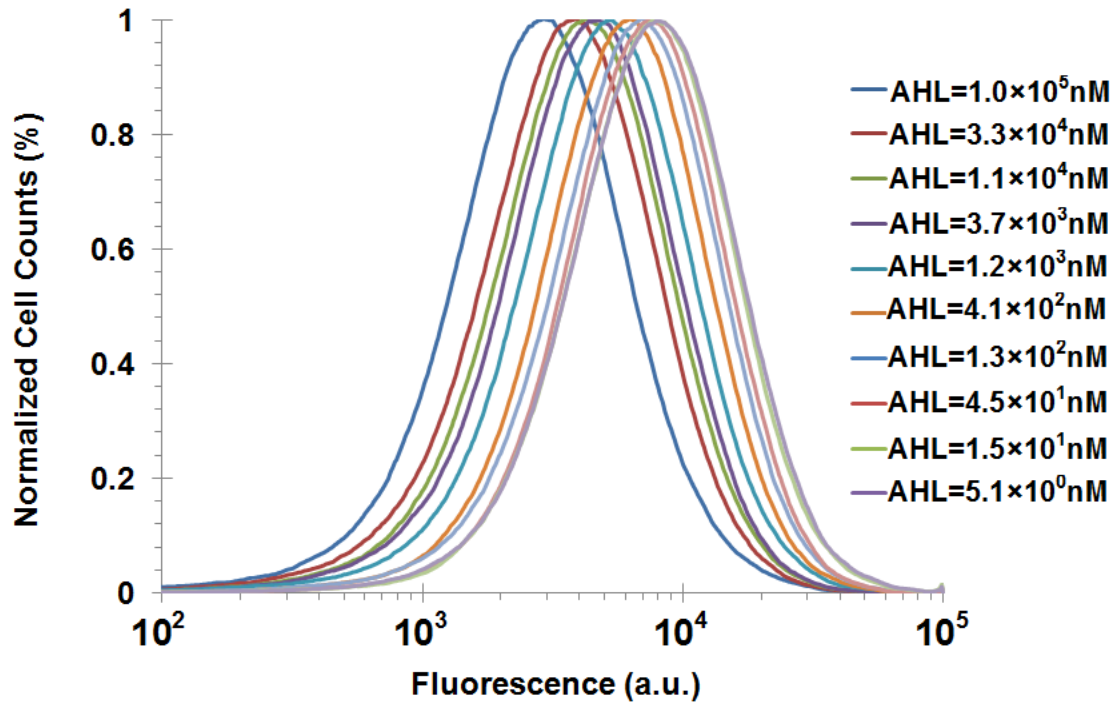
**Supplementary Figure 38.** mCherry flow cytometry data for a population of cells containing the variable plasmid-copy-number system enabling the dynamic switching of transfer functions between analog and digital behaviors. The LuxR-GFP-based positive-feedback circuit is on a VCP and the shunt HCP contains a  $P_{lux}$  promoter (Fig. 2d). (a) No CC (CopyControl). (b) 1X CC.



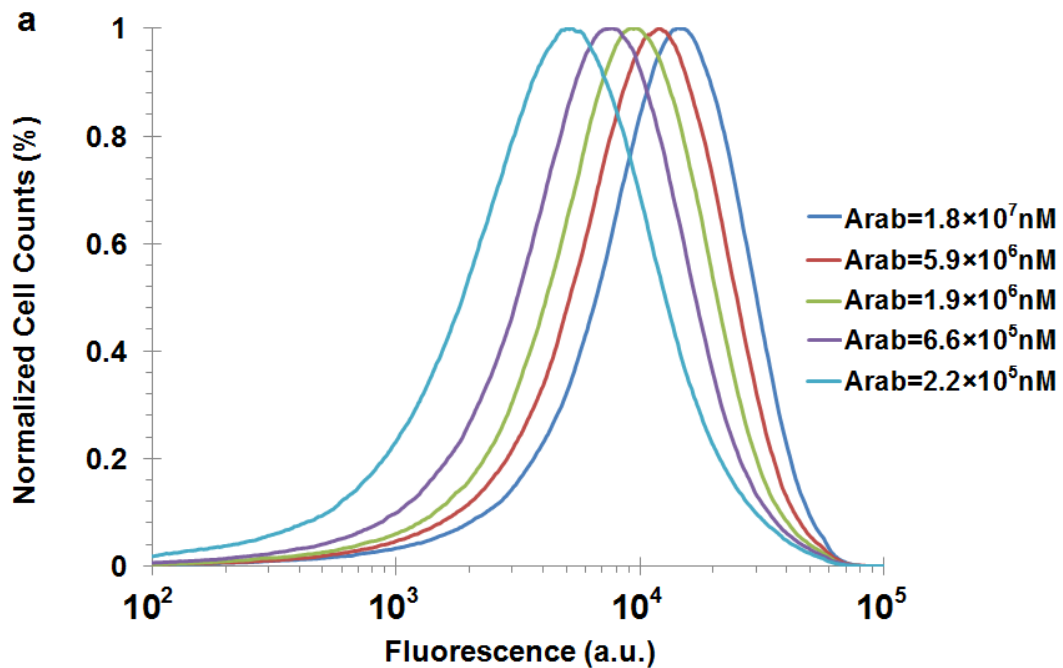
**Supplementary Figure 39.** mCherry flow cytometry data for a population of cells containing the wide-dynamic-range positive-slope circuit with the two  $P_{lux}$  promoters driving expression of LuxR-GFP and mCherry from a LCP and a different  $P_{lux}$  promoter driving expression of GFP from a HCP shunt (Supplementary Figure 31a).

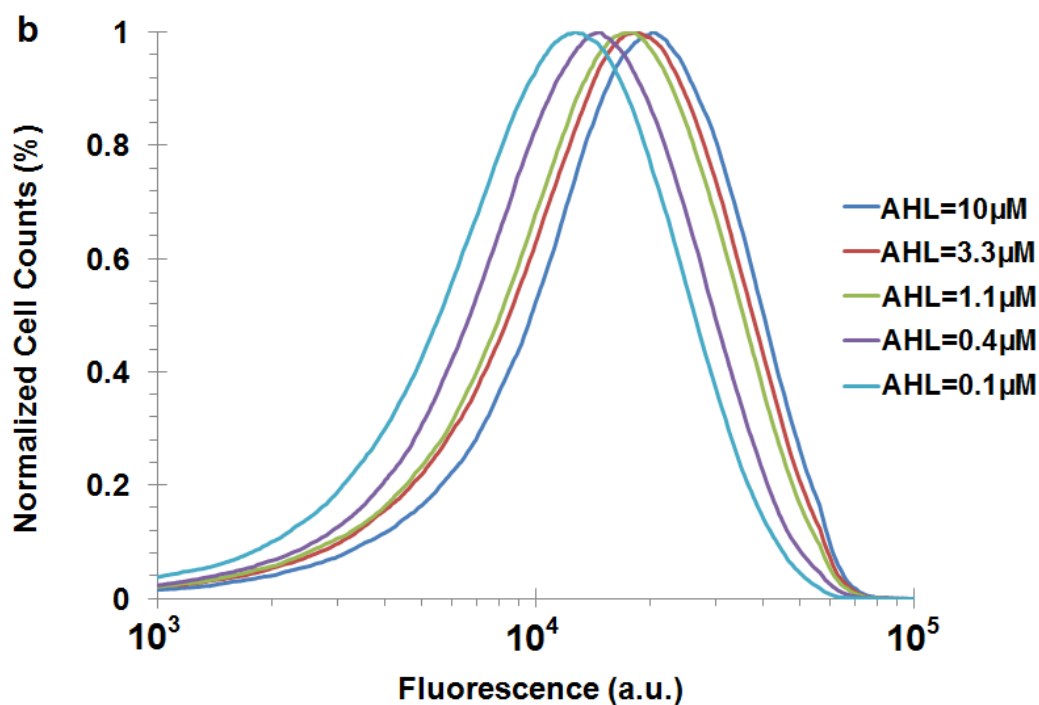


**Supplementary Figure 40.** mCherry flow cytometry data for a population of cells containing the  $P_{lacO}$  promoter driving expression of mCherry in the wide-dynamic-range negative-slope circuit (Supplementary Figure 31e). (a) AHL = 100  $\mu$ M. (b) AHL = 3.4  $\mu$ M.

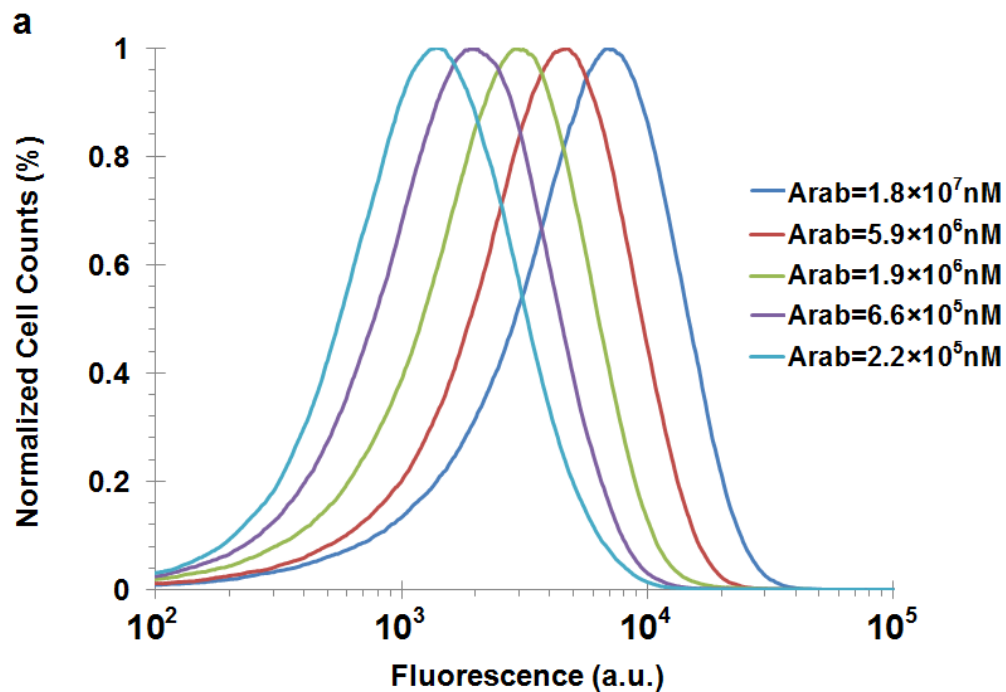


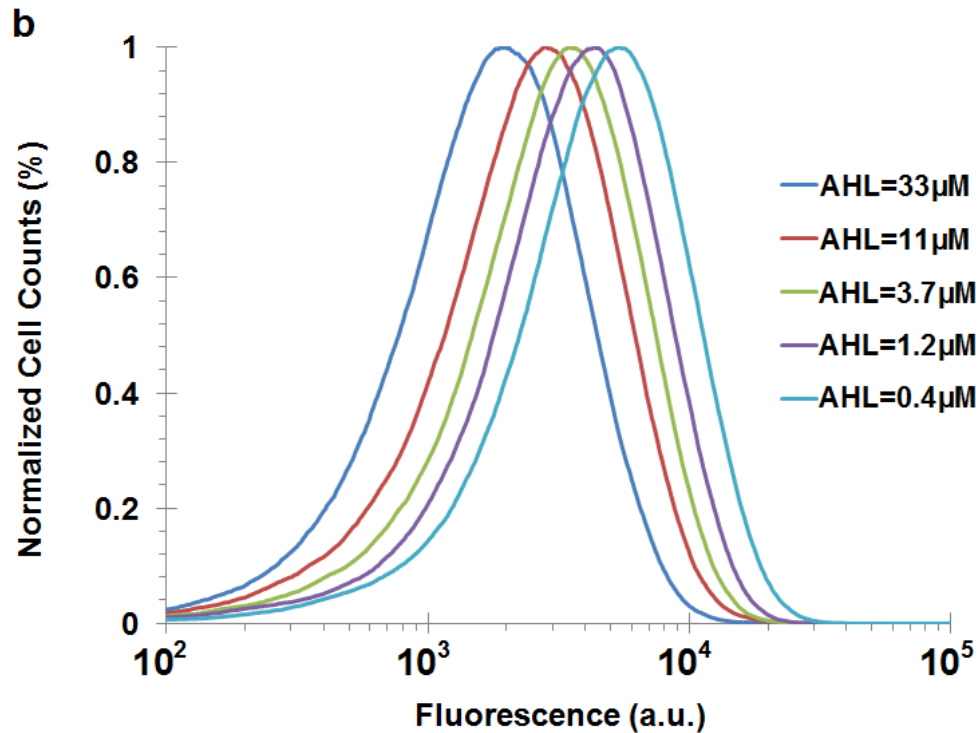
**Supplementary Figure 41.** mCherry flow cytometry data for a population of cells containing the  $P_{lacO}$  promoter driving expression of mCherry in the wide-dynamic-range negative-slope circuit (Supplementary Figure 31e), where IPTG = 1 mM.



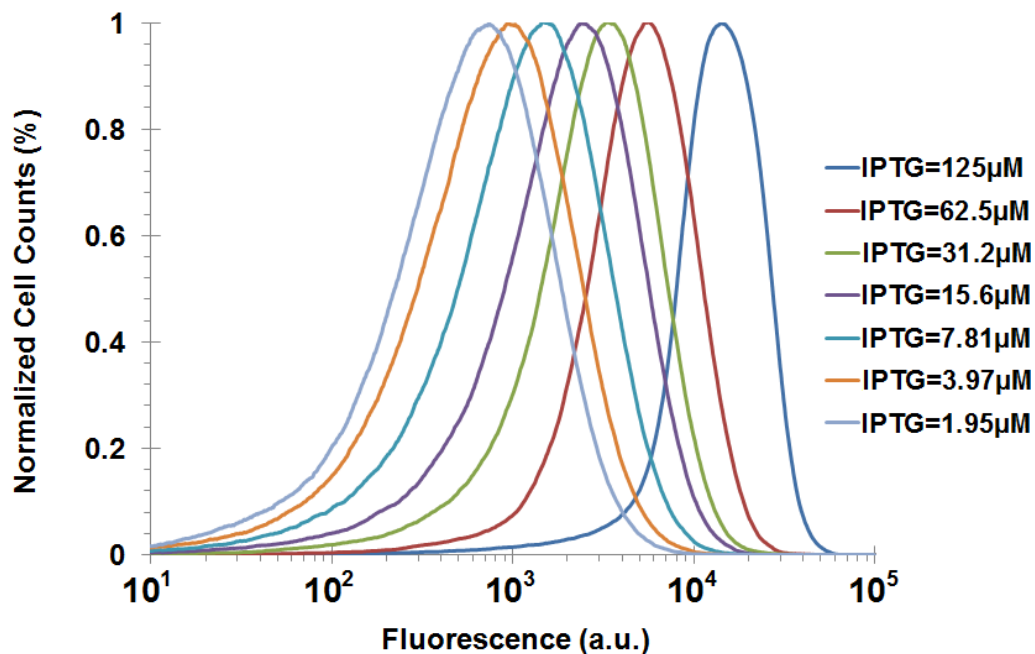


**Supplementary Figure 42.** mCherry flow cytometry data for a population cells containing the adder circuit (Fig. 3a). (a) AHL was held constant at 10  $\mu$ M and arabinose was varied. (b) Arabinose was held constant at 17.7 mM and AHL was varied.

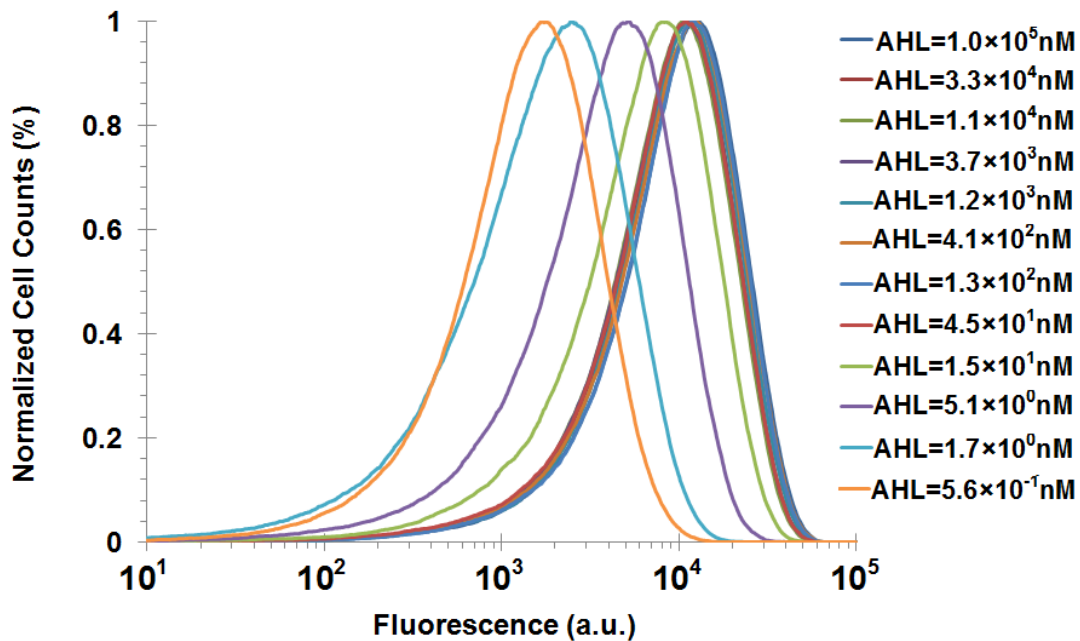




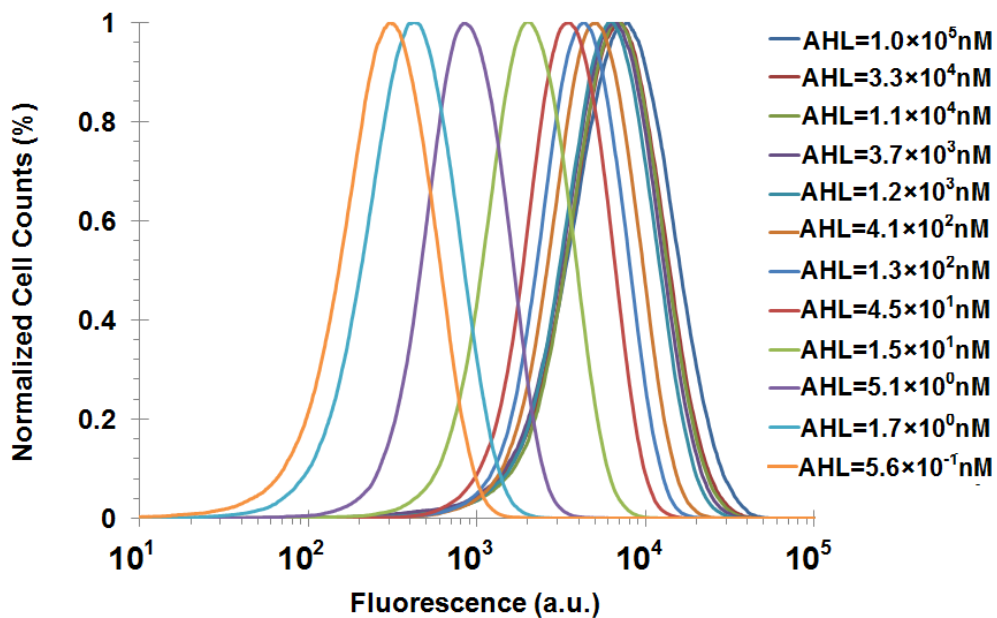
**Supplementary Figure 43.** mCherry flow cytometry data for a population of cells containing the divider (i.e., ratiometer) circuit (Fig. 3c). (a) IPTG was held constant at 1 mM, AHL was held constant at 33  $\mu$ M, and arabinose was varied. (b) IPTG was held constant at 1 mM, arabinose was held constant at 0.66 mM, and AHL was varied.



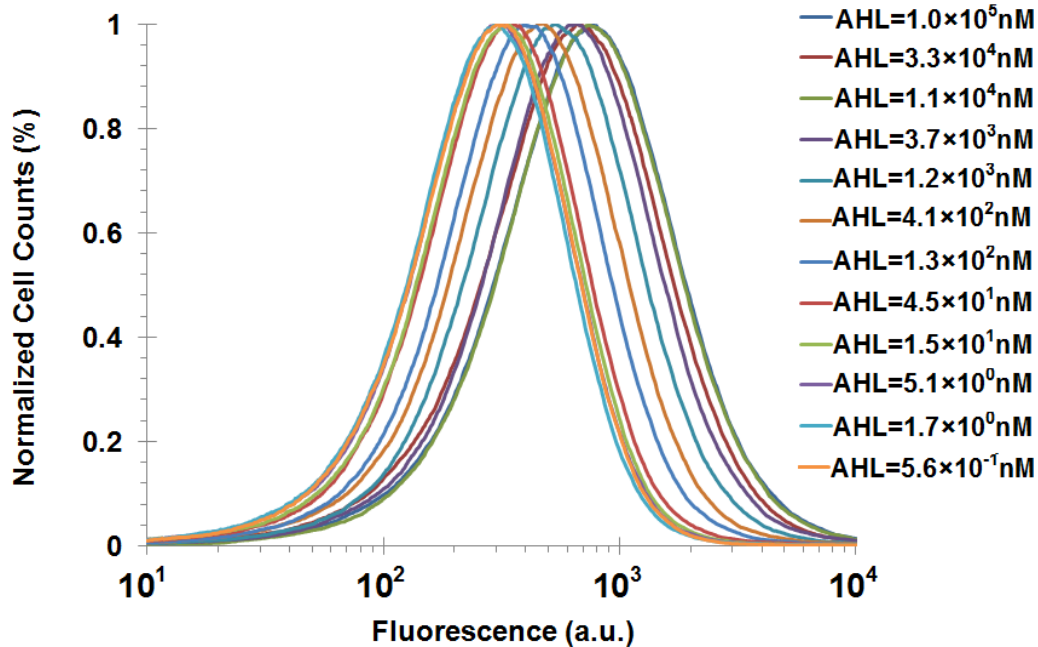
**Supplementary Figure 44.** mCherry flow cytometry data for populations of cells containing power-law circuits (Fig. 3e). Arabinose was held constant at 4.6  $\mu\text{M}$  and IPTG was varied. This circuit contains pRD43 (LCP) and pRD114 (HCP).



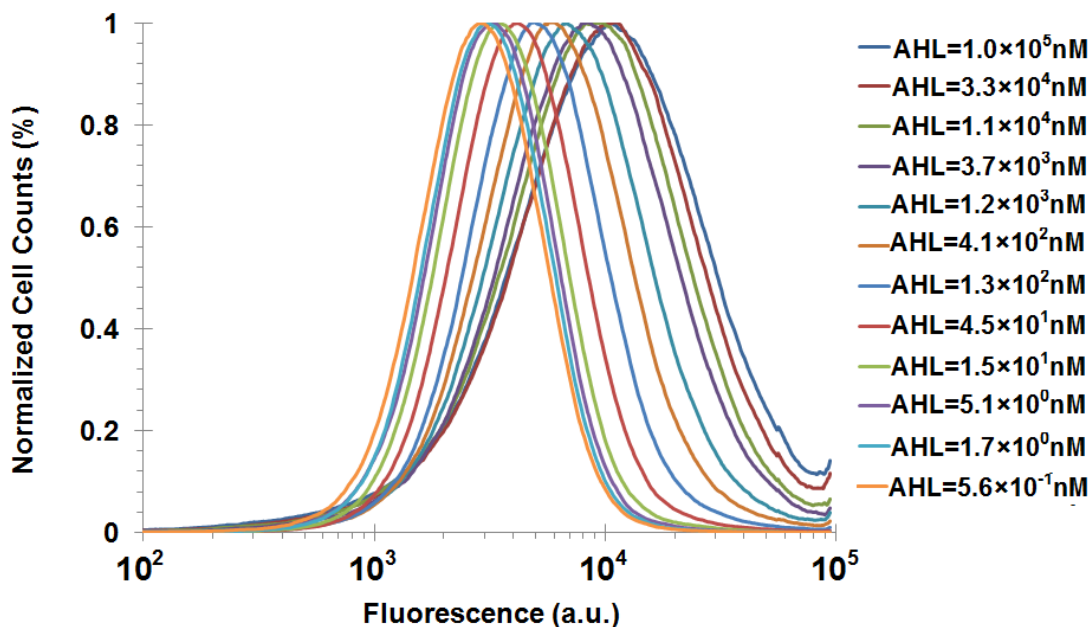
**Supplementary Figure 45.** GFP flow cytometry data for a population of cells expressing GFP under the control of the  $P_{\text{lux}}$  promoter on a LCP (Supplementary Figure 14a, OL: LuxR). The transcription factor LuxR is under the control of the  $P_{\text{lacO}}$  promoter and is expressed from the same LCP as GFP.



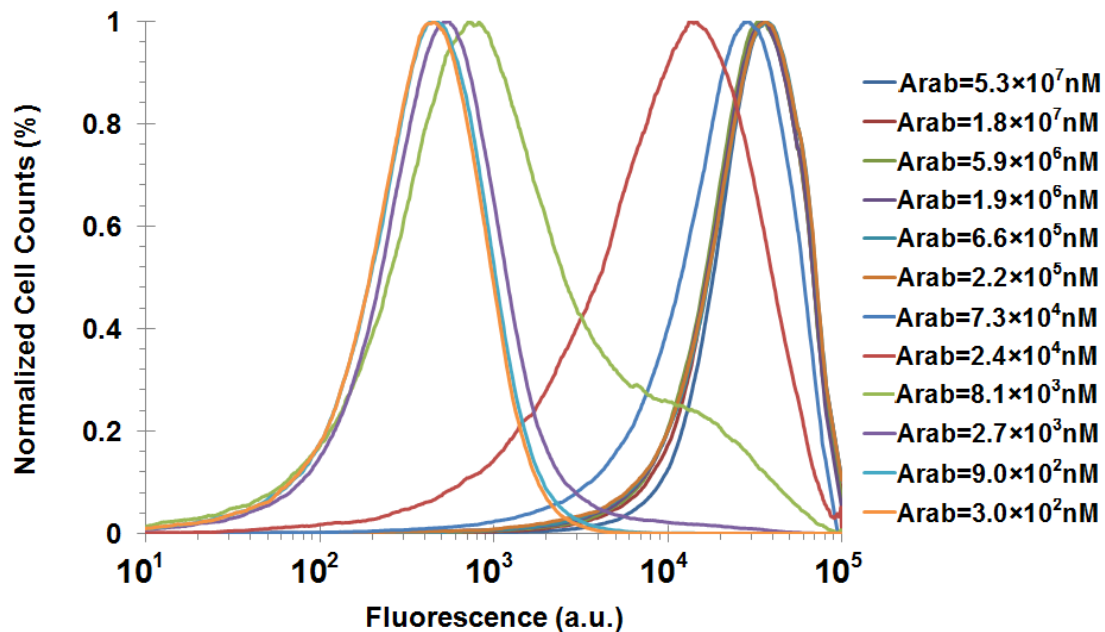
**Supplementary Figure 46.** mCherry flow cytometry data for a population of cells expressing mCherry under the control of the  $P_{lux}$  promoter on a HCP shunt (Supplementary Figure 14b, OL+Shunt: LuxR). The transcription factor LuxR is under the control of the  $P_{lacO}$  promoter and is expressed from a separate LCP.



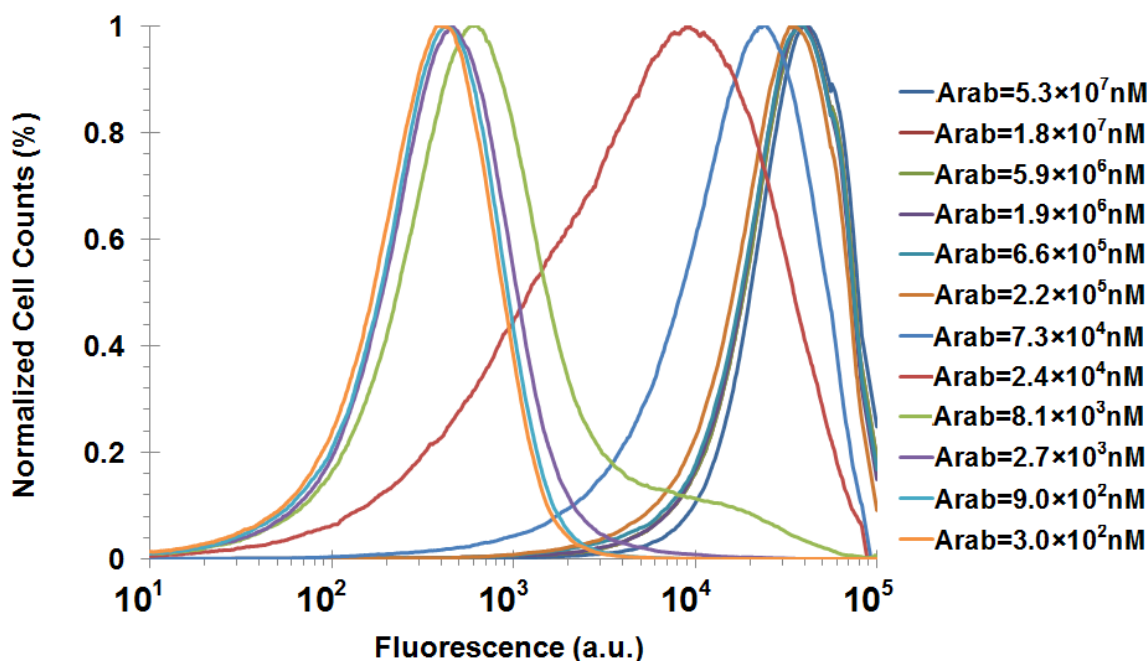
**Supplementary Figure 47.** mCherry flow cytometry data for a population of cells expressing mCherry under the control of the  $P_{lux}$  promoter on a LCP (Supplementary Figure 14c, OL: LuxR-GFP). The transcription factor LuxR is fused to GFP, is under the control of the  $P_{lacO}$  promoter, and is expressed from the same LCP as mCherry.



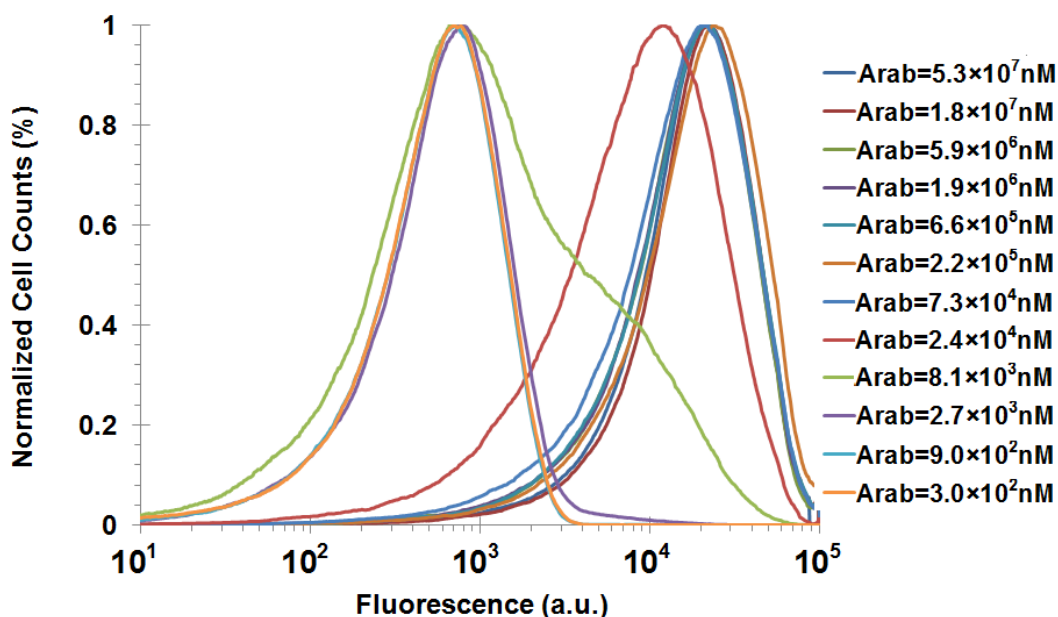
**Supplementary Figure 48.** mCherry flow cytometry data for a population of cells expressing mCherry under the control of the  $P_{lux}$  promoter on a HCP shunt (Supplementary Figure 14d, OL+Shunt: LuxR-GFP). The transcription factor LuxR is fused to GFP, is under the control of the  $P_{lacO}$  promoter, and is expressed from a separate LCP.



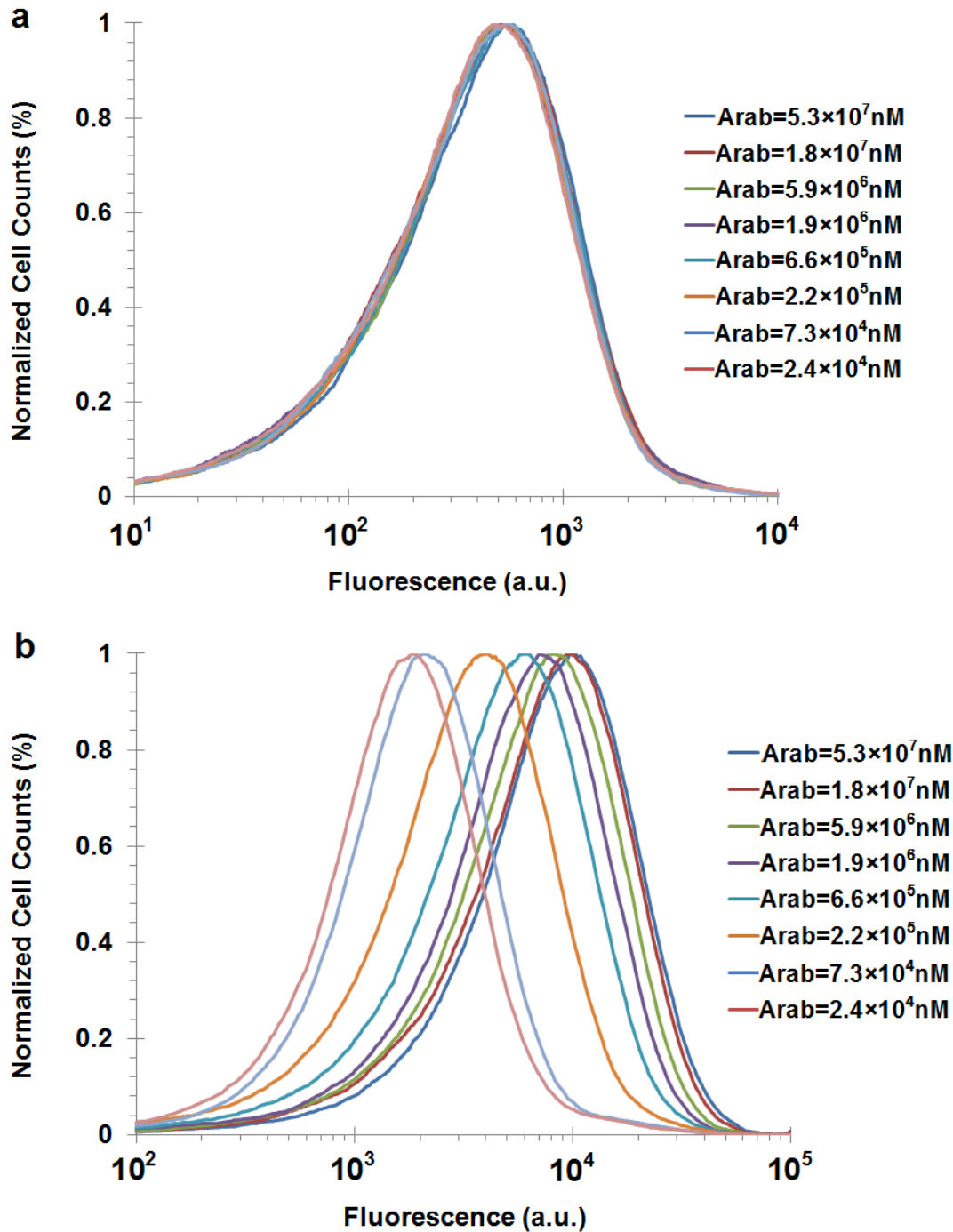
**Supplementary Figure 49.** mCherry flow cytometry data for a population of cells expressing mCherry under the control of the  $P_{BAD}$  promoter on a HCP shunt (Supplementary Figure 16a, OL+Shunt: AraC). The transcription factor AraC is under the control of the  $P_{lacO}$  promoter, and is expressed from a separate LCP.



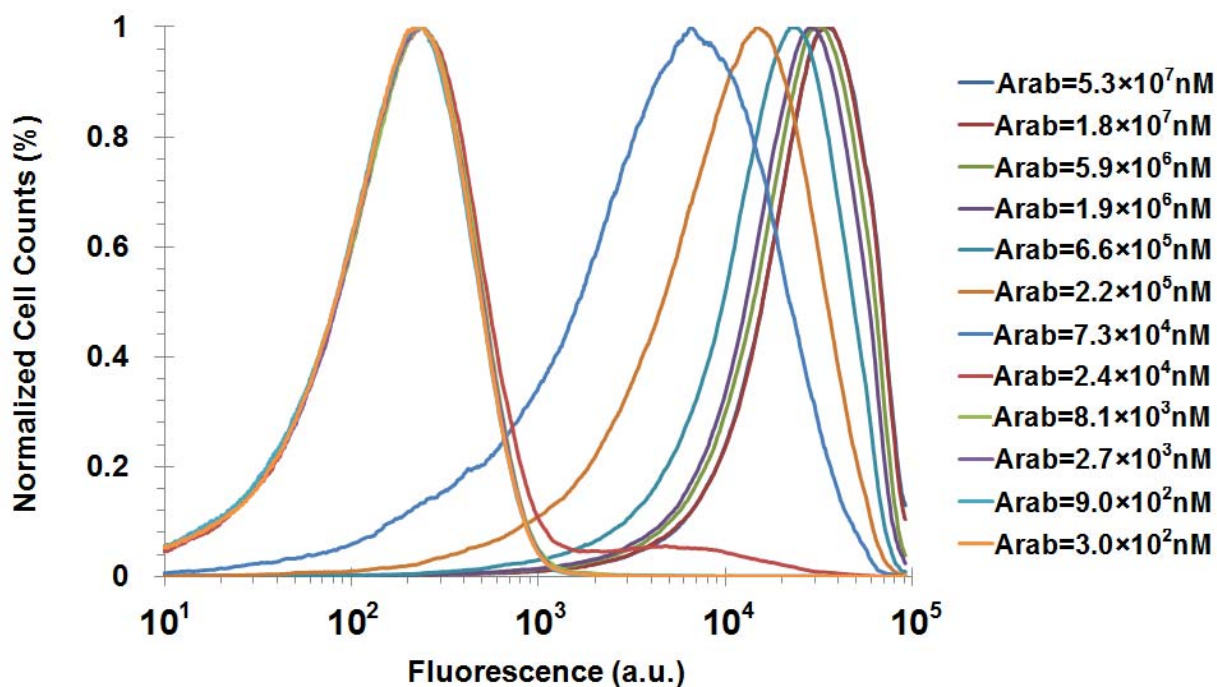
**Supplementary Figure 50.** mCherry flow cytometry data for a population of cells expressing mCherry under the control of the  $P_{BAD}$  promoter on a HCP shunt (Figure 1c, Supplementary Figure 16b, OL+Shunt: AraC-GFP). The transcription factor AraC is fused to GFP, is under the control of the  $P_{lacO}$  promoter, and is expressed from a separate LCP.



**Supplementary Figure 51.** GFP flow cytometry data for a population of cells containing the AraC-GFP-based positive feedback circuit on a LCP and a dummy shunt HCP containing the  $P_{lux}$  promoter (Supplementary Figure 17a).



**Supplementary Figure 52.** mCherry flow cytometry data for a population of cells containing the positive-logarithm circuit that can be digitally toggled by leveraging the hybrid promoter  $P_{lacO/ara}$  as an output (Supplementary Figure 24). **(a)** AHL was held constant at 5  $\mu$ M, IPTG was held at 0 mM, and arabinose was varied. **(b)** AHL was held constant at 5  $\mu$ M, IPTG was held at 0.7 mM, and arabinose was varied.



**Supplementary Figure 53.** mCherry flow cytometry data for a population of cells containing the wide-dynamic-range positive-slope circuit with the  $P_{BAD}$  promoter driving expression of AraC-GFP from a LCP and a double  $P_{BAD}$  promoter driving expression of mCherry from a HCP shunt (Supplementary Figure 25a).

### 13 Plasmid Construction

All the plasmids in this work were constructed using basic molecular cloning techniques<sup>19</sup>. New England Biolab's (Beverly, MA) restriction endonucleases, T4 DNA Ligase, and Taq Polymerase were used. PCRs were carried out with a Bio-Rad S1000™ Thermal Cycler With Dual 48/48 Fast Reaction Modules. Synthetic oligonucleotides were synthesized by Integrated DNA Technologies (Coralville, IA). As described in the Methods Summary, plasmids were transformed into *E. coli* 10β (araD139 Δ(ara-leu)7697 fhuA lacX74 galK (φ80 Δ(lacZ)M15) mcrA galU recA1 endA1 nupG rpsL (StrR) Δ(mrr-hsdRMS-mcrBC)), *E. coli* EPI300 (F-mcrA Δ(mrr-hsdRMS-mcrBC) Φ80dlacZΔM15 ΔlacX74 recA1 endA1 araD139 Δ(ara, leu)7697 galU galK λ-rpsL (StrR) nupG trfA tonA), or *E. coli* MG1655 Pro which contains integrated constitutive constructs for TetR and LacI proteins (Supplementary Figure 14e and 15c)<sup>15</sup>, with a standard heat shock protocol<sup>19</sup>. Plasmids were isolated with Qiagen QIAprep Spin Miniprep Kits and modifications were confirmed by restriction digests and sequencing by Genewiz (Cambridge, MA).

All devices (promoter-RBS-gene-terminator) were initially assembled in the Lutz and Bujard expression vector pZE11G<sup>15</sup> containing ampicillin resistance and the ColE1 origin of replication.

Parts are defined as promoters, RBSs, genes, and terminators. Manipulation of different parts of the same type were carried out using the same restriction sites. For example, to change a gene in a device we used KpnI and XmaI. To assemble two devices together, we used a single restriction site flanking one device and used oligonucleotide primers and PCR to add that restriction site to the 5' and 3' ends of a second device. After assembling devices in the ampicillin-resistant ColE1 backbone, antibiotic-resistance genes were changed using AatII and SacI, and origin of replications were changed with SacI and AvrII. For gene fusions, oligonucleotide primers were designed to delete the stop codon in the C-terminus of the first gene as well as the start codon in the N-terminus of the second gene and to insert a 12-bp (Gly-Gly-Ser-Gly) linker between the two genes. The genes were amplified separately with appropriate primers using standard PCR techniques and the PCR products were assembled in a subsequent PCR reaction with the linker region serving as means of annealing the two templates. The variable copy plasmid (VFP) containing  $P_{lux}$  positive feedback was built by adding an AatII site to the 5' end and a PacI site to the 3' end of the  $P_{lux}$  positive feedback device using PCR. This PCR product was cloned into the AatII and PacI sites of a pBAC/oriV vector<sup>17</sup>.

**Supplementary Table 3.** List of strains used in this study

Circuit	Schematic	Output	Input	Parameter	Plasmids
PF LCN	Figure 2a	GFP	AHL		pRD152
PF LCN + Shunt MCP	Figure 2a	GFP, mCherry	AHL		pRD152, pRD318
Positive WDR*	Figure 2a	GFP, mCherry	AHL		pRD152, pRD58
PF LCN	Figure 1b	GFP	Arab		pRD123
PF LCN + Shunt MCP	Figure 1b	GFP, mCherry	Arab		pRD123, pRD357
Positive WDR*	Figure 1b	GFP, mCherry	Arab		pRD123, pRD131
D/A** Positive WDR*	Figure 2d	mCherry	AHL	CC(0,1x)	pJR378, pRD58
Positive WDR DP***	Suppl. Fig. 25	mCherry	Arab		pRD123, pRD10
Positive WDR-3Output	Suppl. Fig. 31a	mCherry	AHL		pJR570, pRD58
Negative WDR	Suppl. Fig. 31e	mCherry	AHL	IPTG	pRD289, pRD293
Adder	Figure 3a	mCherry	AHL, Arab		pRD258, pRD238
Ratiometer	Figure 3c	mCherry	AHL, Arab	IPTG	pRD289, pRD362
Power Law	Figure 3e	mCherry	IPTG	Arab	pRD43, pRD114
OL: LuxR	Suppl. Fig. 14a	GFP	AHL		pRD302
OL+Shunt: LuxR	Suppl. Fig. 14b	mCherry	AHL		pRD171, pRD58
OL: LuxR-GFP	Suppl. Fig. 14c	mCherry	AHL		pRD397
OL+Shunt: LuxR-GFP	Suppl. Fig. 14d	mCherry	AHL		pRD331, pRD58
OL+Shunt: AraC	Suppl. Fig. 16a	mCherry	Arab		pRD89, pRD131
OL+Shunt: AraC-GFP	Suppl. Fig. 16b	mCherry	Arab		pRD43, pRD131
	Figure 1c				
PF + Dummy Shunt	Suppl. Figure 17a	GFP	Arab		pRD152, pRD58

\*WDR: Wide Dynamic range

\*\*D/A: Digital-to-Analog (in other words, digitally toggleable analog circuit behavior)

\*\*\*WDR DP: Wide Dynamic Range with Double Promoter

**Supplementary Table 4.** List of parts used in this study

Part Name	Description and Source
P <sub>lux</sub>	Lux promoter, BBa_R0062 <sup>21</sup>
P <sub>BAD</sub>	<i>araBAD</i> promoter <sup>6</sup>
P <sub>lacO</sub>	P <sub>LlacO-1</sub> promoter <sup>15</sup>
RBS1	BBa_B0030 (ATTAAAGAGGAGAAA) <sup>21</sup>
RBS2	BBa_B0034 (AAAGAGGAGAAA) <sup>21</sup>
RBS3	BBa_B0029 (TTCACACAGGAAACC) <sup>21</sup>
TermT1	Terminator T1 <sup>15</sup>
TermT0	Terminator T0 <sup>15</sup>
LuxR	LuxR coding sequence (BBa_C0062) <sup>21</sup> , induced by AHL (3OC <sub>6</sub> HSL)
AraC	AraC coding sequence <sup>6</sup>
LacI	LacI coding sequence <sup>15</sup>
GFP	Enhanced Green Fluorescent Protein coding sequence <sup>22</sup>
mCherry	Red Fluorescent Protein coding sequence <sup>22</sup>
ColE1	High-copy number origin of replication <sup>15</sup>
p15A	Medium-copy number origin of replication <sup>15</sup>
pSC101	Low-copy number origin of replication <sup>15</sup>

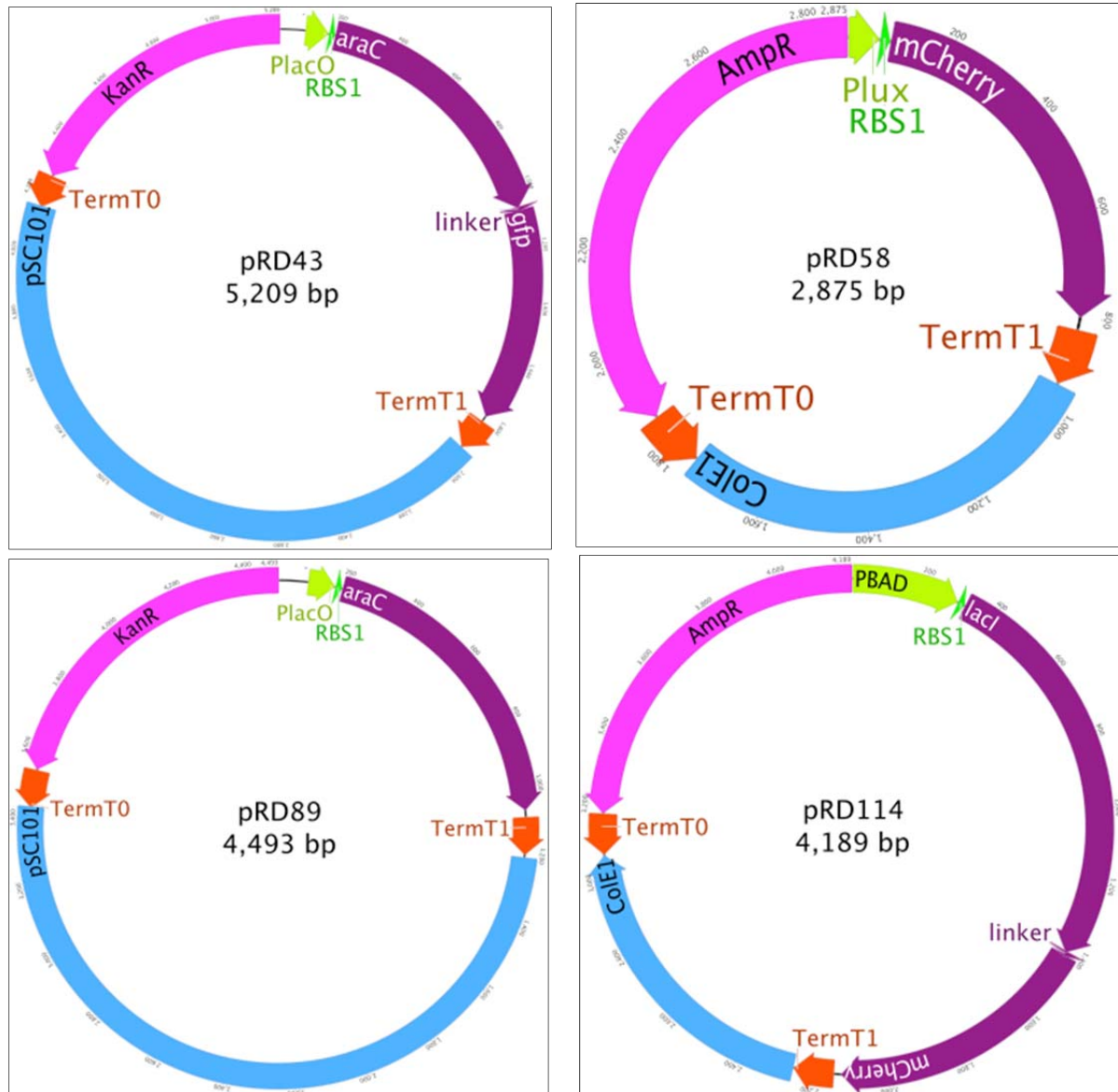
## 14 Plasmid Maps

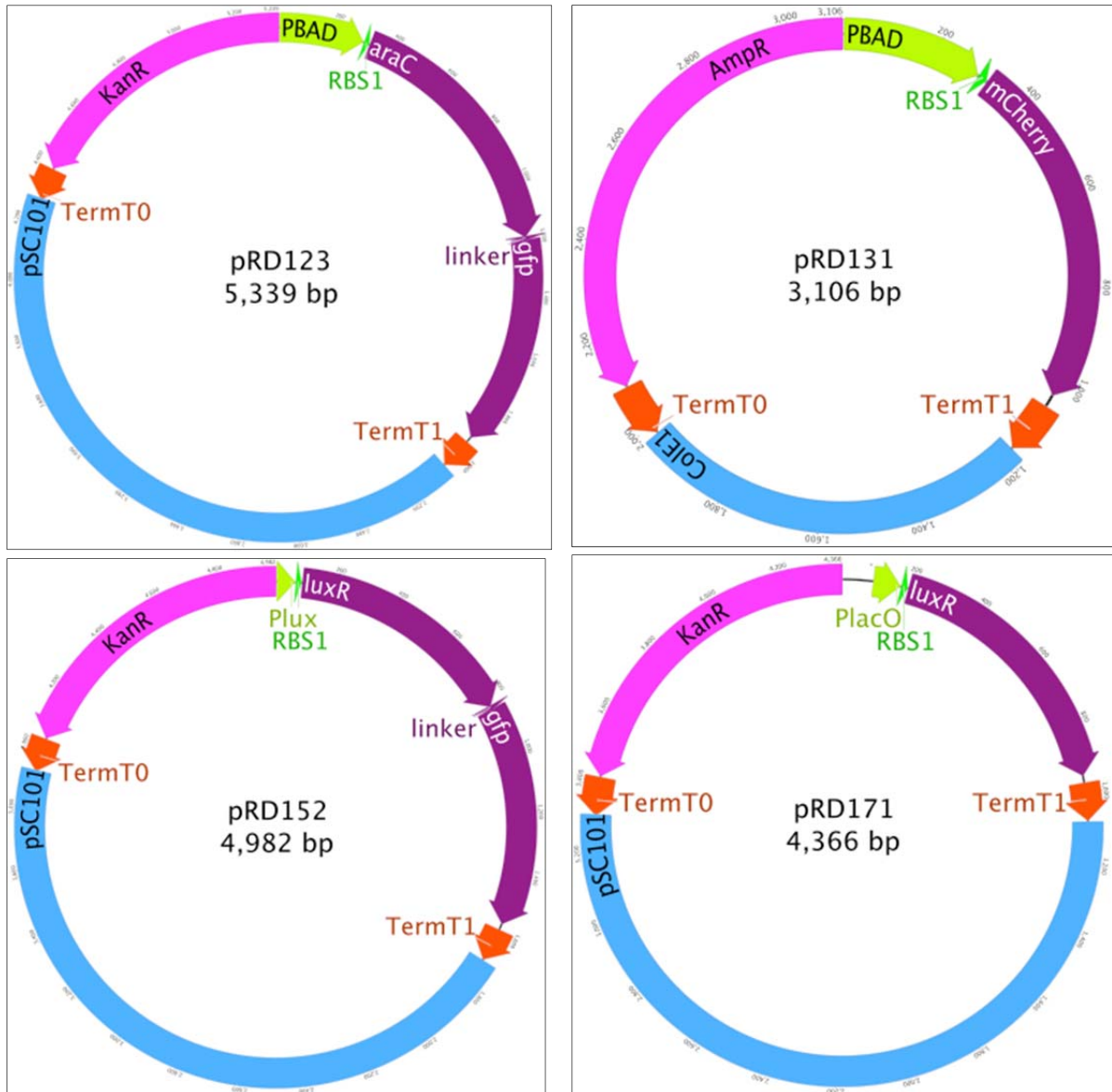
All plasmid sequence files can be found at

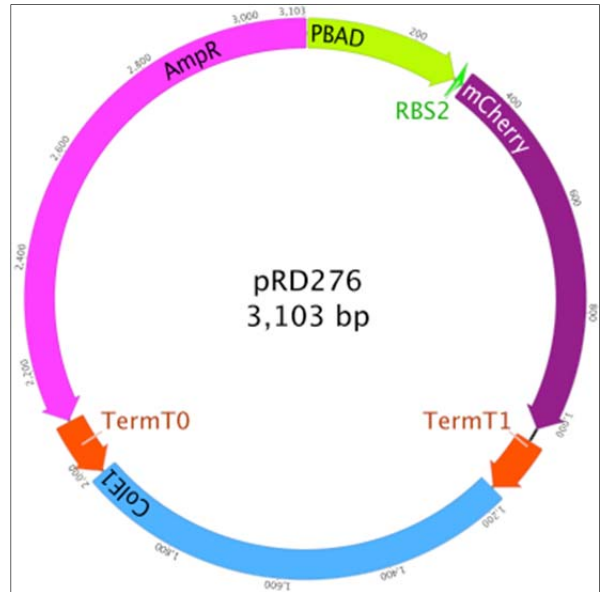
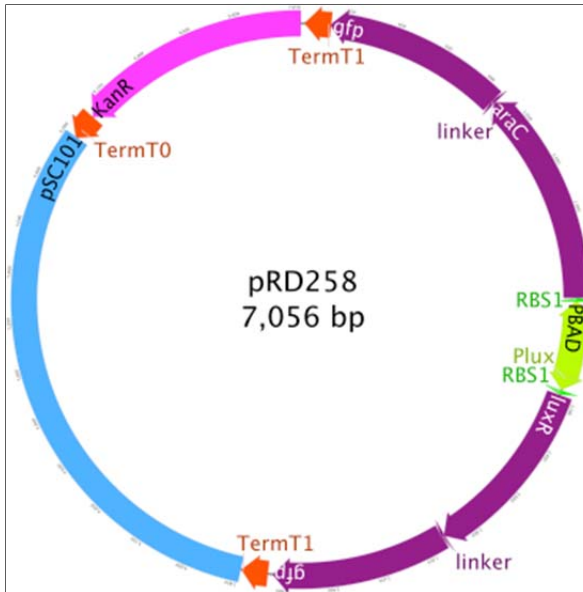
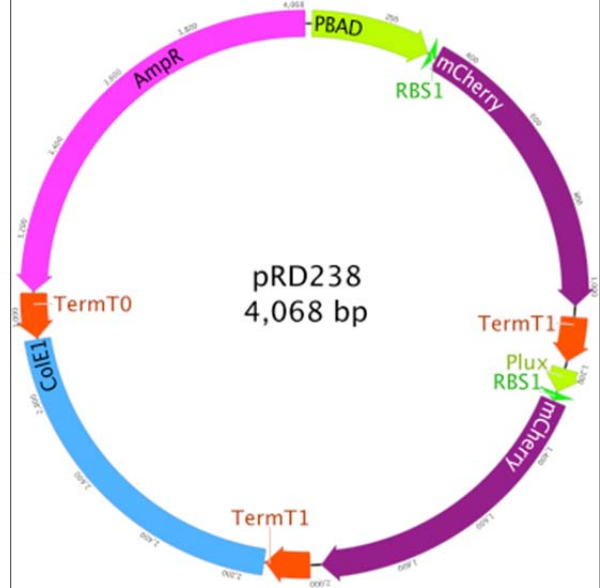
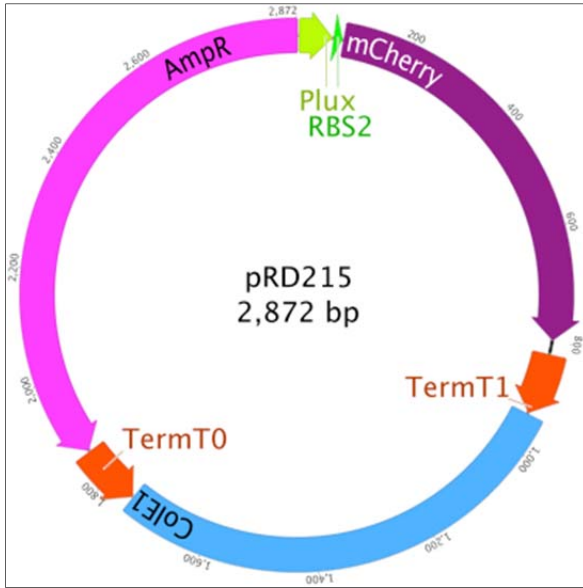
<http://www.rle.mit.edu/acbs/research/supplementary>

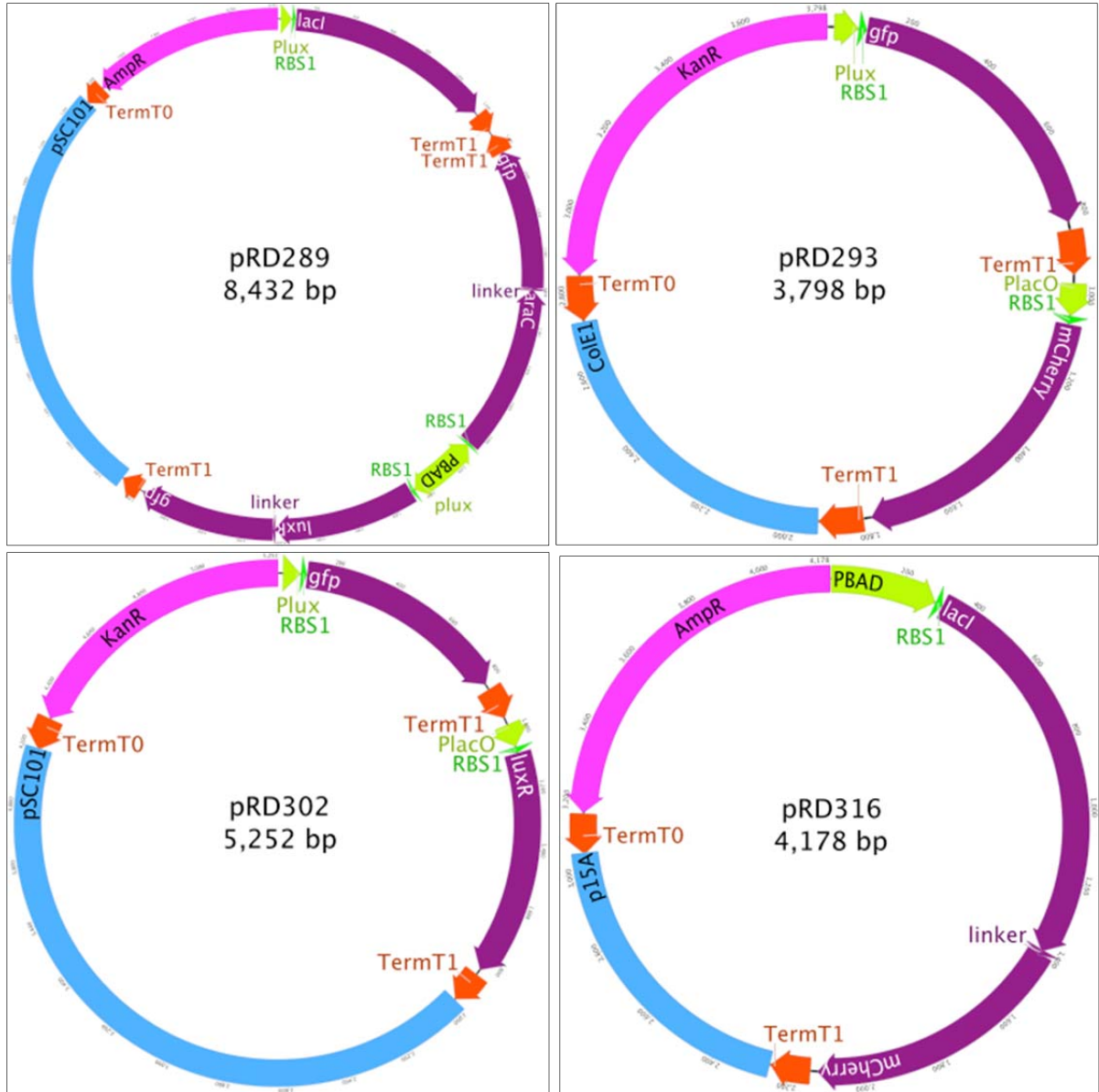
and also at

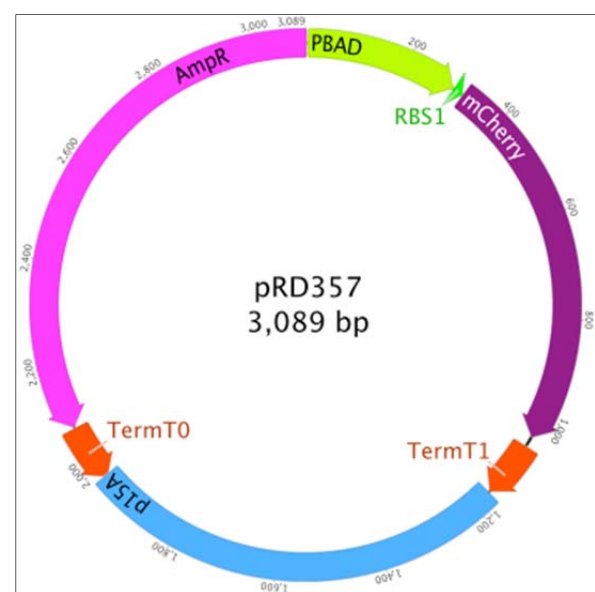
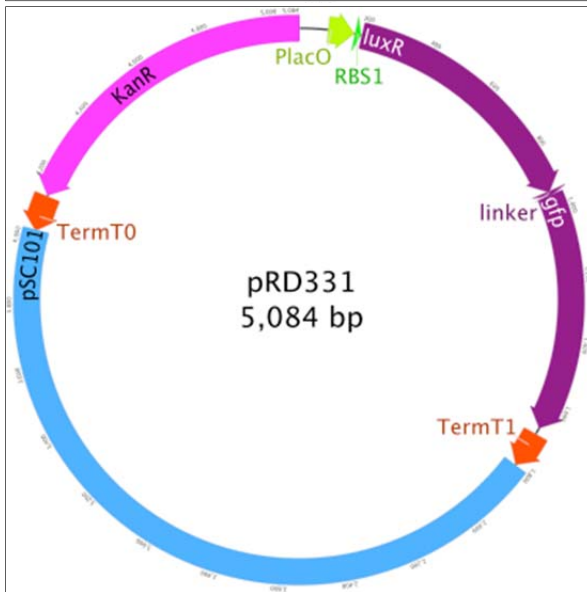
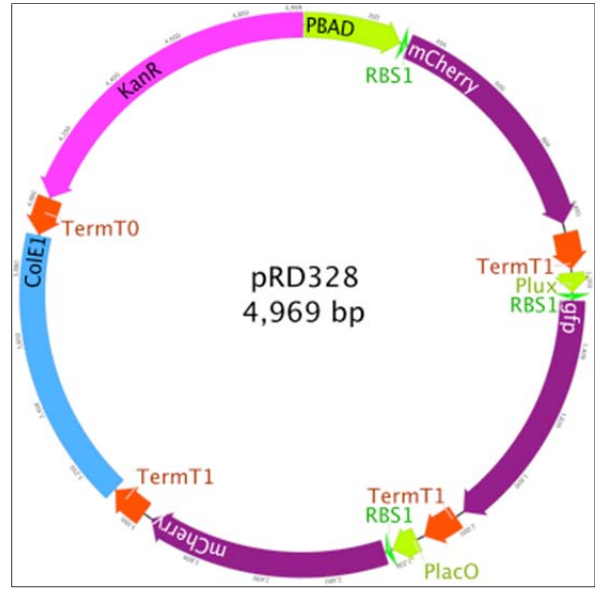
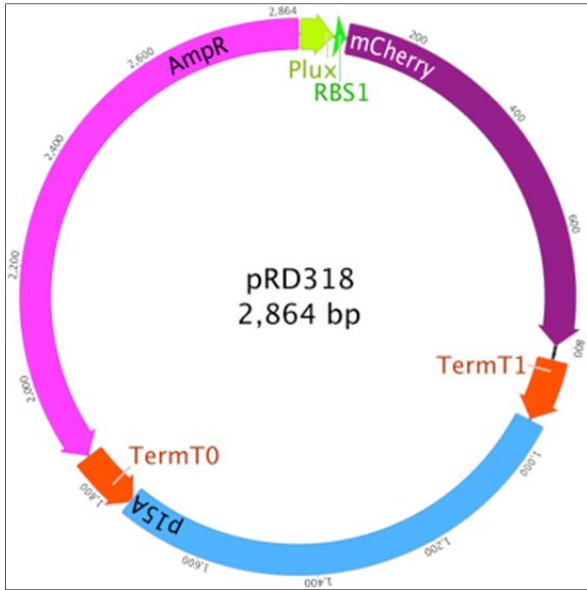
<http://www.rle.mit.edu/sbg/supp.shtml>

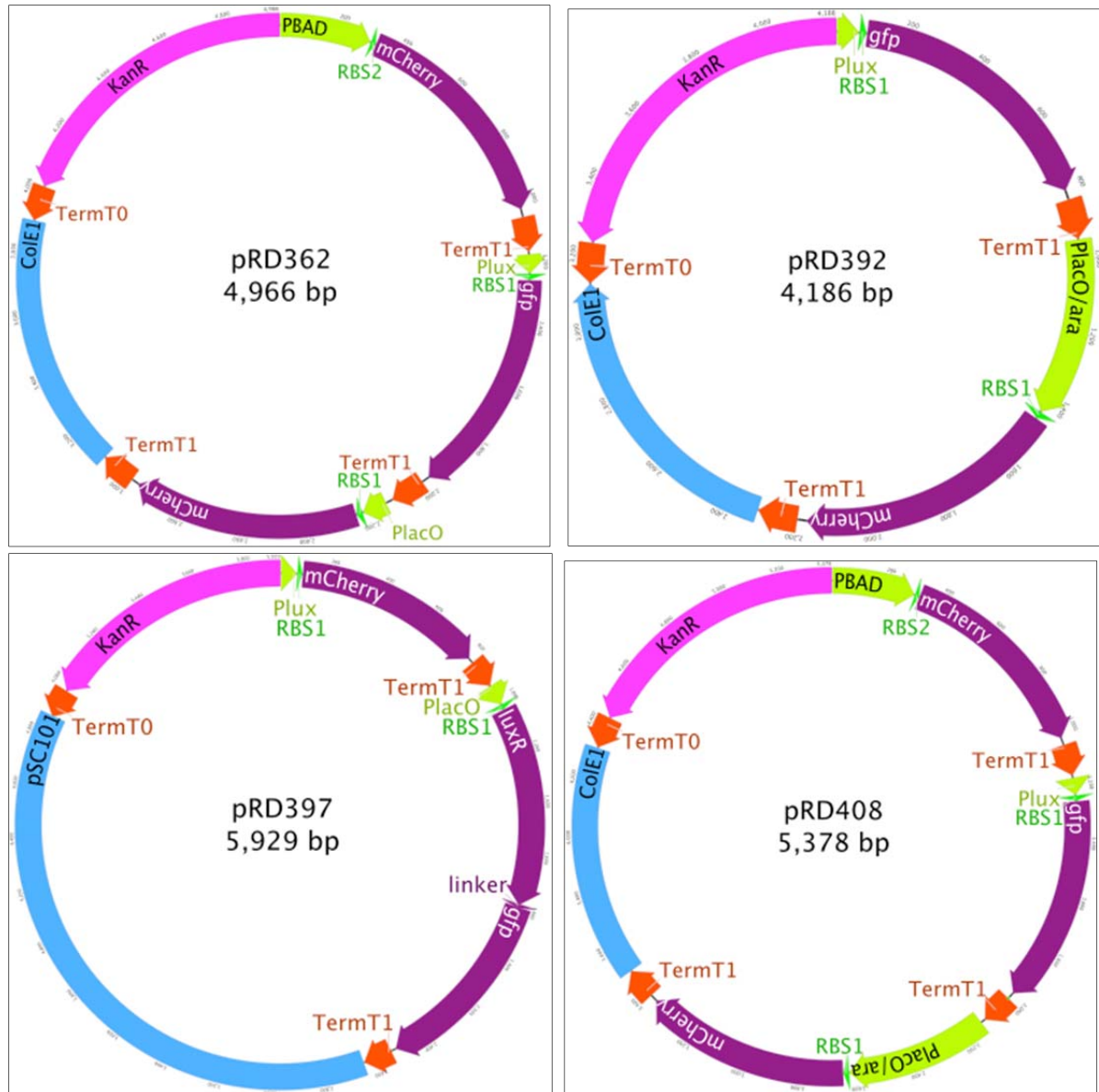


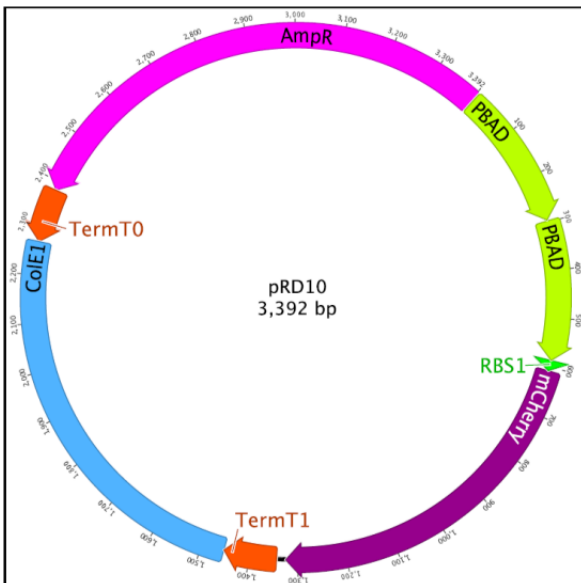
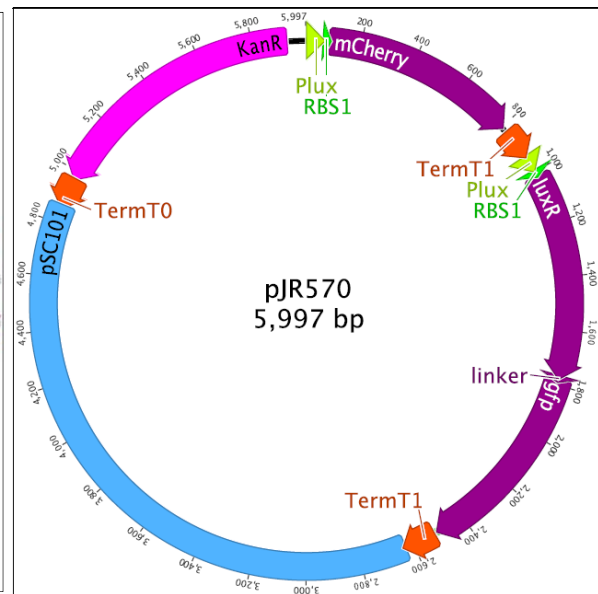
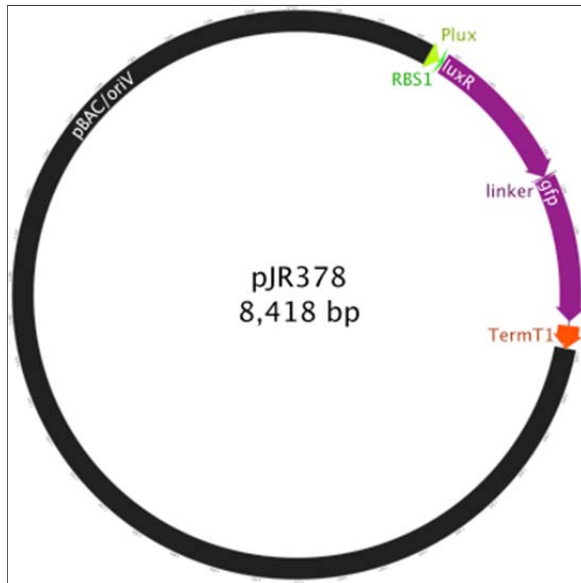












## 15 Supplementary References

1. Sarpeshkar, R. *Ultra Low Power Bioelectronics: Fundamentals, Biomedical Applications, and Bio-Inspired Systems*. Cambridge University Press, Cambridge, 2010. [http://www.rle.mit.edu/acbs/pdfpublications/cyto\\_c24.pdf](http://www.rle.mit.edu/acbs/pdfpublications/cyto_c24.pdf)
2. Hill, T. L. *Cooperativity Theory in Biochemistry* (Springer, New York, 1985).
3. Ackers, G. K. Johnson, A. D. & Shea, M. A. Quantitative model for gene regulation by lambda phage repressor. *Proc Natl Acad Sci* 79, 1129-1133,(1982)
4. Bintu, L. *et al.* Transcriptional regulation by numbers: models. *Curr Opin Genet Dev* 15, 116-124, (2005).
5. Pesci, E. C. Pearson, J. P. Seed, P. C. & Iglewski, B. H. Regulation of las and rhl quorum sensing in *Pseudomonas aeruginosa*. *J Bacteriol* 179, 3127-3132, (1997).
6. Lee, N. L. Gielow, W. O. & Wallace, R. G. Mechanism of araC autoregulation and the domains of two overlapping promoters, Pc and PBAD, in the L-arabinose regulatory region of *Escherichia coli*. *Proc Natl Acad Sci* 78, 752-756, (1981).
7. Tamsir, A. Tabor, J. J. & Voigt, C. A. Robust multicellular computing using genetically encoded NOR gates and chemical 'wires'. *Nature* 469, 212-215, (2010).
8. Burger, A. Walczak, A. M. & Wolynes, P. G. Abduction and asylum in the lives of transcription factors. *Proc Natl Acad Sci* 107, 4016-4021,(2010).
9. Wilkinson, D.J. *Stochastic Modelling for Systems Biology*, (Chapman & Hall/CRC Mathematical & Computational Biology, 2006)
10. Cookson, N. A. *et al.* Queueing up for enzymatic processing: correlated signaling through coupled degradation, *Mol Syst Biol* 7, 561, (2011)
11. Gardner, T. S. Cantor, C. R. & Collins, J. J. Construction of a genetic toggle switch in *Escherichia coli*. *Nature* 403, 339-342, (2000).
12. Ajo-Franklin, C. M. *et al.* Rational design of memory in eukaryotic cells. *Genes Dev.* 21, 2271-2276, (2007)
13. Wunderlich, Z. & Mirny, L. A. Spatial effects on the speed and reliability of protein-DNA search, *Nucleic Acids Res* 36, 3570-3580 (2008)
14. Gardiner, C. *Handbook of stochastic methods: For physics, chemistry and the natural sciences*, (Springer Verlag, Berlin, 1996)
15. Lutz, R. & Bujard, H. Independent and tight regulation of transcriptional units in *Escherichia coli* via the LacR/O, the TetR/O and AraC/I1-I2 regulatory elements. *Nucleic Acids Res* 25, 1203-1210, (1997).

16. Ceroni, F., Furini, S., Giordano, E. and Cavalcanti, S. Rational design of modular circuits for gene transcription: A test of the bottom-up approach. *J. Biol Eng* 4, 14, (2010).
17. Wild, J. Hradecna, Z. & Szybalski, W. Conditionally Amplifiable BACs: Switching From Single-Copy to High-Copy Vectors and Genomic Clones. *Genome Res* 12, 1434, (2002).
18. <http://www.cyflogic.com/>
19. Sambrook, J., Fritsch, E. F., and Maniatis, T. *Molecular Cloning: A Laboratory Manual*, (Cold Spring Harbor Laboratory Press, Plainview, New York, edn. 2, 1989).
20. Daniel, R., Woo, S. S., Turicchia, L., & Sarpeshkar, R. Analog Transistor Models of Bacterial Genetic Circuits, *Proceedings of the IEEE Symposium on Biological Circuits and Systems*, 333-336, (2011).
21. <http://partsregistry.org/>
22. <http://www.microscopyu.com/articles/livecellimaging/fpintro.html>
23. Andersen, J. B, Sternberg C, Poulsen L. K., Bjorn S. P., Givskov M, & Molin S. New unstable variants of green fluorescent protein for studies of transient gene expression in bacteria, *Appl. Environ Microbiol*, 64 (6), 2240-2246 (1998)
24. Shibata, T., and Fujimoto, K. Noisy signal amplification in ultrasensitive signal transduction, *Proc. Natl. Acad. Sci. U.S.A.*, 102, 331-336 (2005).
25. Madar, D., Dekel, E., Bren, A. and Alon, U. Negative auto-regulation increases the input dynamic-range of the arabinose system of Escherichia coli, *BMC Systems Biology*, 5:111 (2011)
26. Isaacs F. J., Dwyer D. J., Ding C, Pervouchine D. D., Cantor C. R., and Collins J. J. Engineered riboregulators enable post-transcriptional control of gene expression. *Nature Biotechnology* 22: 841-847 (2004).
27. Tavakoli, M. & Sarpeshkar, R. A sinh resistor and its application to tanh linearization. *IEEE Journal of Solid-State Circuits*, 40, 536-543, doi:10.1109/jssc.2004.841015 (2005).

28. Gardner, T. S., Cantor, C. R. & Collins, J. J. Construction of a genetic toggle switch in *Escherichia coli*. *Nature* 403, 339-342, doi:10.1038/35002131 (2000).
29. Ajo-Franklin, C. M. et al. Rational design of memory in eukaryotic cells. *Genes Dev* 21, 2271-2276, doi:21/18/2271 [pii] 10.1101/gad.1586107 (2007).
30. Ham, T. S., Lee, S. K., Keasling, J. D. & Arkin, A. P. A tightly regulated inducible expression system utilizing the fim inversion recombination switch. *Biotechnol Bioeng* 94, 1-4, doi:10.1002/bit.20916 (2006).
31. Friedland, A. E. et al. Synthetic gene networks that count. *Science* 324, 1199-1202, doi:324/5931/1199 [pii] 10.1126/science.1172005 (2009).
32. Rinaudo, K. et al. A universal RNAi-based logic evaluator that operates in mammalian cells. *Nat Biotechnol* 25, 795-801, doi:nbt1307 [pii] 10.1038/nbt1307 (2007).
33. Win, M. N. & Smolke, C. D. Higher-order cellular information processing with synthetic RNA devices. *Science* 322, 456-460, doi:322/5900/456 [pii] 10.1126/science.1160311 (2008).
34. Tamsir, A., Tabor, J. J. & Voigt, C. A. Robust multicellular computing using genetically encoded NOR gates and chemical 'wires'. *Nature*, doi:nature09565 [pii] 10.1038/nature09565 (2010).
35. Regot, S. et al. Distributed biological computation with multicellular engineered networks. *Nature* 469, 207-211, doi:10.1038/nature09679 (2011).
36. Anderson, J. C., Voigt, C. A. & Arkin, A. P. Environmental signal integration by a modular AND gate. *Mol Syst Biol* 3, 133, doi:msb4100173 [pii] 10.1038/msb4100173 (2007).
37. Auslander, S., Auslander, D., Muller, M., Wieland, M. & Fussenegger, M. Programmable single-cell mammalian biocomputers. *Nature advance online publication*, *Nature* 487, 123-127, doi: 10.1038/nature11149 (2012).
38. Xie, Z., Wroblewska, L., Prochazka, L., Weiss, R. & Benenson, Y. Multi-input RNAi-based logic circuit for identification of specific cancer cells. *Science* 333, 1307-1311, doi:10.1126/science.1205527 (2011).
39. Nissim, L. & Bar-Ziv, R. H. A tunable dual-promoter integrator for targeting of cancer cells. *Mol Syst Biol* 6, 444, doi:10.1038/msb.2010.99 (2010).
40. Tabor, J. J. et al. A synthetic genetic edge detection program. *Cell* 137, 1272-1281, doi:S0092-8674(09)00509-1 [pii]10.1016/j.cell.2009.04.048 (2009).
41. Prindle, A. et al. A sensing array of radically coupled genetic 'biopixels'. *Nature* 481, 39-44, doi:10.1038/nature10722 (2012).
42. van der Meer, J. R. & Belkin, S. Where microbiology meets microengineering: design and applications of reporter bacteria. *Nat Rev Micro* 8, 511-522 (2010).
43. Burger, A., Walczak, A. M. & Wolynes, P. G. Abduction and asylum in the lives of transcription factors. *Proceedings of the National Academy of Sciences* 107, 4016-4021, doi:10.1073/pnas.0915138107 (2010).

44. Holtz, W. J. & Keasling, J. D. Engineering Static and Dynamic Control of Synthetic Pathways. *Cell* 140, 19-23 (2010).
45. Tolonen, A. C. et al. Proteome-wide systems analysis of a cellulosic biofuel-producing microbe. *Mol Syst Biol* 7, doi:[http://www.nature.com/msb/journal/v7/n1/supinfo/msb2010116\\_S1.html](http://www.nature.com/msb/journal/v7/n1/supinfo/msb2010116_S1.html) (2011).